Alexandre Bittencourt de Sá

OPTICAL AND THERMO-HYDRAULIC CHARACTERIZATION OF LINEAR FRESNEL SOLAR CONCENTRATORS OPERATING WITH DIRECT STEAM GENERATION

Florianópolis
2018

Ficha de identificação da obra elaborada pelo autor,
através do Programa de Geração Automática da Biblioteca Universitária
da UFSC.

Alexandre Bittencourt de Sá

OPTICAL AND THERMO-HYDRAULIC CHARACTERIZATION OF LINEAR FRESNEL SOLAR CONCENTRATORS OPERATING WITH DIRECT STEAM GENERATION

Esta Tese foi julgada adequada para obtenção do Título de "Doutor em Engenharia Mecânica", e aprovada em sua forma final pelo Programa de Pós-Graduação em Engenharia Mecânica.

Florianópolis, 06 de Novembro de 2018.

_____
Prof. Jonny Carlos da Silva, PhD
Coordenador do Curso
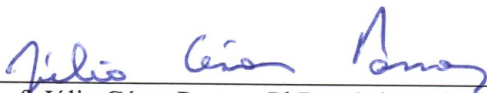
_____
Prof. Júlio César Passos, PhD – Orientador
Universidade Federal de Santa Catarina
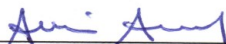
_____
Prof. Lounès Tadrist, PhD – Coorientador
Aix-Marseille Université

Banca Examinadora:

Prof. Júlio César Passos, PhD – Orientador
Universidade Federal de Santa Catarina

Amir Antonio Martins Oliveira Jr., Ph.D
Universidade Federal de Santa Catarina

José Roberto Simões Moreira, PhD - Relator
Escola Politécnica da Universidade de São Paulo

Rafaela Frota Reinaldo, Dra
Centro de Pesquisas Leopoldo Américo Miguez de Mello
PETROBRAS

Samuel Luna de Abreu, Dr
Instituto Federal de Santa Catarina

Vicente de Paulo Nicolau, Dr
Universidade Federal de Santa Catarina

To my parents Jussara and Alamiro.

AGRADECIMENTOS

Gostaria de agradecer também às pessoas importantes de minha vida particular: a minha família por sua compreensão e apoio incondicional de minha decisão de aprimorar minha formação acadêmica, em especial a minha mãe Jussara, cujos passos segui ao decidir ingressar no doutorado e a meu pai Alamiro, que foi minha inspiração para me tornar engenheiro; a minha irmã Naiana e minhas queridas sobrinhas Isabela e Marina; ao meu velho amigo e companheiro Odin; a minha amiga Manuela com quem compartilhei minha estadia na França; a Greice por ter ajudado na revisão de um importante artigo, parte desta tese; ao Marcos pela companhia detestável durante 2411km ao redor da Islândia; aos meus colegas de engenharia Murilo e Silva, pelos bons p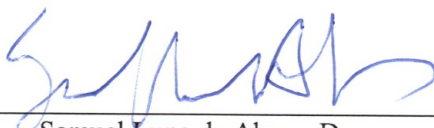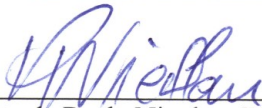apos e investimentos em Silva-Coins, aos amigos com quem joguei RPGs e jogos de tabuleiro para descontrair nos momentos de dificuldade; aos amigos que me acompanhavam aos bares para bater bons papos; a turma de São Martinho, aquele lugar mágico; aos meus amigos da Amurel; e aos meus bons amigos, o astrofísico e modelo Daniel e meus companheiros de boemia Dedo e Jonas.

Preço desculpa aos amigos que esqueci de citar aqui, saibam que estão em meu coração, mas o doutorado e a idade cobraram um preço alto da minha memória!

Agradeço também a todos que tirarem um tempo para ler o meu trabalho.

ACKOWLEDGEMENTS

"The Road goes ever on and on
Down from the door where it began.
Now far ahead the Road has gone,
And I must follow, if I can."
(Baggins, Bilbo)

RESUMO

Existem diferentes formas de aproveitar a energia solar; uma delas é usando a tecnologia de energia solar concentrada (CSP do inglês Concentrating Solar Power). Sistemas CSP utilizam espelhos ou lentes para concentrar a radiação solar, aumentando seu desempenho. Atualmente, a maior parte da tecnologia CSP consiste em coletores cilindro-parabólicos operando com óleo térmico; no entanto, uma estratégia operacional relativamente nova chamada geração direta de vapor (DSG do inglês Direct Steam Generation) tem sido cada vez mais estudada e usada. Neste caso o fluido de transferência de calor nos campos solares é a água. O vapor é então produzido diretamente dentro do concentrador solar. Essa estratégia operacional é promissora e competitiva para as usinas térmicas e uso industral, principalmente devido ao potencial de melhoria de desempenho e redução de custos. Além disso, a tecnologia de concentradores Fresnel lineares também tem um grande potencial para redução de custos e é recomendada para operação em DSG. Este trabalho estudou duas bancadas experimentais de LFC, uma desenvolvida pelo laboratório LEPTEN, da Universidade Federal de Santa Catarina, e a outra é um protótipo da empresa SunCNIM. O objetivo deste trabalho é apresentar uma análise paramétrica e térmica destes concentradores, com base em resultados experimentais. Este estudo apresenta uma metodologia de como avaliar novos concentradores Fresnel lineares e dá indicação da instrumentação necessária. Os objetivos específicos são obter a: caracterização geométrica; caracterização óptica usando dados experimentais; avaliação de perda de calor usando dados experimentais; modelo termo-hidráulico bifásico; comparação entre os resultados do modelo com experimento e análise dos resultados. Foi observado que a utilização de concentradores Fresnel lineares operando em DSG é um processo viável, embora algumas complexidades sejam adicionadas devido ao fluxo bifásico. O dimensionamento do tubo absorvedor é de extrema importância para atingir padrões de escoamento desejáveis e para obter uma queda de pressão aceitável no concentrador. O modelo de padrões de escoamento adotado fornece uma estimativa do que está acontecendo dentro do tubo. No geral, o concentrador Fresnel linear do LEPTEN apresentou um bom desempenho em operação e resultados satisfatórios para um sistema de pequena escala, no entanto, um novo design do receptor é necessário.

Palavras-chave: Energia renovável; energia solar; concentrador Fresnel linear; análise paramétrica; análise termo-hidráulica bifásica.

RESUMO EXPANDIDO

Introdução

Atualmente, nossa sociedade enfrenta um enorme desafio relacionado à demanda de energia. Não só as matrizes energéticas devem ser diversificadas, como se espera que os modos de produção de energia tenham cada vez menos impacto sobre o meio ambiente. A maior parte da energia gerada é proveniente de fontes insustentáveis e está geralmente associada a emissões de gases que contribuem para o efeito estufa. Esses fatos reforçam a ideia da necessidade de se migrar cada vez mais para fontes renováveis e, entre elas, a energia solar aparece como uma opção promissora. Existem diversas maneiras de tomar proveito da radiação solar, e uma delas é através da utilização da tecnologia de energia solar concentrada (CSP do inglês Concentrating Solar Power). Os sistemas CSP utilizam espelhos ou lentes para concentrar a radiação solar em uma área menor, onde um receptor está posicionado, a fim de obter maiores fluxos de calor. Isso possibilita obter maiores temperaturas e aumentar a eficiência térmica e termodinâmica de um sistema quando comparado com coletores de placa plana. O CSP é considerado uma tecnologia viável para suprir uma parte considerável da demanda futura de energia, no que diz respeito a energias renováveis (MÜLLER-STEINHAGEN; TRIEB; TRIEB, 2004).

A maior parte das tecnologias CSP utilizadas mundialmente baseia-se no conceito de concentrador parabólico (PTC do inglês Parabolic Trough Concentrators), operando com óleo térmico como fluido de transferência de calor (HTF do inglês Heat Transfer Fluid) (ELSAFI, 2015). Nestes sistemas, o circuito de óleo térmico troca calor com água e vapor dentro de um ciclo Rankine. No entanto, uma estratégia operacional relativamente nova tem sido cada vez mais estudada e utilizada, onde o HTF operando nos campos solares é a água. Nesse caso, o vapor é produzido diretamente nos concentradores solares, eliminando a necessidade dos trocadores de calor mencionados anteriormente, tornando o sistema mais simples. Essa estratégia operacional é chamada de geração direta de vapor (DSG do inglês Direct Steam Generation).

O processo DSG promete ser competitivo para as usinas de óleo térmico, especialmente devido ao potencial de melhoria de desempenho e redução de custos. Neste contexto, foi realizado o projeto heliotérmica CNPq (Proc. 406357 / 2013-7), pelo laboratório LEPTEN, da Universidade Federal de Santa Catarina. Este projeto tem como objetivo a concepção e construção de um LFC, para operar na DSG, utilizando materiais locais de baixo custo, e estudar sua viabilidade e desempenho. O protótipo LFC

do LEPTEN é estudado neste trabalho. Além disso, parte do presente trabalho de doutorado foi realizado no exterior, no laboratório IUSTI "Institut Université des Systèmes Thermiques Industriels" (IUSTI, UMR 7343), da Universidade de Aix-Marselha e do CNRS (Centro Nacional de Pesquisa Científica), em Marselha no sul da França, sob a supervisão do professor Lounès Tadrist. Isso visou trocar conhecimentos sobre a tecnologia LFC e fortalecer os laços de pesquisa entre o LEPTEN e o IUSTI, e também contou com a parceria entre o laboratório IUSTI e a empresa SunCNIM, que possui um protótipo do tipo concentrador LFC operacional, de tamanho industrial e em operação a vários anos.

Objetivos
Este trabalho apresenta uma análise paramétrica e térmica, baseada nos resultados experimentais dos dois protótipos LFC mencionados. O estudo apresenta uma metodologia de como avaliar um concentrador LFC e dá uma indicação da instrumentação necessária para faze-lo. Os objetivos específicos para os protótipos LFC são: Caracterização geométrica; Caracterização óptica usando dados experimentais; Avaliação de perda de calor usando dados experimentais; Modelo termo-hidráulico para o HTF; Balanço de energia usando perdas de calor experimentais; Modelo de queda de pressão monofásica; Modelo de queda de pressão bifásica; Validação de modelo usando dados da literatura; Comparação entre os resultados do modelo com os experimentais e Verificar a viabilidade do modo DSG para os protótipos estudados.

Metodologia
O desenvolvimento do trabalho é dividido em duas partes. A primeira é a caracterização dos principais parâmetros dos protótipos LFC. Os parâmetros estudados são as curvas de modificadores de ângulo de incidência, a eficiência óptica de pico e as curvas de perda de calor. Alguns modelos complementares tiveram que ser desenvolvidos para caracterizar totalmente o protótipo do LEPTEN, e são o resultado de aspectos específicos do projeto e construção desta bancada de estudos.
A segunda parte do desenvolvimento do trabalho é uma análise termo-hidráulica. Para isso, desenvolveu-se um modelo termo-hidraulico para estudar tanto a parte monofásica quanto bifásica do escoamendo no interior dos tubos absorvedores. Este modelo inclui um balanço térmico usando as curvas de perda de calor experimentais. A queda de pressão foi modelada para fluxos monofásicos e bifásicos. A equação de Fanning foi utilizada para queda de pressão monofásica, com os fatores de atrito Bla-

sius e Colebrook-White. Este último foi desenvolvido para tubulações industriais, levando em consideração a rugosidade da superfície. A queda de pressão em duas fases utilizou diferentes modelos: Homogêneo; Lockhart e Martinelli; Friedel; Müller-Steinhagen e Heck; e uma correlação baseada nos padrões de escoamento. A correlação baseada em padrões de escoamento é um modelo fenomenológico proposto por Quibén e Thome (MORENO QUIBÉN; THOME, 2007b, 2007a). Essa correlação utilizou o mapa de fluxo diabático desenvolvido por Wojtan, Ursenbacher e Thome (WOJTAN; URSENBACHER; THOME, 2005a, 2005b).

Ambos os protótipos foram avaliados dentro deste modelo, que foi ajustado de acordo com cada LFC. A parte LEPTEN também incluiu a distribuição de radiação concentrada não uniforme entre os seis tubos absorvedores, que apresentou uma boa concordância com a distribuição experimental da temperatura ao longo dos tubos.

Resultados e Discussão

O modelo termo-hidráulico foi verificado com dados experimentais encontrados na literatura da instalação DISS (Direct Solar Steam), da plataforma solar de Almeria. Observou-se que o modelo fenomenológico não respondeu particularmente bem aos casos de baixa pressão, subestimando a queda de pressão. Os modelos que apresentaram o melhor ajuste para todos os dados experimentais foram os de Friedel e Muller-Steinhagen e Heck. Para pressões mais altas, o modelo fenomenológico também apresentou resultados confiáveis. Este modelo também indica o padrão de escoamento no tubo absorvedor. A distribuição de padrão de escoamento ao longo do tubo foi comparada com um trabalho numérico (MOYA; VALENZUELA; ZARZA, 2011), que simulou o escoamento bifásico em RELAP. Ambos os modelos apresentaram resultados semelhantes.

Um dos protótipos do LFC analisados neste trabalho foi a bancada de trabalho SunCNIM. Para este caso, a curva de perda de calor foi dada pela própria empresa, e as curvas de modificador de ângulo de incidência utilizadas foram obtidas por meio do software SolTrace. A avaliação paramétrica serviu apenas para obter a eficiência óptica de pico. Na análise termo-hidráulica os parâmetros do LFC foram variados para avaliar sua influência no padrão de escoamento. Verificou-se que a geometria do tubo desempenha um papel importante no padrão de fluxo. Uma redução de 20 % no diâmetro interno mostrou fluxo anular de quase 60 % do tubo em casos de 3 MPa e quase metade do tubo em casos de 5 MPa. Os benefícios térmicos da redução do diâmetro vêm associados a um aumento médio na queda de pressão de cerca de 3,5 % no nível de pressão mais baixo, que pode ser considerado tolerável.

O outro LFC estudado é o do LEPTEN, instalado em Florianópolis na Universidade Federal de Santa Catarina, na região no sul do Brasil. Ele é um protótipo LFC de pequena escala, capaz de fornecer vapor para a indústria, porém a temperaturas mais baixas como as da SunCNIM. Para este caso, a caracterização dos parâmetros foi utilizada para obter a eficiência óptica de pico e a curva experimental de perdas de calor. As curvas de modificador de ângulo de incidência foram obtidas inicialmente usando o software SolTrace, entretanto, a curva longitudinal mostrou discrepâncias com dados experimentais. Para isso, outros experimentos foram realizados com a intenção de ajustar tais curvas calculadas com dados experimentais. Os procedimentos para caracterização de parâmetros mostraram um desempenho satisfatório na identificação desses principais parâmetros de um LFC.

Um detalhe específico do LFC do LEPTEN é que seu absorvedor é móvel, possibilitando reduzir as perdas de final de linha. As perdas de final de linha médias, considerando o movimento devido ao sul para os períodos em que o deslocamento máximo não pode compensar totalmente o ângulo de incidência, são de 4 %. Para um absorvedor fixo, esse valor atinge 35 %. A análise mostrou que o absorvedor móvel apresenta grande vantagem para protótipos de pequena escala, e que não é viável para linhas longas de LFC. Quanto à análise termo-hidráulica, foram utilizados dois conjuntos de testes experimentais. Primeiro, houve os experimentos monofásicos, que foram usados para validar o modelo de escoamento monofásico, e estudar o comportamento da bancada de trabalho em condições mais controladas do que as encontradas nos testes bifásicos. Verificou-se que a rugosidade do tubo tem um impacto na queda de pressão. Os resultados da correlação de Colebrook apresentaram uma diferença de medidas em torno de -0,5 %; enquanto que para a correlação de Blasius, os valores medidos de queda de pressão foram cerca de 50 % maiores que os encontrados. O modelo de radiação concentrada não uniforme também apresentou melhor ajuste com dados experimentais, representando melhor o desenvolvimento do perfil de temperatura ao longo do tubo. Encontraram-se grandes erros nas quedas de pressão para escoamentos bifásicos. Existem alguns aspectos que podem justificar esses erros, como erros na medição da vazão volumétrica, vazamentos nas conexões, tubos não preenchidos completamente com líquido e acúmulo de vapor nas mangueiras flexíveis. Os erros de alguns testes atingiram um valor de cerca de 80 %.

Considerações Finais
O modo de operação de geração direta de vapor aparenta ter um futuro promissor. Existem diversos estudos sendo feitos na área, de caráter tanto

teórico quanto experimental. Quanto as bancadas experimentais estudadas neste trabalho, verificou-se que é viável a operação em DSG utilizando concentradores solares do tipo Fresnel linear. O protótipo da SunC-NIM já está em operação há vários anos, e apresentou um bom desempenho óptico. O protótipo do LEPTEN apresentou um bom desempenho, em especial o sistema de absorvedor móvel, que impactou bastante na performance geral do concentrador. Entretanto foi observado que este desempenho é dependente da pequena escala do LFC estudado. O modelo desenvolvido foi utilizado para simular uma condição de filas mais longas de LFC, utilizando módulos do protótipo LEPTEN. Para tais condições, verificou-se que a configuração multitubo com o diâmetro original resultavam numa perda de carga muito grande, e modificações deveriam ser feitas. Em ambos os casos foi visto que é possível fazer uma análise dos parâmetros de projeto das plantas LFC, de forma a melhorar o caráter termo-hidraulico das mesmas, seja referente a queda de pressão ou aos padrões de escoamento encontrados. Tais modificações estão previstas para o protótipo do LEPTEN, entre outras que incluem a substituição e adição de mais sensores de pressão e temperatura, a substituição da bomba hidráulica, uma melhor fixação dos tubos flexíveis e avaliação de possíveis vazamentos.

Palavras-chave: Energia renovável; energia solar; concentrador Fresnel linear; análise paramétrica; análise termo-hidráulica bifásica.

ABSTRACT

There are different ways to harness the solar energy; one of them is by using the Concentrating Solar Power (CSP) technology. The CSP system makes use of mirrors or lens in order to concentrate the solar radiation, increasing its performance. Nowadays most of the CSP technology consists on parabolic trough collector operating with thermal oil; however, a relatively new operational strategy called direct steam generation (DSG) has been increasingly studied and used, where the heat transfer fluid in the solar fields is water. Steam is then produced directly inside the solar concentrator. This operational strategy is, and it promises to be competitive to the thermal oil plants, especially due to the potential of performance improvement and cost reductions. In addition, the linear Fresnel concentrator technology (LFC) have also a great potential for cost reduction, and it is recommended for operating in DSG. This work studied two experimental LFC benches, one developed by the LEPTEN laboratory, from the Federal University of Santa Catarina, and the other is a prototype from the company SunCNIM. The objective of this work is to present a parametrical and thermal analysis of these concentrators, based on the experimental results. This study presents a methodology for how to evaluate new LFCs and gives indication of the instrumentation needed. The specific objectives are to obtain: geometric characterization; optical characterization using experimental data; heat loss evaluation using experimental data; thermo-hydraulic two-phase model for the heat transfer fluid; comparison between model results with experiment and analysis of the results. It was seen that by the DSG using linear Fresnel concentrators is a viable process, although some complexities are added due to the two-phase flow. The dimensioning of the absorber tube is of utter importance achieving desirable flow patterns, and for the pressure drop of the LFC. The two-phase flow model gives an insight of what is happening inside the tube. Overall the LEPTEN linear Fresnel concentrator presented a good performance in operation, and satisfactory results for a small-scale concentrator, however, a re-design of the receiver is needed if it is to be used in larger scale.

keywords: Renewable energy; solar energy; linear Fresnel concentrator; parametrical analysis; Thermo-hydraulic two-phase analysis.

LIST OF FIGURES

LIST OF TABLES

LIST OF ABBREVIATIONS AND ACRONYMS

CNRS	Centre National de La Recherche Scientifique
CSP	Concentrating Solar Power
DISS	Direct Solar Steam
DNI	Direct Normal Irradiance
DSG	Direct Steam Generation
EES	Engineering Equation Solver
HTF	Heat Transfer Fluid
IAM	Incidence Angle Modifier
IUSTI	Institut Universitaire des Systèmes Thermiques Industriels
LEPTEN	Laboratórios de Engenharia de Processos de Conversão e Tecnologia de Energia
LFC	Linear Fresnel Collector
MCRT	Monte Carlo Ray Tracing
PSA	Plataforma Solar de Almería
PTC	Parabolic Trough Collector
QDT	Quasi-Dynamic Test Method
RMSE	Root Mean Square Errors
SPA	Solar Position Algorithm
UFSC	Universidade Federal de Santa Catarina

LIST OF SYMBOLS

Latin alphabet:	Unit	
A	[m^2]	Area
a	[W/m.K^2]	Curve parameter
b	[W/m.K]	Curve parameter
C	[-]	Chisholm parameter
$\bar{c}_p$	[J/kg.K]	Mean specific heat at constant pressure
D	[m]	Diameter
DNI	[W/m^2]	Direct normal irradiation
f	[-]	Friction factor
Fr	[-]	Froude number
G	[kg/s.m^2]	Mass velocity
G_d	[W/m^2]	Diffuse radiation
g	[m/s^2]	Gravitational acceleration
h_r	[m]	Height from the aperture plane to the receiver
IAM	[-]	Incidence angle modifier
L	[m]	Length
$\dot{m}$	[kg/s]	Mass flow
p	[Pa]	Pressure
$\dot{Q}$	[W]	Heat flux
q''_{crit}	[W/m^2]	Critical wall heat flux
Re	[-]	Reynolds
r_0	[m]	Offset pivot distance
T	[ºC]	Temperature
u	[m/s]	Velocity
We	[-]	Weber number
X	[-]	Lockhart- Martinelli parameter
x	[-]	Steam quality
x_n	[m]	Variation in the x axis due to the offset
x_0	[m]	Position on the horizontal plane of the turning axis of the mirror line
y_n	[m]	Variation in the y axis due to the offset
z	[m]	Length

Greek alphabet:

α	[-]	Void fraction
α_s	[º]	Solar altitude angle
γ	[º]	Azimuth
Δh_{evap}	[kJ/kg]	Evaporation enthalpy of water
Δ_z	[m]	Infinitesimal element of length
ε	[mm]	Surface roughness
η_{endL}	[-]	End losses
$\eta_{0º}$	[-]	Zero optical efficiency
θ	[º]	Angular relation
θ_n	[º]	Inclination of the mirror plane
θ_Z	[º]	Zenith angle
μ	[N.s/m²]	Dynamic viscosity
ρ	[kg/m³]	Density
σ	[N/m]	Surface tension
ϕ^2	[-]	Two phase friction multipliers

Subscripts

$1ph$	Single-phase
$2ph$	Two-phase
A	Annular flow
abs	Absorbed
amb	Ambient
col	Collector
$dryout$	Dryout flow
eq	Equivalent
H	Homogeneous
HL	Heat loss
I	Intermittent flow
i	Incidence / inlet / inner
IA	Intermittent to annular flows
L	Longitudinal / liquid
LO	Liquid only
m	Mirrors / mean
$mist$	Mist flow
o	Outlet
$pipe$	Absorber pipe
S	Section
s	Solar
Sat	Saturated

Slug	Slug flow
stat / S	Stratified flow
SW	Stratified wavy flow
T	Transversal
V	Vapor
VO	Vapor only
wavy	Wavy flow

SUMMARY

1 INTRODUCTION

1.1 Context

Nowadays our society faces a challenge regarding energy production. Not only energy matrixes must be diversified, as the ways of production must have less and less impact on the environment. Most of the energy generated comes from unsustainable sources, and it is usually associated with greenhouse gas emissions. These facts strengthen the idea of increasingly migrating to renewable sources, and among them, the solar energy appears as a promising option.

There are many ways of harnessing the solar radiation, and one of them is by use of the concentrating solar power (CSP) technology. The CSP systems make use of mirrors or lens in order to concentrate the solar radiation on a smaller area, where a receiver is located, in order to obtain higher temperatures and/or heat fluxes and reduce the prices of conversion in electricity, for example, and increasing the thermal and thermodynamics efficiency when compared with flat plate collectors.

The CSP is said to be a viable technology to supply a considerable part of the future energy demand, regarding renewable energy (MÜLLER-STEINHAGEN; TRIEB; TRIEB, 2004). The International Energy Agency has developed roadmaps for the CSP technology, on which the goal set on 2010 was for CSP to supply 11% of the total global electric energy demand by 2050. Another roadmap later developed, in 2014, has maintained this goal, which indicates a positive trend for CSP (PHILIBERT C, 2014). On this same roadmap, it is set that the CSP alongside photovoltaic will be able to provide 27% of the global electricity demand in 2050. In addition, suggestions are made in order to slow global warming.

Although this roadmap focuses on electrical generation, the CSP can also be used to provide heat for industrial processes. At the present time, most of the concentrating solar power (CSP) technologies used worldwide are based on the parabolic trough collector (PTC) concept, operating with thermal oil as heat transfer fluid (HTF) (ELSAFI, 2015). On those systems, the thermal oil circuit is connected to a Rankine cycle by thermal heat exchangers, where steam is produced.

However, a relatively new operational strategy has been increasingly studied and used, where the HTF operating on the solar fields is water. In that case, steam is directly produced on the solar concentrators, eliminating the need of the heat exchangers mentioned before, making the

power plant simpler. This operational strategy is called direct steam generation (DSG).

Although thermal oil plants present more controllability when compared to DSG, regarding the HTF properties on the outlet of the solar field, the latter technology presents some advantages. The oil degradation temperature limits the maximum operational temperature for thermal oil plants. For DSG, the operational temperature can reach higher values, hence increasing the overall efficiency (BIENCINTO; GONZÁLEZ; VALENZUELA, 2016). The environmental impact for DSG is also smaller, since leakage of oil presents a higher hazard. The DSG process is becoming the main research subject for PTC, and the research in this subject is growing for linear Fresnel collectors (LFC) (ROJAS; DE ANDRÉS; GONZÁLEZ, 2008).

DSG process promises to be competitive to the thermal oil plants, especially due to the potential of performance improvement and cost reductions. However, research must be performed on this subject.

The present doctorate work is part of the heliothermic project, CNPq (Proc. 406357/2013-7), conducted by the Heliotérmica research group of the LEPTEN laboratory, from the Federal University of Santa Catarina. This project has as objective the conception and construction of an LFC, to operate at DSG, using local low-cost materials, and study the feasibility and performance of this prototype.

In addition, part of this doctorate study was performed abroad, at the IUSTI "Institut Universitaire des Systèmes Thermiques Industriels" (IUSTI, UMR 7343) laboratory, from the University of Aix-Marseille and CNRS (Centre National de la Recherche Scientifique), in Marseille, France, under the supervision of professor Lounès Tadrist. This aimed to exchange knowledge on the LFC technology, and to strengthen the research ties between LEPTEN and IUSTI. The work in Marseille counted with the partnership between the IUSTI laboratory and the company SunCNIM, which had an operational LFC concentrator prototype. Since part of the doctorate work was performed over this prototype from SunCNIM, and the initial models and results were developed and acquired for it. These analyses are also presented on this thesis.

The main focus however, is the prototype build by the Heliotérmica group. The stages of conception and design of the LEPTEN LFC are only briefly presented here. More information about these stages can be seen in Appendix A. There, a small description of the works performed by the group Heliotérmica can be seen, alongside with their reference.

1.2   Objectives

This work presents a parametrical and thermal analysis of this concentrator, based on the experimental results. This study presents a methodology for how to evaluate a new LFC and gives indication of the instrumentation needed. The specific objectives for the LFC prototypes are:

- Geometric characterization;
- Optical characterization using experimental data;
- Heat loss evaluation using experimental data;
- Thermo-hydraulic model for the HTF;
    - Energy balance using experimental heat losses;
    - Single-phase pressure drop model;
    - Two-phase pressure drop model;
- Model validation using data from literature;
- Comparison between model results with experimental ones;
- Verify the feasibility of DSG for the prototypes.

1.3   Structure of the thesis

This work is divided in seven chapters. The first chapter is the introduction, where a brief context of the global scenery and of the technology aspects of this study is presented, as are the objectives of this work.

Chapter 2 presents a literature review about solar generation, CSP technologies, DSG and an overview of the main works performed on the literature on these subjects. A more complete review can be seen on (DE SÁ et al., 2018).

Chapter 3 describes the experimental benches studied in this work, which are the LFC prototypes from SunCNIM and LEPTEN.

The development of the work is divided into two parts. First is the identification of the main parameters of the LFCs, which takes place in Chapter 4. These parameters are intertwined to each other, as with the theoretical development, therefore there is no distinction between materials and methods and the results. For that, each subsection presents its results, when applicable. The parameters studied are the incidence angle modifier curves, the optical peak efficiency and the heat losses curves. Some complementary models had to be developed in order to fully characterize the LEPTEN LFC optically and geometrically, and they are result of the design and construction of this specific workbench. These analyses are presented on sections 4.1.4 and 4.2. The logical strategy used here

can, however, be used for other LFC with similar constructive characteristics.

The analysis performed includes a geometric characterization, in section 4.1, where the behavior of the LFC is evaluated for its geometry, and regarding the variation of the solar angles. The optical performance of the LFC is also obtained in section 4.3 for the condition where the sun vector is perpendicular to the aperture area of the LFC. These aspects are then used to obtain the experimental heat losses for the LEPTEN LFC on section 4.3.1.3, so that its behavior is well understood for the fluid flow analysis.

The second part of the development of the work is a thermo-hydraulic analysis. For that, Chapter 5 gives the material and methods of the model used. This model includes a thermal balance using experimental heat losses and a pressure drop model for both single-phase and two-phase flows. The analysis and results of the model applied to the two LFC benches are presented in Chapter 6. The feasibility of DSG is evaluated, and some modifications are modeled to analyze the prototypes with different configurations. These studies are presented, alongside with the results of the thermo-hydraulic model.

Chapter 7 presents the conclusions drawn from the study for both prototypes, and suggestions for further work for the LEPTEN LFC.

There are six appendixes. Appendix A gives an overview of the works developed by the Heliotérmica group and published or presented so far. Appendix B gives more details on the LEPTEN LFC, showing some steps on the design, conception, construction, control strategy and instrumentation that are omitted from the main work. Although they are not essential for understanding this work, these steps have important experimental value, and the reading is advised. Appendix C shows the equivalent length of the fittings and interconnections between the absorber tubes of the LEPTEN LFC. Appendix D shows an analysis performed over the receiver of the LEPTEN LFC. This receiver has a moving mechanism to compensate the end losses, and although the specific study showed in Appendix D does not directly impact other analysis, its understanding can throw a light on the behavior of this moving absorber system. Appendix E shows the experimental procedure performed to verify the behavior of the flowmeter for conditions different from calibration. Appendix F discusses measurement discrepancies found in some two-phase flow tests and make hypothetical assumptions in order to evaluate them.

2   LITERATURE REVIEW

This section presents a literature overview on solar generation, CSP technology, DSG operational mode, and some main works from literature on these subjects. A thorough review can be seen in (DE SÁ et al., 2018), which is a work developed mostly in Marseille, and counted with the assist of professor Lounès Tadrist, from the Aix-Marseille University, professor Júlio César Passos and the doctorate student Victor César Pigozzo Filho from the LEPTEN laboratory. This paper was published on the Renewable and Sustainable Energy Reviews, and it presents a detailed gathering of relevant works performed on the DSG subject, both theoretical and experimental.

2.1   The Sun

Solar energy is the most abundant resource available for humanity. However, even with its great potential, the use of such energy often does not become economically viable. Compared to other sources of renewable energy, solar energy is characterized as of low-density, and of relatively difficult exploitation. At the moment, it represents only a small part of World energy production, however, in the long term, a rapid rise is expected (LUQUE; HEGEDUS, 2011).

The Sun, when observed from Earth, behaves as a black body irradiating at 5777 K, and the flux density of its radiation, when measured out of the atmosphere for a mean distance between Earth-Sun, is 1366 W/m^2. It was observed that the variation of this intensity was not greater than 0.1 % in a century of measurements, characterizing it as the solar constant (DUFFIE; BECKMAN; WOREK, 2003). However, this value varies during the year according to the distance between the Earth and the Sun. In addition to the intensity of radiation, it is interesting to know the direction in which such radiation reaches a surface on Earth. These solar angles are described in section 4.1.

It is also important to clarify some aspects about the influence of the atmosphere on incident radiation on earth. When solar radiation reaches a plane above the Earth's atmosphere, it has its direction and intensity well known, however, when it penetrates the atmosphere, these conditions change. In a plane on the surface of the earth we can classify three distinct portions of radiation, direct, diffuse and global.

Direct radiation represents the portion that has not been dispersed by air, water molecules, or dust from the atmosphere. It is the radiation

coming directly from the sun without altering its course until it reaches the surface (DUFFIE; BECKMAN; WOREK, 2003). Direct normal irradiation (DNI) represents the direct radiation measured in a plane normal to its direction. The equipment used to measure the direct radiation is the pyrheliometer, and it is designed in a way that the other portion of radiation is shaded from the sensor. This equipment must have a solar tracking device in order to properly track the sun movement.

Diffuse radiation is the portion that has been influenced by the atmosphere. It reaches the observer plane from several directions. The global radiation represents the sum of the direct and diffuse portions. The devices used to measure these portions are the pyranometer, with the difference where diffuse measurements have a device that shades the direct radiation portion from the measurements. For that, the diffuse sensor must also have a tracking device to operate, or at least some periotic correction on the device shading the direct radiation.

All the experimental data used on this work accounted with pyrheliometer measurements, which is the most relevant equipment when working with CSP.

2.2   Solar generation

Solar energy can be converted into electrical energy using two distinct processes: the photovoltaic conversion and by means of thermodynamic cycles (DESIDERI et al., 2013).

The photovoltaic effect was discovered in the year 1839, when the experimental physicist Edmund Becquerel accidentally observed, during an experiment involving an electrolytic cell, that when certain materials are exposed to light it is possible to generate a weak electric current. This effect is the basis of the operation of photovoltaic cells.

This system was later improved by creating the p-n junction (positive and negative), which creates a preferential path for the electrical current, making it viable to harness electrical energy.

Silicon is one of the main materials used in the construction of photovoltaic cells, due to the great amount of information about this semiconductor due to the electronics industry and its abundance in nature.

Governments have an important role regarding the development of these new technologies (SOLANGI et al., 2011). Germany can be mentioned as an example. There, photovoltaic residential installations connected to the grid can sell surplus energy at a higher rate than those of large power generation plants, encouraging small installations. These are

called subsidy rates or premium rates and generally have long-term contracts with pre-established values for the sale of energy.

Photovoltaic technology assumes that solar radiation, composed of discrete energy units called photons, as it strikes the semiconductor material of the panel, causes it to absorb photons from the radiation and deliver a portion of this energy into electrical current.

Photovoltaic systems have advantages over thermodynamic cycles when it comes to domestic applications or micro generation plants, because they are easy to maintain and produce energy without the need for monitoring. However, when the size of the plant is greater than a few MW, a more cautious study is needed, especially for comparing with solar thermodynamic cycles (DESIDERI et al., 2013). So far this technology lacks of an economically feasible, large-scale energy storage system.

Thermosolar systems are the other form of energy generation using solar power, and it has been in development for more than a century. Initially their use was restricted to small applications such as water pumping, in potencies up to 100 kWe (DUFFIE; BECKMAN; WOREK, 2003). These systems have as a working principle to convert solar thermal energy into mechanical energy, generating work, thus producing electric energy.

The thermosolar generation plant usually consists of two interconnected circuits, that can be seen in Figure 2.1. The first is the thermal oil circuit, where solar energy is harnessed by the HTF. This task is performed by solar concentrators that will be discussed on the next section.

The solar field may or may not have a thermal storage system, depending on the application of the plant. Storing surplus thermal energy collected in the solar field can become very useful for supplying thermal energy during daytime transients generated by clouds or shading, or even to generate electricity for hours after the sunset, depending on the size of the system (ORÓ et al., 2012).

There are different types of storage technology:

• Storage in sensible heat energy using both solid and liquid media. The materials used can be concrete, that has low cost, is easy to handle and have high specific heat. Molten salts, mineral and synthetic oils are used as liquid medium;

• Storage in latent heat energy means phase transition on the storage medium, that allows the storage to be done isothermally. The most common form would be the storage in heat of fusion;

• Chemical storage, or chemical reaction potential.

The comparison of feasibility of using the different types of storage systems should take into account both the costs, the amount of storage

and the environmental impacts (ORÓ et al., 2012). In a thermosolar plant, the installation of a storage system can improve both generation performance and dispatchability (BAYÓN et al., 2010).

In the second circuit, the conversion of thermal energy into mechanics and, later, into electric energy, occurs by a Rankine cycle. To this end, heated HTF from the thermal storage is routed to heat exchangers used to heat, evaporate and superheat the water. The superheated steam is used in a turbine to generate mechanical work. The usually saturated mixture at the outlet of the turbine is directed to a condenser. The condensate is then extracted by a feed pump, which increases the condensate pressure before closing the cycle.
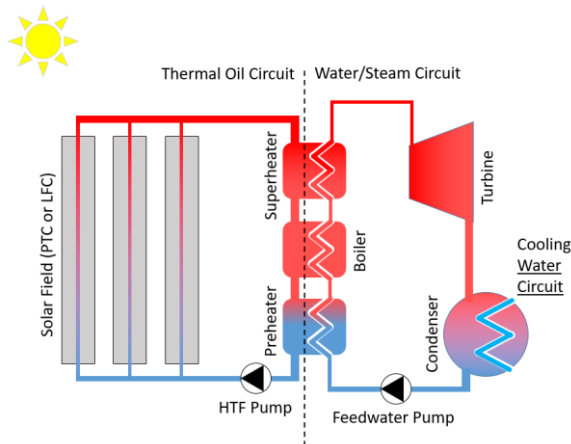
Figure 2.1 - Scheme of a typical heliothermic power plant.

The system actually depends on the configuration of the cycle, which may or may not have a reheating cycle, different numbers of condensate heaters and turbine extractions, among other components.

The power cycle for pure solar plants differs from cycles based on fossil fuels or minerals by experiencing solar transients. They have at least once a day of operation a startup and a shutdown. This is a design challenge for these cycle types since variations of the plant's nominal operation condition strongly influence the efficiency.

Thermosolar systems have some advantages over photovoltaic. Among them is the possibility of installing a thermal storage as discussed before. Another advantage is due to the fact that the solar thermal system presents a lower degradation of its performance throughout its life of operation. Considering a life of 20 years, the degradation stays below 3 %

in relation to the income of its first year, while this degradation is considerably more appreciable for photovoltaic systems (DESIDERI et al., 2013).

Despite the appearance that these two solar conversion technologies are competing against each other for the energy market, they are ultimately complementary. In order to have a solid solar matrix, and to supply the energy demand on both day and night, the two technologies can be used in parallel. Photovoltaic can supply during high radiation periods, while a thermosolar plant with a proper thermal energy storage system can generate energy for hours at night.

2.3   Concentrating solar power

Concentrating solar power technology makes use of mirrors or lenses to concentrate the solar energy. By doing so, these systems can achieve higher temperatures, by increasing the heat flux and reducing the heat exchange area, and therefore reducing heat losses to the environment (PIGOZZO FILHO, 2013). Flat plate solar panels can achieve an operating temperature usually up to a maximum of 100 ºC, while CSP systems can operate at temperatures higher than 800 ºC.

The generation temperature can be classified as low, medium and high. Low temperature systems operate below 100 ºC, and usually are flat plate collectors with either water or air as HTF. Medium temperature is for the range between 100 ºC and 400 ºC, usually using evacuated tubes with concentrators. The generation at elevated temperature is for temperatures higher than 400 ºC, and generally use punctual concentration (PAVLOVIĆ et al., 2012).

The fact that these systems concentrate the solar radiation implies that they must have some tracking mechanism, in order to correct the mirrors with respect to the solar position. Actually, there are some parabolic compound CSP that operates without tracking, however they are small modules and do not have industrial applications. Since the absorber element is on the focus of these mirrors or lenses, only the direct portion of the radiation is useful for CSPs.

The heated HTF from CSP systems have several possible applications, from electrical energy production, steam for industrial processes, cooling, water desalinization, among others. This solar technology can also be hybridized to operate with conventional fired boilers, which increases the dispatchability and reduces investment risks of the CSP. CSP solar fields can also be added to already operational thermal plants or industrial boilers, with the intent to reduce fuel consumption without totally

relying on a renewable source with an uncertain dispatchability. Thermal storage systems also help reduce these uncertainties related to solar transients, such as passing of clouds. In fact, storage systems are one of the great advantages of CSP that may turn the table towards this technology. In 2014 the total electrical production coming from photovoltaics reached around 150 GW, while CSP produced approximately 4 GW, however, due to thermal storage this panorama may change in a near future (PHILIBERT C, 2014).

There are four main CSP technologies nowadays, two of them of punctual concentration, and two of linear concentrations. The punctual concentrations ones are the solar dish and solar tower, and the linear concentration are the parabolic trough and linear Fresnel. The punctual concentration systems have higher concentration ratios; hence they are able to reach higher temperatures.

The radiation on these systems is concentrated to the receiver, inside which there is the absorber element from where the HTF flows. The absorber element usually has a spectral selective surface finish designed to absorb more on the concentrated radiation peak frequency and emit less in the infrared spectrum (DUFFIE; BECKMAN; WOREK, 2003).

The solar dish can be seen in Figure 2.2. They have the appearance of parabolic antennas, and they concentrate the radiation to a receiver mounted on its focus. These high concentration systems can provide a solar concentration rate of up to 1000 suns and temperatures that can exceed 1500 °C. The concentrator is composed of a parabolic disk that tracks the sun on two axes, with the receiver on its focus.
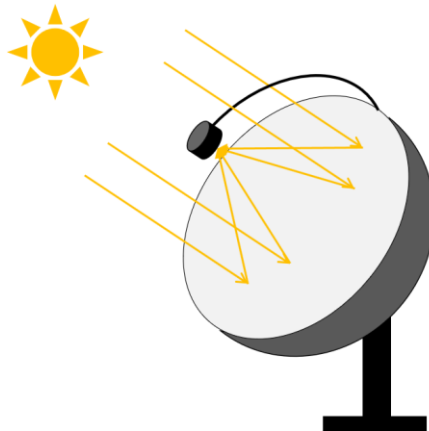
Figure 2.2 - Solar dish CSP system.

Solar dish CSP are usually modular compact systems. They are expensive and the parabolic geometry is hard to manufacture. Therefore, these systems have a specific niche of market, the off-grid installations or military application (MÜLLER-STEINHAGEN; TRIEB; TRIEB, 2004).

The receiver of solar dishes is usually a motor generator, a Stirling or small gas turbine, being the Stirling cycle more efficient but more expensive. Due to its high solar concentration rate, the parabolic disk system has great potential to be used as a concentrator in photovoltaic generation (BARLEV; VIDU; STROEVE, 2011).

Another application of solar dishes is to test new materials for solar application under high concentration. One industrial example of this system is the 10 kW Dish-Stirling developed by the European consortium inside the EURO-DISH project (MÜLLER-STEINHAGEN; TRIEB; TRIEB, 2004).

Solar tower systems, although efficient, are expensive, and are installed only on a few regions of the world so far. Two pioneer solar tower plants were built in the Mojave Desert in the US. These are the Solar One (1981) and the Solar Two (1995), each with nominal power of 10 MWe and have already been deactivated (BARLEV; VIDU; STROEVE, 2011). As can be seen in Figure 2.3, the solar tower system is composed of a central tower with height generally between 75 and 150 m, with the receiver mounted at its top. The tower is located at the center of a solar field, composed by heliostats. These heliostats consist of flat mirrors that track the sun on two axes, each with an area ranging from 8 to over 100 m², distributed around the solar tower.
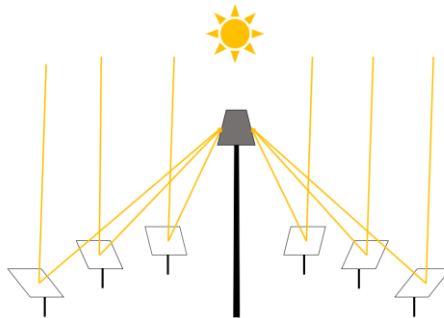
Figure 2.3 - Solar tower CSP system.

This CSP also has high concentration ratios, allowing it to achieve temperatures above 800 ºC. The high temperature HTF can be used to

drive a steam cycle or a gas turbine in combined cycles. This is the most commercially viable punctual concentration technology.

The parabolic trough is the most commercially used CSP technology, with several operational power plants installed (MÜLLER-STEINHAGEN; TRIEB; TRIEB, 2004). Experiments with PTC date back to the 1870, with a solar module built by John Ericsson. It was set to operate with DSG, to drive a steam engine of 373 W. The module had 3.25 m^2 of aperture. John Ericsson later built several other PTC prototypes operating with air as HTF. His death in 1889 prevented the conclusion of a commercial version that was already designed.

The Germans, Wilhelm Maier and Adolf Remshardt, patented the first PTC system commercially used in 1906. It was installed in Cairo, Egypt, in 1912, and it generated steam for a 73 kW pump for irrigation (FERNÁNDEZ-GARCÍA et al., 2010).

Even though several other experiments were performed in CSP, only with the oil crisis in the 70's that this technology reached industrial proportions, with the PTC as pioneer (DE SÁ, 2013). The first milestone for CSP was the Solar Electricity Generating Systems (SEGS) complex, installed in the 1980's in south California, with a capacity of 354 MW (PATNODE, 2006). The research and studies performed on the SEGS made possible to reduce costs up to 30 % regarding operation and maintenance (FERNÁNDEZ-GARCÍA et al., 2010; MÜLLER-STEINHAGEN; TRIEB; TRIEB, 2004).

A scheme of the PTC can be seen in Figure 2.4. This linear concentration system has a reflective parabolic mirror that concentrates the radiation on a receiver, located at the focus of the parabola. The PTC has a one axis tracking mechanism that usually tracks the suns movement from east to west, with the PTC lines oriented on the north-south axis.
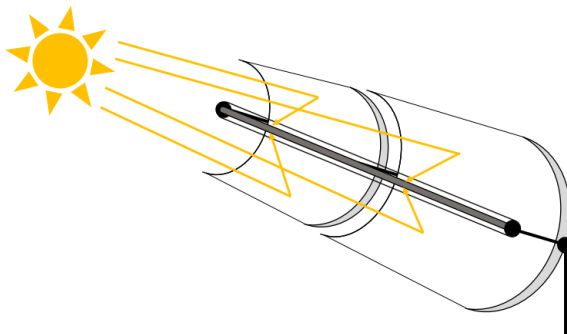
Figure 2.4 – Parabolic trough CSP system.

A stainless-steel absorber tube, with a glass tube external and concentric to it, usually composes the receiver. This glass tube has good resistance and high transmissivity for the working temperature range. To avoid optical loss, the glass has anti-reflective treatment.

The annular region between the absorber metal tube and the glass shell is evacuated, considerably reducing convective thermal losses to the environment. Reports on the functioning of the SEGS show that this vacuum is gradually affected over the years, either by leaks or breakage of the enclosure, or by the diffusion of hydrogen released by the thermal fluid through the absorber element.

At the ends of the collector there are folding elements called bellows that make the insulation between the steel and the glass, also allowing the thermal expansion differentiated of the different materials without damaging such elements. The fixation of the collector in the structure of the collector assembly occurs in the spacing between two bellows.

The LEPTEN laboratory have previously performed both theoretical and experimental works on the PTC technology (DE SÁ, 2013; FILHO et al., 2014; PIGOZZO FILHO, 2013).

The linear Fresnel (LFC) is similar to the PTC. This CSP is the focus of this study. Early works on this technology dates back to 1964, when Francia designed, patented and built the first relevant module in Italy. Several other LFC were designed, built and tested following this first prototype (ZHU et al., 2014). Later in the 1970s, the Department of Energy of the USA (DOE) performed a deep analysis of the LFC indicating that it was a viable CSP for energy production. The LFC however, did not gain the same importance as the PTC on subsequent studies. And even after the oil crisis, the LFC was not the scope of the main studies and projects.

Therefore, the LFC is a relatively new technology, with still a lot of work to be developed before it becomes truly competitive with PTC. It has, however, some advantages in terms of design flexibility and potential of cost reduction (MORIN et al., 2012).

In 2009 the German company *Novatec Biosol* built a plant with LFC called Puerto Errado 1 (PE1), which has a nominal capacity of 1.4 MWe, and its good operation inspired the design and construction of larger plants using this same system (BARLEV; VIDU; STROEVE, 2011).

The LFC works as a PTC that had its parabolic mirror discretized in several lines of flat or slightly curved mirrors. On this technology, there

are therefore several lines of mirrors located near the ground, which reflects the solar radiation to a receiver positioned high above, as seen on Figure 2.5.
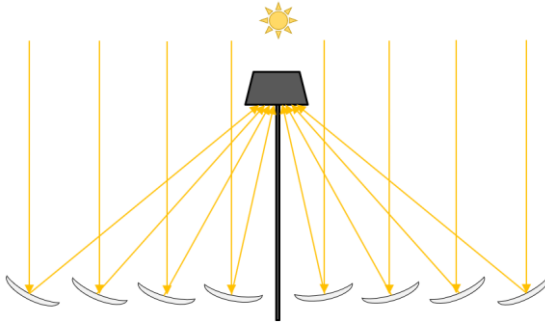
Figure 2.5 - Linear Fresnel CSP system.

By discretizing the parabola, these systems can now have simpler mirrors geometry, easier and cheaper to manufacture. This low-profile mirror lines also represents a smaller wind loads, which impacts on a lighter structure. This configuration also increases the design flexibility, by allowing to simply add or remove rows, changing the nominal power delivered by the collector (BARLEV; VIDU; STROEVE, 2011; MORIN et al., 2012). The Heliotérmica group have performed a parametric evaluation on the LFC prototype configuration, in order to obtain its final design, and the results on this design flexibility can be seen on (BITTENCOURT et al., 2015).

The receiver of the LFC is usually more complex than the evacuated tube of the PTC. Usually they include a cavity, with the absorber element mounted on its interior. Figure 2.6 shows the two main types of receiver found on LFC.
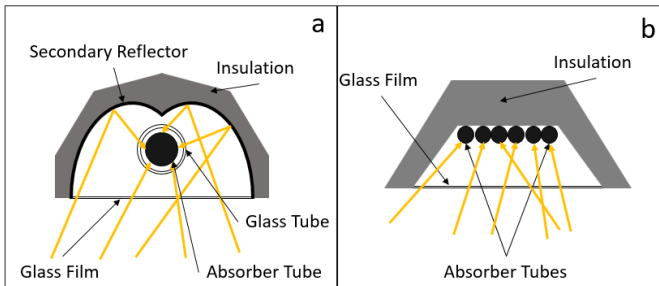
Figure 2.6 - Types of receiver for an LFC.

Figure 2.6 (a) shows a receiver with a secondary reflector that is used usually with a single absorber tube. Since the LFC uses flat or slightly curved mirrors, their focus is not as narrow as the PTC. In addition, the aperture of the mirror lines is usually not perpendicular to the solar radiation, and when it is, the receiver is shading the mirror. This because the mirror must reflect to the receiver, therefore they are in a position where the angle between a normal vector to its aperture and the solar vector is equal to the angle between this normal vector and a vector reaching the receiver. All this results in a wider area of concentrated radiation reaching the receiver. To compensate the radiation that would miss the single absorber tube, a secondary reflector is used, usually with a parabolic compound geometry.

There are two ways to make the thermal insulation on this configuration, one is by using a single evacuated tube, and other is by using a glass film on the bottom of the cavity (Figure 2.6). The two are not used simultaneously. The evacuated tube is a more expensive option, however with better insulation efficiency.

The cavity is not evacuated for the case with the glass film on its bottom. This because the geometry of the glass would result on great stress concentration. The thermal insulation on this case happens by creating a greenhouse effect. Since the heated surface is at the top of the cavity, heat is transferred in the air inside the cavity mostly by diffusion, resulting in reduced convection. The selective coating of the absorber element must be air resistant for this case.

This type of cavity is the one used by the SunCNIM prototype, with a secondary parabolic compound reflector, single absorber tube and a glass film on the bottom of the cavity.

Another type of receiver is showed in Figure 2.6 (b), and it is the same type of receiver from the LEPTEN LFC. This is called a trapezoidal cavity receiver, and it usually operates with several absorber tubes. By doing so, it creates a wider absorber element area, eliminating the need of a secondary reflector. A glass film on the bottom of the non-evacuated cavity does the insulation of this type of receiver.

The multi-tube configuration also presents a better internal convective coefficient when comparing with a single absorber tube with the same hydraulic diameter as all tubes. On the other hand, tubes with smaller diameter presents a higher-pressure drop. This all must be taken into account; however, it shows the wider design flexibility of the LFC.

Usually the heat losses are bigger on the LFC than on PTC, therefore the receiver is a key component in order for the LFC to be even more competitive with the PTC (MORIN et al., 2012).

Both these linear concentration technologies have their advantages and disadvantages, and regardless of which, both have a promising future on the DSG segment. With future research and development, the costs of production an installation will decrease, that will gradually increase the contribution of these technologies on the energy scenario.

2.4   Direct steam generation

Usually solar linear concentrators operate with thermal oil as HTF, and this heated fluid is used to generate steam on a coupled Rankine cycle, as showed in Figure 2.1. This work studies a different concept, called direct steam generation, where the heating, boiling and possibly superheating of the water happens inside the absorber element of the solar field.

The DSG process is not limited by the degradation temperature of thermal oils, and can, therefore, operate at higher temperatures, which increases the overall efficiency (ECK et al., 2011; PATNODE, 2006). It is said that LFC has advantages to operate with DSG when comparing with PTC (MUÑOZ-ANTÓN et al., 2014). One major drawback of the DSG is its harder controllability with respect to thermal oil, which is why more research must be performed in this process in order to better understand what happens inside the absorber tubes during the DSG.

A scheme of a DSG power plant can be seen on Figure 2.7, and it eliminates the need of the heat exchangers.
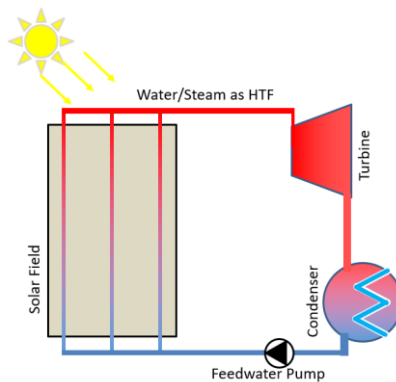
Figure 2.7 - Scheme of a DSG power plant.

In this configuration, the steam is directly routed to the turbine on the Rankine cycle. This concept has advantages from the thermodynamic and economic point of views compared to those using a primary fluid with heat exchangers. Nevertheless, the two-phase flow in the DSG loop must be well controlled to avoid two-phase flow instabilities, high thermal gradients, among other effects.

The steam produced in the solar field can also be used for industrial processes (LOBÓN et al., 2014; LOBÓN; VALENZUELA, 2013). The use of water as HTF is an advantage regarding environmental risks such as oil leaks in the solar field.

All these advantages of DSG over thermal oil can represent a 15 % decrease in energy production costs (FERNÁNDEZ-GARCÍA et al., 2010).

Early works already stated the benefits of DSG. May and Murphy (MAY; MURPHY, 1983), estimated the performance improvement for a DSG PTC system, however, they also stated the additional operational complexities such as reduction on internal wall cooling depending on the flow pattern and two-phase flow instabilities.

Other aspect that must be taken into account is that Steam generation at high temperatures is associated with higher pressures, which implies that the DSG system must be dimensioned to sustain such pressures, increasing the costs of the pipes (ECK et al., 2003, 2011). This also implies on thicker walls, that can lead to higher thermal distributions and higher thermal stress (ALGUACIL et al., 2013; SERRANO-AGUILERA; VALENZUELA; PARRAS, 2014). In addition, the thermal stress caused by the non-uniform concentrated radiation on the outer surface of the absorber tube can be aggravated depending on the flow pattern configuration inside the pipe (LU et al., 2013; ROLDÁN; VALENZUELA; ZARZA, 2013).

There are three main DSG operational mode reported, the once-trough, injection and recirculation (ZARZA et al., 2002), and they can be seen on Figure 2.8.

The once-through, Figure 2.8 (a), is associated to the nominal condition of the plant. Here, the solar field is fed with subcooled water, and the preheating, boiling and superheating happens directly in one passage. This appears to be a simple operational mode, however, experiments showed that controlling the superheated steam condition at the outlet is not a simple task, resulting on a complex and expensive system (VALENZUELA et al., 2006).
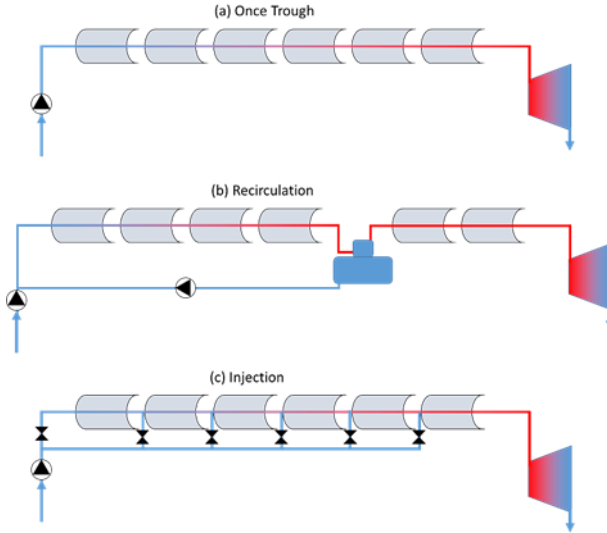
Figure 2.8 - DSG operational modes. Source (DE SÁ et al., 2018).

The injection mode, Figure 2.8 (c), consists basically on the once-through with injections of feed water in several points of the solar line, as a way to control the outlet steam (ZARZA et al., 2002). Tests results proved it to be complex, expensive and unsatisfactory.

The recirculation mode, Figure 2.8 (b), is perhaps, the most viable one. Here the solar field is divided into two sections, one for the preheating and boiling, and the other for the superheating.

In the left part of Figure 2.8 (b), saturated liquid exits the steam separator and is pressurized by the recirculation pump. After, this HTF is mixed with liquid from the condenser, before entering the solar field. There, the now subcooled liquid is heated until saturation, and after until it becomes a two-phase mixture. This mixture is then re-routed to the steam separator, closing this cycle. If the DSG system only operates with saturated mixture on its outlet, then only this left part of the scheme is considered. Both the LEPTEN and the SunCNIM prototypes operates similarly to this.

For superheated systems, the saturated steam from the steam separator is then directed to the superheating section of the solar field, and then to the turbine. There are also injections of feed water at this superheating section, in order to control the outlet steam. This last operational mode presented as highly controllable, however, with more parasitic loads due to the higher recirculation rates (VALENZUELA et al., 2006).

Most studies on the DSG subject considers the recirculation mode (AUROUSSEAU; VUILLERME; BEZIAN, 2016). Some operational examples can be found. The PTC Thai Solar One operates in Thailand in recirculation mode since 2011. It presents a good stability; however, high transients lead to some flow instabilities between parallel loops. Puerto Errado 1 and 2 are two LFC plants that also operate with recirculation mode, and they presented good control stability even on high transients.

2.4.1   Two phase flow

The DSG operation is associated with two-phase flow, and it is necessary to study this subject to better understand what is happening in the absorber tubes. Two-phase flow occurs when there is a simultaneous flow of two different phases, with an interface separating them. In the case of the DSG these two phases are saturated liquid water and saturated steam.

The two-phase flow is classified according to the flow patterns. They represent the way in which the interface is arranged within the flow. The identification and classification of these flow patterns is important, because they indicate what is physically happening in the absorber tube. The convective coefficient and the pressure drop changes depending on the flow pattern.

Experiments with the objective to identify flow patterns date back to the early 1940s. Those were flow-visualization experiments and the classification of the most typical horizontal flow patterns can be seen in Figure 2.9 (VIJ; DUNN, 1996).

The void fraction showed in Figure 2.9 is the time-average fraction of how much of the tube cross section is occupied by steam. There, the flow patterns are divided into two categories, one with a continuous flow of steam, and another where the flow of steam is separated in volumes by liquid. Usually the division is around a void fraction of 0.5.

Some aspects must be known about the two-phase flow. The split velocity is a relation between the vapor and liquid velocities, and it also influences the flow pattern. As an example, for low vapor velocities and high void fractions the stratified flow regime is commonly found. With the increase of the vapor velocity there is an agitation of the interface due to shear flow, surface tensions and liquid vapor density. These effects may cause the flow pattern to shift to a wavy flow. This agitation makes the liquid to climb the inner walls of the tube, and with the adequate velocity

the flow may become annular. The annular flow pattern is the most desirable for DSG, because it wets the entire inner surface of the tube, achieving better heat transfer coefficients.
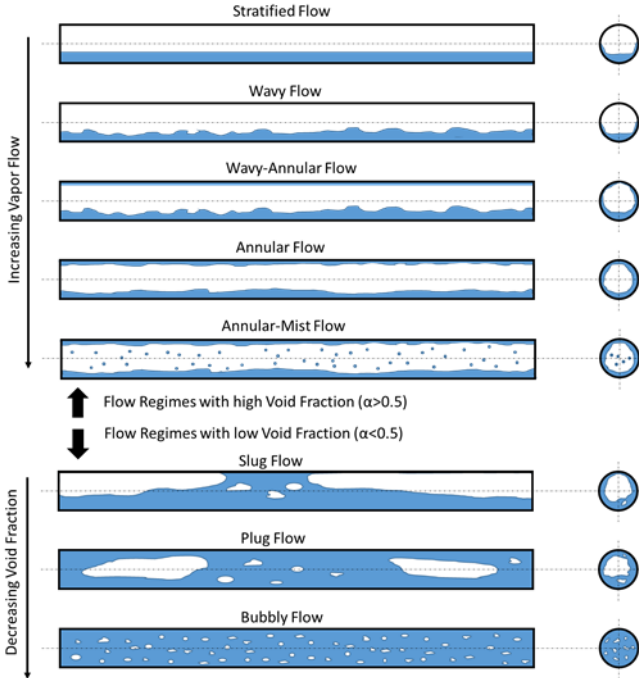
Figure 2.9 - Flow patterns in a horizontal pipe. Source: (DE SÁ et al., 2018).

There are flow charts that attempt to correlate the properties of the flow with the flow pattern. Several of these charts can be found in literature. The horizontal is of interest for DSG. Taitel and Dukler's flow map is an early example (TAITEL; DUKLER, 1976). It was first published in 1976, and it was developed for horizontal gas-liquid flow in tubes. Another example is the Kattan and the Steiner, showed in Figure 2.10, developed for R-410A at a saturation temperature of 5 °C (WOJTAN; URSENBACHER; THOME, 2005a). The horizontal tube here had a 13.84 mm internal diameter. Three surface heat fluxes are compared on this diabatic map, 7.5, 17.5 and 37.5 kW/m². The influence of the wall heat flux on the flow pattern is an important effect to take into account when studying DGS on solar concentrators.

The two-phase flow differs from horizontal to vertical due to gravitational effect. For horizontal flow this effect tends to separate the steam to the upper part of the absorber tube, as seen on Figure 2.9. Usually the two-phase flow models analyses aspects such as pressure drop, heat transfer, flow pattern and phase change rate. These parameters are interconnected (VIJ; DUNN, 1996).

For a DSG system, the pressure drop and heat transfer are of utter importance, especially if the heat losses are not experimentally obtained. Both parameters, however, are associated with the flow pattern and phase change rate. All these quantities change throughout the pipe.
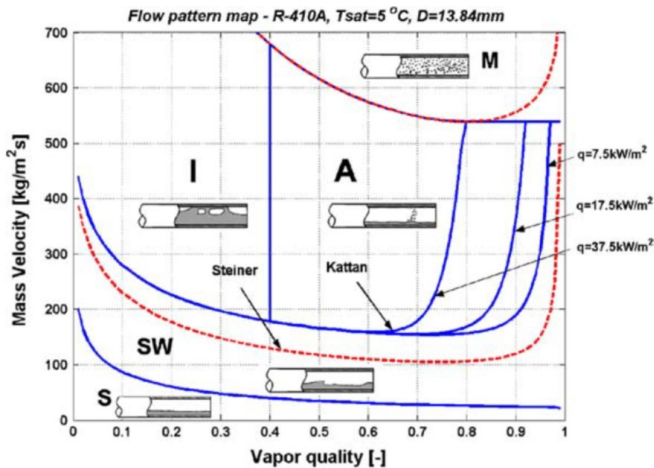
Figure 2.10 - Horizontal flow pattern map of Kattan and Steiner, considering different wall heat fluxes. Source: (WOJTAN; URSENBACHER; THOME, 2005a).

The two-phase flow can be approached by different ways. One is to stem from the fluid mechanics equations in their general form. For that, it is considered that fluid is a continuous medium and the physical variables denoting the thermal and dynamic state of the fluid are well defined.

Two types of conservation laws are then used. The first type are the fundamental conservation equations of mass, momentum and energy, and they describe the hydrodynamics of the HTF. The second type is the constitutive, which relates the velocity field to the stress field and the heat flux field to the energy field (VIJ; DUNN, 1996). When applied in a three-dimensional time-dependent form they should be able to predict the flow condition. However, there are no analytical solutions for these equations, therefore simplifications are made and they are solved numerically. For

that, computational fluid dynamics methods are usually applied. This approach is usually only suited for the simplest two-phase flows, and it is not the case for a DSG system. Few very simplified cases of DSG are analyzed in this manner (DE SÁ et al., 2018).

There are other methods that simplify the conservation equations, in order to achieve a solution. The simplest is the homogeneous model, where the two phases are considered both in thermodynamic equilibrium and flowing at the same velocity. The flow properties are the weighted average property of both phases. This model is suited for simpler flows, with either very low or very high void fractions. In these cases, one phase is highly dispersed in the other, such as the case of the bubbly flow or mist flow.

Another simplified model is the separated-flow. It considers the split between phases, allowing evaluating the velocity of each flow separately. The conservation laws are written for the control volume, and both phases are considered in thermodynamic equilibrium. In order to solve the conservation laws, correlations are used. One of them, that is also used in the model developed on this work, is the Lockhart and Martinelli (LOCKHART; MARTINELLI, 1949). For this correlation, a two-phase multiplier is proposed in order to compensate the wall shear stress of a single-phase liquid flow. In order to solve the energy equation, correlations are used to obtain the two-phase Nusselt number as well.

Another model, called the two-fluid model, considers the conservation equations separately for liquid and vapor, therefore, they may not be in thermodynamic equilibrium. The two-phase multiplier is not needed in this model, although it requires models to treat the exchange of mass, momentum and energy between the phases at the interface, as well as the information about the flow pattern (VIJ; DUNN, 1996).

2.4.2   Review of the works found in literature

The most used technology for DSG is the PTC collectors, same as for thermal oil plants. The main experimental work on this subject is the DISS (Direct Solar Steam) project, which consists on a workbench of PTCs operating in DSG. This set-up is located at the Plataforma Solar de Almería (PSA), Spain, and it was developed between 1997 and 1998. The main results of the project can be seen on (ZARZA et al., 2004). This project proved the feasibility of DSG process using PTCs and it represented a great milestone on the DSG technology.

Overall, the LFC presents a lower optical efficiency when compared to the PTC. However, LFC has some advantages, such as lower

wind loads due to the low mirror profile, less expensive manufacture due to the simpler mirror configuration and it presents a more versatile design that can be best adjusted for each plant requirement (BARLEV; VIDU; STROEVE, 2011; MORIN et al., 2012).

The LFC technology is still relatively new and has to walk a long way to reach the maturity of PTC. For that this technology needs further research. The feasibility of the DSG process in PTC has been already proved in the DISS project (ZARZA et al., 2004), and now efforts have being made in assessing the reliability for DSG in LFC.

Several works have been performed regarding DSG in solar concentrators. Eck et al. (ECK; STEINMANN; RHEINLÄNDER, 2004) studied the influence that the inclination of the receiver has on the two-phase flow, also verifying the wall temperature using ANSYS. The DISS facility was studied, and it was found that although some inclination helps maintaining an annular flow, it was not necessary to guarantee a safe operation without a great thermal distribution on the wall of the absorber.

Eck and Steinmann (ECK; STEINMANN, 2004) developed a DSG model in Matlab®. It considered the two-phase flows most encountered in the DISS facility, the wavy and annular flows. The distinction between them is found through an empirical correlation based on the mass flow rate. The Friedel pressure drop correlation was used (FRIEDEL, 1979). This was found to have a good agreement with the DISS experimental data. The same Friedel correlation was used in the works of Pye et al., Montes et al. and Sun et al. (MONTES; ABÁNADES; MARTÍNEZ-VAL, 2010; PYE; MORRISON; BEHNIA, 2006; SUN; LIU; HONG, 2015). Valenzuela et al. and Lobón et al. also used the Friedel correlation on models developed in Matlab/Simulink® (LOBÓN; VALENZUELA, 2013; VALENZUELA; HERNÁNDEZ-LOBÓN; ZARZA, 2012).

According to the experimental investigations of Eck et al. (ECK et al., 2008), the ideal operational range for the steam separator, on a DSG plant operating in recirculation mode, is with a steam quality on its inlet around 0.7 to 0.8. The experimental setup used was the DISS facility, with different steam separators installed and tested.

Xu and Wiesner (XU; WIESNER, 2015) developed an unsteady, one-dimensional, and closed-form solution for DSG with PTCs.

Elsafi (ELSAFI, 2015) used the flow pattern based pressure drop model proposed by Quibén and Thome (MORENO QUIBÉN; THOME, 2007a, 2007b) to analyze the DISS facility. This model is also used in the present work.

Biencinto et al. (BIENCINTO; GONZÁLEZ; VALENZUELA, 2016) developed a PTC model using TRNSYS capable of performing fast

simulations and evaluating transient periods. This approach permitted a reasonable accuracy for fast simulations. The collectors were modeled in FORTRAN using a one-dimensional approach. It takes into account the thermal inertia of the fluid mass and pipe mass.

A library was developed in Modelica to perform transient studies on two-phase flow in horizontal receivers. Several works used Modelica to develop their models (BIRNBAUM et al., 2011; ECK; HIRSCH, 2007; HIRSCH; STEINMANN; ECK, 2005).

Light water reactor evaluation software was also used to study the two-phase flow behavior of the receiver in DSG. Moya et al. and Aguilar-Gastelum et al. used RELAP (AGUILAR-GASTELUM et al., 2014; MOYA; VALENZUELA; ZARZA, 2011), while Hoffmann et al. opt to use ATHLET (HOFFMANN et al., 2014).

The present work used a flow map developed by Wojtan et al. (WOJTAN; URSENBACHER; THOME, 2005a, 2005b), to analyze the flow pattern inside the tube. It used different pressure drop correlations, including the phenomenological model proposed by Quibén and Thome (MORENO QUIBÉN; THOME, 2007a, 2007b). Other two-phase pressure drop correlations are also used. The results were compared to experimental data from the DISS project. Later the model verified with the DISS data was used on a prototype LFC plant from SunCNIM and the LEPTEN LFC prototype.

2.5   Partial Conclusions

The generation potential of the sun is stated, and it was seen that the CSP technology could make a proper use of this potential. Inside the CSP technology, the DSG operational mode allows systems to achieve higher efficiencies, since water is not limited at an operation temperature of 400 ºC as much of the commercial thermal oils. It also eliminates the need of heat exchangers. However, DSG is a relatively new technology, and there are studies being performed in order to increase the knowledge on this operational strategy.

A major milestone on the DSG was the DISS facility (ZARZA et al., 2004), which has proven the feasibility of DSG on PTC, alongside clarifying several operational aspects on this operational mode.

The experimental data from DISS allowed verifying models of two-phase flow on evacuated absorbers (AGUILAR-GASTELUM et al., 2014; ECK; HIRSCH, 2007; MOYA; VALENZUELA; ZARZA, 2011; XU; WIESNER, 2015) and models for different operational control strategies (VALENZUELA et al., 2005, 2006).

Components of the solar field were also analyzed due to the higher operational pressure and temperature with respect to thermal oil solar plants (ECK et al., 2008, 2011). Safe operation was found, although extra care is required due to complexities added by the two-phase flow.

It was also experimentally verified that the most reliable and stable operational mode is the recirculation (ECK et al., 2003; ZARZA et al., 2004), although early works had different expectations (LIPPKE, 1996). For the tube diameter used on the DISS, it was mainly found wavy and annular two-phase flow (ECK; STEINMANN, 2005).

Regarding the models seen on literature, several correlations were used to analyze the two-phase flow on DSG systems, however, Pye et al. (PYE; MORRISON; BEHNIA, 2007) states that the Friedel presented the best fit for the DISS pressure drop experimental data.

The models found approach the heat losses on different manners, some used a semi-analytical analysis (ODEH; MORRISON; BEHNIA, 1998; RUSSELL, 2003; YAN et al., 2010), some considered an empirical heat loss curve found experimentally (ECK; STEINMANN, 2005; FRAIDENRAICH et al., 2013; ROLDÁN; VALENZUELA; ZARZA, 2013).

Much work has already been done regarding DSG, however, there are still miles to go for deeply understanding it in both a practical and theoretical manner. For an industrial point of view there are aspects such as the development of new materials and components adequate to operate at a solar field at high temperature and pressure. Selective paint and design of solar fields can be improved. At higher operational temperatures, the insulation of the absorber elements must also be enhanced, to compensate for the bigger role that heat losses get.

Overall, due to the versatility that CPS operating with DSG have, to either generate electricity or steam for processes, a prosperous future is expected for these technologies.

64

3   DESCRIPTION OF THE EXPERIMENTAL BENCHES

The present work studies two different experimental benches, both LFC prototypes. One is the LFC from the French company SunCNIM and the other is the workbench developed by the LEPTEN laboratory, from the Federal University of Santa Catarina.

3.1   SunCNIM LFC

The prototype from SunCNIM consists of a module of LFC operating in DSG, with saturated mixture at the outlet. It is located at La Seyne-sur-Mer, in south France. A description of this LFC is presented in this section, although the specific details of the prototype are omitted due to a confidentiality agreement with SunCNIM. The prototype is operational since 2010, and it can be seen in Figure 3.1 (SUNCNIM, 2018).

Figure 3.1 - Prototype from SunCNIM. Souce: (SUNCNIM, 2018).

This LFC has 14 lines of slightly curved mirrors, with a total mirror area of 719 m^2, and a trapezoidal cavity receiver with secondary parabolic compound reflector, closed by a glass film on the bottom. The receiver is fed with subcooled water and operates in partially open loop, where the steam generated passes by an expansion valve and then is purged to the environment. A steam separator, located at the outlet of the receiver, separates the steam from the condensate. For recirculation, the saturated liquid extracted from bottom of the steam separator is mixed with fresh wa-

ter, to compensate for the mass of steam lost to the environment. The operational pressures vary from 25 to 75 bar, which the saturation temperature on the outlet are of around 224 to 290 ºC.

There are two means to evaluate the temperature at the outlet of the receiver, one is by a thermocouple installed, and the other is by obtaining the saturation temperature using the measured pressure in the steam separator. The insulation of the thermocouple from the outlet of the receiver was compromised by the concentrated radiation, leading to uncertain measurements. Therefore, the pressure measurements are used in calculations to evaluate the saturated temperature on the outlet of the receiver.

The water level at the steam separator is practically constant and considered so in calculations. The inlet mass flow rate measurement is the same as the recirculation, which considers the condensate coming from the steam separator plus the inlet of raw water to compensate for the steam lost to the environment.

The inlet temperature measurement is performed almost on ground level, before the flow rises to reach the absorber. There is a considerable height difference from the measurement point to the inlet of the receiver. The use of the measured temperature as inlet temperature neglects the heat losses on the flexible hose that leads the flow to the receiver. This conservative approach is tolerable, because it leads to an overestimation of the inlet temperature, resulting on a lower performance of the collector.

Five days of operation of the LFC were analyzed, the 21, 23 and 24 of July, and the 19 and 21 of September of 2015. The recorded experimental data was provided by SunCNIM.

3.2 LEPTEN LFC

The LEPTEN LFC is a workbench to study the viability of this type of technology, locally developed and manufactured, that operates with DSG. This prototype can be seen in Figure 3.2, and it was entirely designed and constructed by the Heliotérmica group from the LEPTEN laboratory inside the project Heliotérmica CNPq (Proc. 406357/2013-7). An overall description and preliminary analysis of the workbench and initial results can be found in (PIGOZZO FILHO et al., 2018).

In parallel with the LFC workbench, an indoors experimental bench was set up as part of the Master's project of a member of the Heliotérmica group, with the intent to estimate the heat losses of the receiver. This analysis and its results can be found in (SOUSA et al., 2017).

Figure 3.2 - LEPTEN LFC prototype.

The present doctorate study started at the same time as the Heliotérmica project. Hence, all the steps around the conception, design, construction and control strategy were part of it. The thesis, however, is focused on the optical, parametrical and thermal characterization of the LFC, and on a thermal analysis of the HTF, therefore the details of the project, construction and operation of the workbench are omitted.

Appendix B shows a more detailed description of the LFC workbench. Although this description is not essential for understanding the analysis further developed, it gives an important insight of the large experimental work performed. There, steps are displayed such as the project and conception of the LFC, the construction and mounting of the curved mirrors and receiver, the tracking system development, among others. This section gives only a brief view of the LEPTEN LFC.

The first step inside the project was to design the LFC with satisfactory geometrical efficiency and viable costs. For that, the Heliotérmica group developed a Monte Carlo Ray Tracing (MCRT) software in Matlab, that allowed to automatically change these parameters either one at a time or several at a time (BITTENCOURT et al., 2015) (BURIGO et al., 2015). The final configuration of the workbench, as seen on Figure 3.2, is an LFC of 5 m x 12 m, with ten mirror lines, each containing 12 mirrors of

1000 mm x 450 mm. The total mirror area is of 54 m². The spacing between mirror lines is equal for all lines. The receiver was set on a multi-tube trapezoidal cavity configuration, with 346 mm of aperture on its bottom, and located at a height of 3.75 m.

The LEPTEN LFC uses flat mirror modules, cold bent to a small curvature. Each module has 1000 mm x 450 mm of common mirrors locally manufactured to reduce costs.

A trapezoidal cavity with multi-tube configuration was adopted as the receiver. This component is the most important for the present work, for it represents the testing section itself. It is inside the absorber element of the receiver that the HTF will absorb heat from the concentrated radiation, and in some tests, change from subcooled liquid to a saturated mixture. The absorber element is composed by six tubes of 25.40 mm of outside diameter (OD), totaling a width of 152.40 mm (i.e., 6 x 25.4 mm). Figure 3.3 shows a front view of the receiver being fixed on the workbench, without the absorber element.

A flat glass plate of high transparency is positioned at the lower part of the cavity in order to minimize the convective losses to the environment while allowing the entrance of the solar irradiation. This glass was commercially found as the type "Extra Clear Diamond".

Figure 3.3 - Front view of the trapezoidal cavity receiver without the absorber element.

The interconnections of the absorber tubes are done by means of flexible stainless-steel hoses. To fix these hoses on the tubes without interference, some angular extensions were welded on the extremities of the absorber tubes. The HTF flows circularly on the receiver, passing by all the absorber tubes one time. It enters the receiver by the first absorber tube, at the south extremity of the workbench. It flows first at the more

peripheral tubes, and last at the middle tubes, exiting by the fourth tube also at the south extremity of the workbench. Mode details of this configuration can be seen in Appendix B and Appendix C.

The receiver is fixed at the bench structure by two rails, which allows it to move to south and north direction as seen in Figure 3.4. This innovative design was developed in order to compensate the end losses during tests, and it is discussed in more detail on Appendix D, where this system is analyzed throughout one year.

Figure 3.4 - Fixation of the receiver on rails.

The six absorber tubes were coated with a selective ink. The ink used was the SOLKOTE, from the American company SOLEC (SOLEC, 2018). According to the manufacturer the mean emissivity and the absorptivity range from 0.20 to 0.49 and 0.88 to 0.94 respectively, depending on the substrate and the thickness of the paint layer. The thickness of the paint depends on how many ink spray passages are given. The ink operating temperature ranges from -73 °C to 538 °C.

The absorber was instrumented in three sections: beginning, middle and end. In each of the six tubes there are measurements made directly on the fluid. Figure 3.5 shows a scheme of the absorber tubes instrumentation.

Humans on left.

Figure 3.6 - Scheme of the hydraulic system.

Water exits the steam separator also by its lower part, to ensure that even in two-phase flow tests, only condensate is being routed to the pump. Before reaching the pump, there are three routes that the HTF can pass. It can go directly to the pump, it can go first to the condensers, or it can be divided and a fraction goes to the condensers while the other passes directly to the pump. The condensers installed in by-pass are used for some single-phase tests, where maintaining a stable lower temperature was needed.

At the outlet of the pump the HTF passes by the flowmeter. This configuration was chosen because the flowmeter is of the turbine type, so any air or vapor bubbles would cause a variation on the measurements. For the two-phase flow tests, the HTF exiting the steam separator is at the saturated condition, and if it would go directly to the flowmeter it could carry small bubbles or create them due to pressure drop on the pipes and on the flowmeter. For that, first the pump promotes a pressure increase on the HTF, taking it to a subcooled liquid state. The flowmeter used is the FTB-1424-HT from Omega©, and it was calibrated for water at ambient temperature. No calibration laboratory found would calibrate it for subcooled liquid water up to 230 ºC.

In that manner, an experimental verification procedure of the flowmeter behavior was performed for higher temperatures. This experimental

procedure was made using the LEPTEN LFC hydraulic and control structure, and its details and results can be seen on Appendix E.

After passing through the flowmeter, the subcooled HTF passes by an electrical preheater before it finally reaches the receiver on the solar field. This electrical preheater is a pressure vessel with a flanged multi-tubular 20kW electrical heater coupled. This equipment can be used for different ends. It can speed up the beginning of the test, helping the system to achieve the desired HTF temperature faster. It can also just maintain a stable inlet temperature condition for the HTF entering the receiver, helping achieve steady state conditions. It can also be used on the two-phase flow tests to put the subcooled HTF exiting the pump closer to the saturated condition before it enters the receiver. The control of the electrical preheater was done by a PID (proportional-integral-derivative) logical controller.

After exiting the solar field, the HTF is routed again to the steam separator, finishing the cycle. If the tests are single-phase then this is the end of the HTF cycle. For the two-phase flow tests, the steam generated is purged from the system by the control valve. The pipe line that goes to the control valve exits the steam separator from its top part, to prevent condensate to enter the line. This pipeline is then directed downwards for the connections and valves to be in a height easier to access for installation, inspection and possible maintenance.

The control valve is located just after a safety valve, that is set to open if the pressure on the system surpasses 23 bar. The control valve is responsible for setting the internal pressure of the steam separator.

The hydraulic system also includes temperature measurement of the HTF in several points such as before and after the pump, after the preheater, after the condenser and after the control valve. There are two pressure measurements, one just before the HTF enters the receiver, and another before the fluid re-enters the steam separator.

The workbench also counts with several additional auxiliary equipment for data acquisition, power supplies, PID controllers, two-phase and three-phase current supply, frequency inverter, among others. Overall the LEPTEN LFC is a complex bench, result of four years of dedicated work from the Heliotérmica group.

3.3 Partial Conclusions

The SunCNIM workbench, located at La Seyne-sur-Mer, in south France, is an LFC of industrial proportions, already in operation for several years. It has 14 lanes of slightly curved mirrors, and the trapezoidal

cavity receiver has a secondary parabolic compound reflector, insulated by a glass film on its bottom. This prototype operated in partially open loop, where the steam was purged and the condensate was recirculated, with fresh feedwater entering the system to compensate the steam outlet.

The instrumentation and operational details were not part of the present work. The measurements used were provided by SunCNIM.

The LEPTEN workbench, installed at the Federal University of Santa Catarina, south Brazil, represents a small scale LFC prototype that could also supply steam for industry, however for lower temperature demands as the one from SunCNIM. The maximum pressure level allowed by the system is of 23 bar.

This LFC has 5 m x 12 m of area, with 10 mirror lines of 450 mm of width. It operates with a trapezoidal cavity receiver with a height of 3.75 m, with six parallel tubes as absorber element.

The Heliotérmica group performed the experimental control and measurements.

Both experimental apparatuses provided important measurements regarding DSG in LFCs, and the LEPTEN bench also provided essential single-phase flow measurements. All these experimental data are used on subsequent analysis.

4 CHARACTERIZATION OF THE LINEAR FRESNEL CONCENTRATOR

This section describes the optical and thermal characterization of an LFC. At rigor, this chapter should be separated between materials and methods and results, however, since some parameters are intertwined with each other, the results are presented just after the theoretical basis. This dependency between parameters is stronger at section 4.3, where the calculations are iterative, and even the theoretical analysis of the incidence angle modifier (IAM) have experimental dependency for the LEP-TEN case.

The procedures here described can be used to identify the main parameters of the workbenches. They are the optical peak efficiency (η_{0^o}) and the heat loss ($\dot{Q}_{HL}$) curve of the receiver. These parameters can be seen on equation (4.1), which describes the heat absorbed by the working fluid.

$$\dot{Q}_{abs} = A_m \, DNI \, \eta_{0^o} \, IAM - \dot{Q}_{HL} \qquad (4.1)$$

This equation comes from an adaptation from the quasi-dynamic test method (QDT) approach to an LFC. The QDT of the thermal performance of the collector is described as Equation (4.2) by EN12975-2 (HEIMSATH et al., 2014).

$$\frac{\dot{Q}_{calc}}{A_{ap}} = F'(\tau\alpha)_{en}K_{\theta b}(\theta)DNI + F'(\tau\alpha)_{en}K_{\theta d}G_d - \dot{Q}_{HL} \qquad (4.2)$$

This equation is applicable for flat plate collectors and had to be adapted for CSP. The aperture area A_{ap} is considered a net aperture area for CSP, and has different definitions depending on the technology. For parabolic through concentrators the net area changes with regard to the incidence angle, and for LFC it is considered fixed as the total area of primary reflectors A_m (HEIMSATH et al., 2014).

The first term of the right side of the equation (4.1) is related to the direct normal irradiation (DNI), and the second related to the diffuse radiation (G_d). Since the influence of the diffuse radiation on a CSP is very small, this term is neglected. The energy conversion factor, represented by $F'(\tau\alpha)_{en}$, is also changed to the optical efficiency. $K_{\theta b}$ and $K_{\theta d}$ represents the incidence angle modifier for a flat plate collector. For the present case, the optical efficiency includes the zero incidence efficiency

(η_{0^o}) and the factorized IAM. It could also include the end losses (η_{endL}), however this term is already included on the transversal IAM for the cases analyzed. The heat losses to the environment are represented by $\dot{Q}_{HL}$.

The incidence angle modifier is divided in two components, in the transversal and longitudinal directions. These two parameters were obtained using the software SolTrace, as described in Section 4.1.

4.1   Characterization of the incidence angle modifier

The optical efficiency of solar concentrators changes with the variation of the sunray angle direction. This efficiency variation is of utter importance in order to correctly characterize the solar concentrator. The first step in this characterization is to understand the angular relations of the sunray vector, and to be able to track the movement of the sun across the sky. In that manner, the geographical information about the LFC site is needed. The prototype from SunCNIM is located in La Seyne-sur-Mer, and the exact latitude and longitude were provided by SunCNIM. The LEPTEN workbench is located at the Federal University of Santa Catarina, with a latitude of -27.60° and a longitude of -48.52°.

The sunray vector is defined by two solar angles. One is the solar azimuth (γ_s), which is the angle between the north and the sunray projection on the horizontal plane, counted eastward from 0° to 360°. The other is the zenith angle, θ_Z, which is the angle between the sunray vector and the vertical line (Figure 4.1).

For the case analyzed of horizontal aperture, the zenith angle is equal to the incidence angle. Other angle that can be used to describe the solar position is the solar altitude angle, which is complementary to the zenith angle ($\alpha_s = 90 - \theta_Z$), (DUFFIE; BECKMAN; WOREK, 2003).

It would be needed to measure or simulate a solar concentrator for a wide range of different sunray angles to fully characterize its optical performance with respect to the sunray angle. However, the concept of the incidence angle modifier, IAM, was introduced as a way to reduce the quantity of experimental measurements or simulated points.

The IAM is a curve, or set of curves, used to reproduce the changes in efficiency with the variation of the sunray angle. The IAM uses the zero optical efficiency (η_{0^o}) as reference, which is the optical efficiency at zero incidence angle. Instead of making several measurements, usually only a few points are analyzed and the curve is fit to it. This effect can be seen on equation (4.1).

Due to the tracking and geometry, for a PTC there is only one incidence angle projection needed, usually with respect to the longitudinal plane of the collector (for north-south axis orientation). However, LFC have a more complex definition to characterize the incidence angle influence, and two projections are needed. This because all rows of mirror have different inclination, and their aperture are almost never perpendicular to the sunray, and when they are, that means that the receiver is blocking them.

In that manner, for LFC the IAM is divided in two curves (equation (4.3)), each representing the optical efficiency variation on a different direction, the longitudinal and the transversal (GIOSTRI et al., 2012). This concept of separating the IAM was first introduced by McIntire (MCINTIRE, 1982), and was called the McIntire factorization. At first, by using the McIntire factorization the IAM was divided in curves, function of the transversal angle (θ_T) and longitudinal angle (θ_L). The transversal angle is the angle between the sunray vector projection on the transversal plane to the zenith, and the longitudinal angle is the angle between the projection of the sunray vector to the longitudinal plane with the zenith.

Figure 4.1 shows the angular representation of the sunray and the angles used on the IAM factorization. In that case, instead of obtaining experimental data for an entire hemisphere over the collector, only some incidence angles over two symmetric planes are needed to characterize the optical performance.

$$\text{IAM}(\theta_Z, \gamma_s) \approx \text{IAM}_T(\theta_T)\,\text{IAM}_L(\theta_L) \tag{4.3}$$

The LFC IAM curve may vary to include or not the end losses, however it also includes cosine effect, primary mirrors mutual blocking and shading, secondary reflector and support shading, specular reflection deviations, sun shape effects, the impact of material optical properties, etc. Experimental measurements includes also tracking errors (GIOSTRI et al., 2012; HORTA; OSÓRIO, 2014).
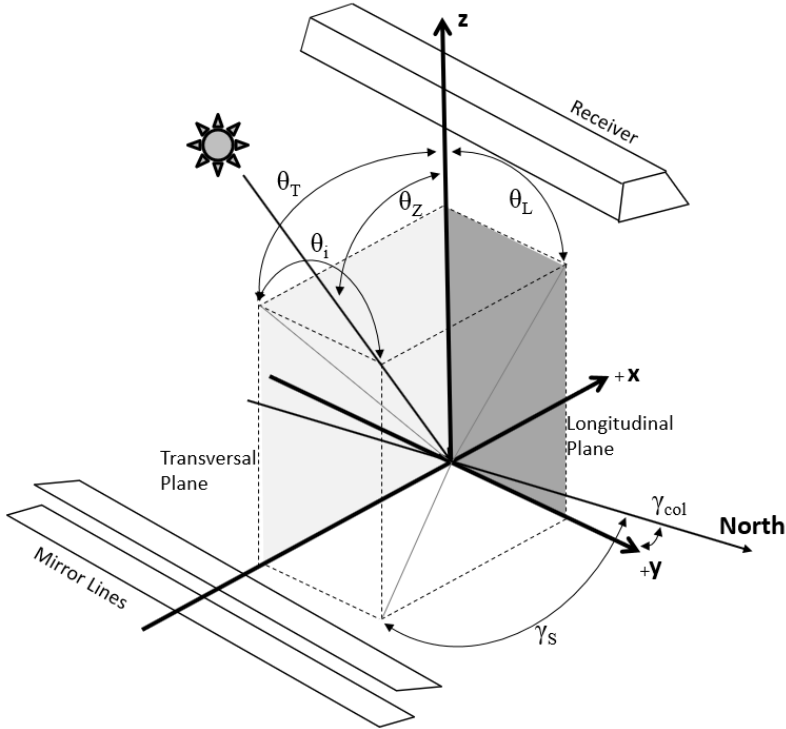
Figure 4.1 - Sunray angles and relations with reference planes used on IAM factorization. Adapted from: (HEIMSATH et al., 2014).

In this case, this procedure introduced some errors by factorizing parameters that are non-factorable, such as the end losses or the cosine effect as seen in equation (4.4) (HERTEL; MARTINEZ-MOLL; PUJOL-NADAL, 2015). The errors however, were found within a tolerable limit for most cases, because the largest errors occur with large incidence angle, which has a lower radiation income.

$$\cos \theta_Z \neq \cos \theta_T \cos \theta_L \qquad (4.4)$$

Later a new concept was defined, where the longitudinal IAM is a function of the incident angle (θ_i), which is defined as the angle between the sunray vector and its projection on the transversal plane, as showed in Figure 4.1. This simple modification on definition added some great advantages without requiring additional simulation or experimental measurements.

Hertel et al. (HERTEL; MARTINEZ-MOLL; PUJOL-NADAL, 2015) state that using the θ_i instead of θ_L increases the accuracy of the factorization. This because although most of the IAM effects are not factorable on the $(\theta_T - \theta_L)$ space, some of these become factorable in the $(\theta_T - \theta_i)$ space such as the end losses and the cosine loss. These two factors are the main cause of efficiency loss on high incidence angles. The fact that they are now factorable increases the precision on the IAM representation of the actual collector.

The end losses effect has a relation with the longitudinal angle, where for the same θ_L, different θ_T ends up making the sunray reach different positions in the length of the absorber tube. In this case, the end loss asymmetry cannot be factorized. When using θ_i, the variation on θ_T does not affect the position on the absorber tube where the sunrays reaches (HERTEL; MARTINEZ-MOLL; PUJOL-NADAL, 2015). Although the advantages of the $(\theta_T - \theta_i)$, most standards tests use the $(\theta_T - \theta_L)$ space.

All these three angles can be obtained as function of the solar azimuth and the zenith angle, as seen in equations (4.5), (4.6) and (4.7). For different orientation of the axis of the collector, the global vectors have to be rotated with respect to the plane of aperture, using the azimuth of the collector (γ_{col}).

$$\theta_T = \arctan(\sin(\gamma_s - \gamma_{col}) \tan(\theta_Z)) \tag{4.5}$$

$$\theta_L = \arctan(\cos(\gamma_s - \gamma_{col}) \tan(\theta_Z)) \tag{4.6}$$

$$\theta_i = \arcsin(\cos(\gamma_s - \gamma_{col}) \sin(\theta_Z)) \tag{4.7}$$

The transversal angle is positive in the morning and negative in the afternoon. The incident and longitudinal angles are positive when coming from the north and negative when coming from the south.

The IAM has different definitions depending on the author. It may or may not include the end losses inside the IAM_L (longitudinal IAM). When taking a wider approach, it is best not to include the end losses, then different lengths of collectors can be easily analyzed. However, when studying one specific collector, the end losses may be included, such as in the work of (HERTEL; MARTINEZ-MOLL; PUJOL-NADAL, 2015) and (HORTA; OSÓRIO, 2014). Since the present work studies two specific collectors, the end losses are included inside the longitudinal IAM curves. In addition, the IAM curve given by CNIM also

includes the end losses, therefore also including it on the curve developed facilitates the comparison. However, if not included the end losses can be later obtained by equation (4.8), where h_r represents the height from the aperture plane to the receiver, and L_{col} the length of the collector line.

$$\eta_{endL} = 1 - \tan(\theta_i) \frac{h_r}{L_{col}} \tag{4.8}$$

The longitudinal and transversal IAM were assessed by means of a ray tracing software for both workbenches analyzed.

4.1.1   Mirror positioning

Different from parabolic trough concentrators, the reflective mirrors surface on an LFC are not perpendicular to the sunray transversal direction. Each line of mirror of an LFC has a different inclination in order to correctly direct the sunrays to the receiver; however, all lines move with the same angular pace.

Most LFC have an offset from between the turning center of the mirror line and the mirrors surface. This has to be taken into account in order to calculate the mirrors inclination as function of the incidence angle. The mirrors positions are function only of the transversal component of the incidence angle.

To serve as an input on the ray tracing software, a geometrical relation was developed in order to predict the mirror inclination with respect to the transversal angle, taking into consideration the offset pivot. The angular relation can be seen in Figure 4.2.
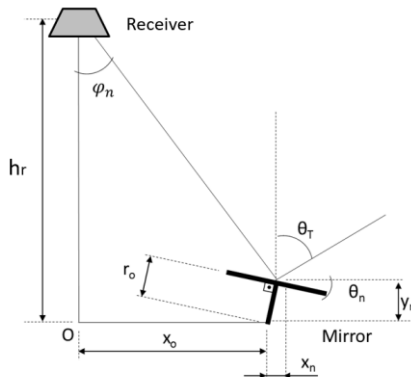
Figure 4.2 - Mirror lines angular relation.

Finding the inclination of the mirrors is an iterative procedure, that can be seen on equations (4.9) to (4.12) (WALKER, 2013). The x_0 represents the position on the horizontal plane of the turning axis of the mirror line, the r_0 is the offset pivot distance, θ_n is the inclination of the mirror plane.

The variation in the x and y axis due to the offset are seen in equations (4.9) and (4.10). They are initially found using a guess value for θ_n.

$$x_n = r_0 \cos(90 - \theta_n) \tag{4.9}$$

$$y_n = r_0 \sin(90 - \theta_n) \tag{4.10}$$

$$\varphi_n = \arctan\left(\frac{x_0 + x_n}{h_r + y_n}\right) \tag{4.11}$$

The inclination of the mirror can then be found by using equation (4.12). This angle is then used in the first equation again, repeating the procedure until it converges.

$$\theta_n = \frac{\varphi_n - \theta_T}{2} \tag{4.12}$$

This procedure is used to obtain the mirror position to all transversal angles in the case of the SunCNIM LFC. However, since the LEPTEN LFC has only one actuator to move all miror lines, the mirror lanes cannot move independently.

The movement of all mirrors would be exactly the same for a case where the center of the mirrors is equal to the center of turn, but the LEPTEN LFC has an offset pivot of 65 mm. For that, this procedure of finding the mirror position is used for a transversal angle of zero, in order to find the initial offset of the mirrors. For other transversal angles each mirror line moves accordingly to equation (4.13), and the parameters showed on table Table 4.1. These parameters were found minimizing the tracking error throughout all the transversal angle range. The parameter a represents the angular pace that all mirror lines are subjected, and b represents the initial offset.

$$\theta_n = -a\,\theta_T + b \tag{4.13}$$

Table 4.1 – Angular movement parameters for the LEPTEN LFC mirror lines.

Line	1	2	3	4	5	6	7	8	9	10
b [°]	15.89	12.87	9.50	5.84	1.97	-1.97	-5.84	-9.50	-12.87	-15.89
a [-]	0.504									

This procedure allows finding the position of the mirrors for different θ_T, and it is used as an input on the ray tracing software. Within this software, sets of values of θ_T and θ_i are changed in order to evaluate the collector at several different incidence angles, for both the longitudinal and transversal planes. For variations on the longitudinal plane the inclination of the mirrors is the same as for the zero incidence angle.

4.1.2   SolTrace Software

CSP are usually complex optical systems, with many parameters to be analyzed, such as solar tracking and geometries that varies from collector to collector. Computational methods are usually applied in order to evaluate the performance of these systems. One of these methods is the ray tracing methodology, which is described in Appendix B. The MCRT optical tool chosen was the software SolTrace.

Due to the random nature of generating a large quantity of sunrays, the SolTrace is suitable to analyze system with complex geometries, providing accurate results. However, this method is time consuming, depending on how many sunrays are to be generated, and therefore, how precise the result is to be.

In the SolTrace interface, there are the stages and the elements. The stages represent a direction of iteration of the sunrays. The sunrays interact first with the first stage, only after that, it goes to the second stage and so on. After leaving one stage, the sunray never returns, even if physically it would do so. In addition, it does not compute shading from further stages. Therefore, the best option for LFC is to model all the optical system in one stage. The elements of each stage represent the elements of the optical system, such as mirrors or receivers. Elements can be of either reflective or refractive optical nature. The optical properties can be set for each individual element (WENDELIN; DOBOS; LEWANDOWSKI, 2013).

When a sunray interacts with an element, the transmittance value is compared to a random number, determining if it is going to be absorbed or reflected. If absorbed, the next ray is generated and so forth.

The sun is defined by two parameters, its position and the angular intensity distribution of light across the sun's disk. A pillbox distribution

was used as sun shape. This distribution is adequate for a large range of problems (WENDELIN; DOBOS; LEWANDOWSKI, 2013).

To optically characterize a collector experimentally it would be needed a great quantity of experimental measurements on different incidence angle, including measurements on zero incidence angle. As mentioned, these measurements are not available on the latitude of both of the LFCs analyzed. Therefore, the use of an optical evaluation tool can be of great assistance in analyzing the collector.

4.1.3   SunCNIM LFC IAM

The IAM curves of the LFC prototype were given by SunCNIM. However, these curves were reproduced with ray tracing simulations, in order to compare results. Therefore, another set of IAM curves was obtained using SolTrace.

The geometry of the collector was thoroughly modeled in the SolTrace, including the secondary reflector curves (parabolic compound geometry), the insulation glass of the receiver and the longitudinal and transversal spacing between mirrors. Figure 4.3 shows the IAM obtained.
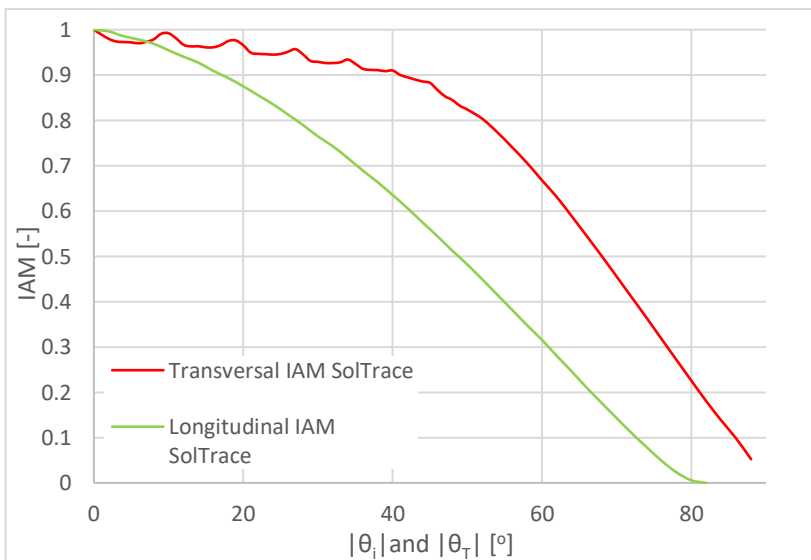
Figure 4.3 - IAM curves from the SunCNIM LFC obtained using SolTrace.

It can be seen that for LFC, the longitudinal IAM curve has a smoother line, while the transversal presents a knurled pattern on the curve beginning (Figure 4.3), caused by the shade of the receiver reaching times the primary mirror times the spacing between mirror. The Ray tracing method presented a good agreement with the curves given by SunCNIM, and they were used on further analysis of the SunCNIM LFC.

4.1.4   LEPTEN LFC IAM

The receiver from the LEPTEN workbench is different from the receiver of the SunCNIM LFC. It is a trapezoidal cavity with six absorber tubes. All the elements of the LFC were modeled inside the SolTrace. The longitudinal and transversal angles were varied one at a time in order to find the two IAM curves. The transversal curve can be seen on Figure 4.4, and it was obtained in a straightforward procedure with the variation of the transversal angle for a zero longitudinal angle.
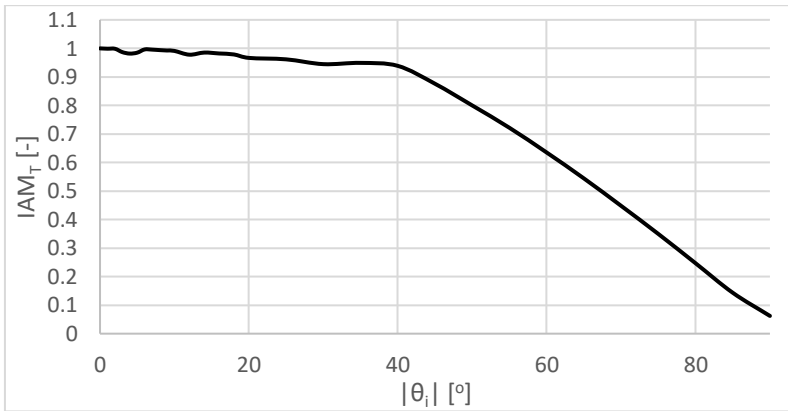
Figure 4.4 - Transversal IAM from LEPTEN LFC obtained using SolTrace.

However, the procedure to obtain the longitudinal IAM for the LEPTEN LFC is a bit more complex. As presented on section 3.2, this prototype has a moving absorber to compensate the end losses. Although it does not influence the transversal IAM, it will have a direct effect on the longitudinal IAM. So, in order to properly simulate the IAM_L on SolTrace the geometry of the receiver has to move accordingly to the variation on the incident angle, up to a point where the moving absorber reaches a maximum dislocation allowed by the system. As stated, the maximum dislocation due to north is of 1.16 m and due to south is of 3.72 m.

Figure 4.5 shows the different IAM_L for three cases, one considering a fixed receiver (zero displacement), and the others considering a moving receiver with a maximum displacement to north and south of 1.16 m and 3.72 m, respectively. The latter two curves represent the IAM_L curves for the LEPTEN prototype when moving north and south respectively.

It can be seen that the moving absorber has a great impact on the IAM_L, and this system allows for the workbench to make better use of the available solar radiation for a wider range of time periods. However, the moving receiver system is only adequate for small scale LFC, since the improve in the IAM_L curve is less appreciable on larger lines of collectors. This is because the end losses are inversely proportional to the total length of the collector, as seen on equation (4.8). This effect can be seen on Figure 4.6, where different configurations of the LFC are considered.
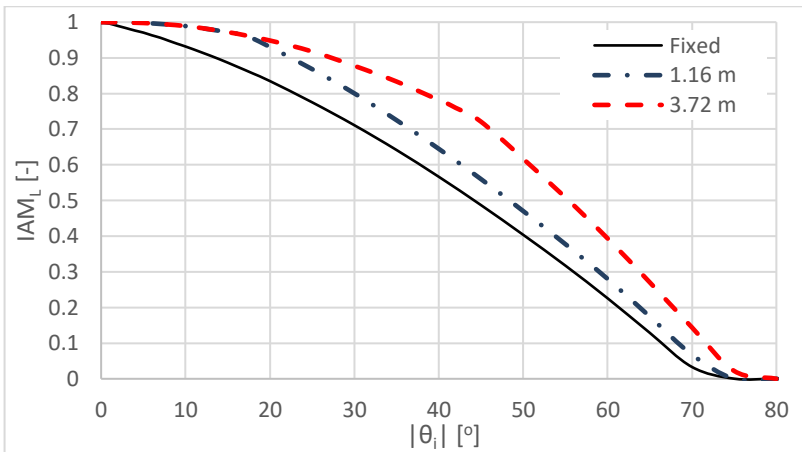
Figure 4.5 - Longitudinal IAM for a fixed receiver and a receiver with a maximum dislocation of 1.16 m to north and 3.72 m to south.

All the LFC compared in Figure 4.6 have the same transversal geometry of the LFC from LEPTEN, however they present different lengths. First, a case of an infinite LFC is analyzed, as seen on the black dashed line. This represents the maximum longitudinal IAM that this configuration of LFC can achieve, since an infinite collector does not take into account the end losses. Later, a case of the LEPTEN LFC with 120 m of length was simulated for a case considering the 3.72 m of moving absorber to south and a case of fixed receiver. This represents a case where

10 LFC modules are connected in series. And then the result of the simulations of the actual LEPTEN prototype are plotted for a case of fixed and moving absorber with 3.72m of maximum displacement to south.

The comparison shows that the moving absorber allows the LFC to operate with the same IAM_L as an infinite collector for incident angles up to 43°. This represents a great increase on performance when compared to a fixed receiver of 12 m of length.

After 43° of incident angle, the maximum length of the moving absorber is reached, and the 12 m of length of the LEPTEN LFC starts to weight heavy on the end losses, as it can be seen on the green curve. For the 120 m LFC, the total length diminishes the end losses effect and even after the final displacement of the moving receiver is reached, the IAM_L curve is still similar to an infinite LFC case. In fact, the IAM_L curve for the 120 m LFC with fixed absorber is also close to the infinite IAM_L. It is noteworthy that 120 m of collector line is not an unreal length, in fact, most linear concentrator solar plant have longer lines, which would reduce even more the effect of the moving absorber.

This shows both that the moving absorber is a powerful design advantage for small-scale prototypes, and that it is not viable for large scale LFC, since it requires a more complex system and it does not make a great impact on the overall efficiency.
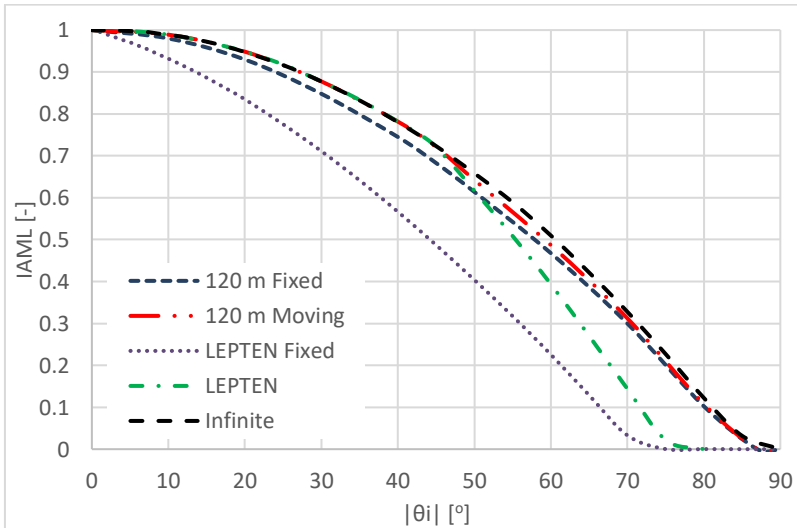
Figure 4.6 - Comparison of the IAML for different configurations of the LFC from LEPTEN obtained using SolTrace.

Solar linear concentrators usually present symmetry in both transversally and longitudinally. This means that the IAM curves are usually presented as showed in Figure 4.4 and Figure 4.5, and that these curves are symmetrical for positive and negative values of θ_i and θ_T. However, for the LEPTEN prototype it is important to know not only the magnitude of these angles, but the direction where they come from.

The IAM$_T$ is symmetrical however the direction from where the θ_T originate influences on the concentrated radiation profile on the absorber tubes, as it will be seen in details on section 4.2. And due to the design of the LFC the moving absorber has different maximum displacements regarding the direction of the θ_i. The final IAM curves covering all range of the incident and transversal angles are showed on Figure 4.7.
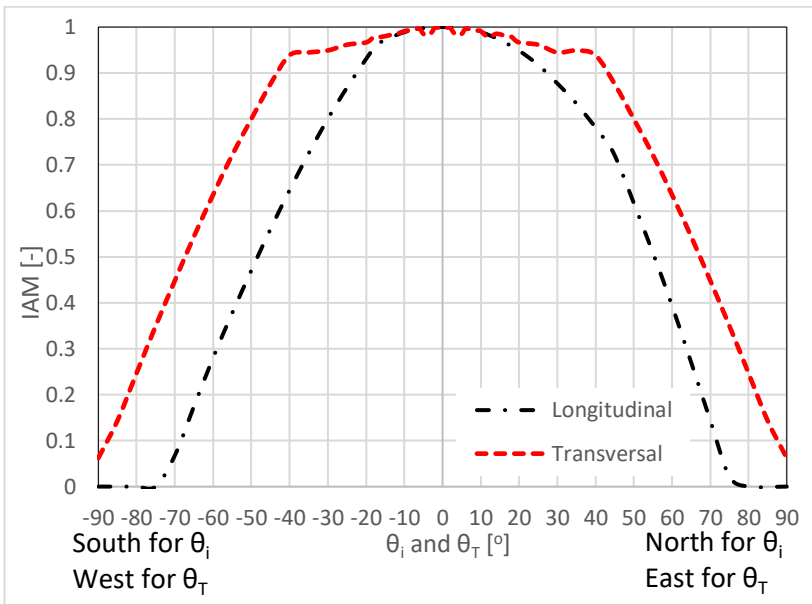
Figure 4.7 - Final IAM curves obtained by SolTrace for the LEPTEN LFC.

As it can be seen, the θ_i is positive when directed to north and negative to south, and the θ_T is positive due to east and negative due to west.

These IAM curves are used on further calculation, although the longitudinal IAM suffer some adaptations when analyzed with experimental data. This will be discussed in section 4.3.1.2.

4.2 Non-uniform concentrated radiation model for the LEPTEN LFC

Most linear concentrators are designed with only one absorber tube, evacuated or not. In that case, the one-dimensional model usually considers a homogeneous heat on the surface of the tube. The prototype from LEPTEN however has six absorber tubes. One way to model the heat flux reaching the tubes is to equally divide the incoming heat among the six tubes. The thermal model used in this work considers this config-uration, but it also makes a different approach, that takes into account the concentrated radiation distribution between tubes.

For that, it is important to analyze the concentrated radiation on the absorber tubes during real operation. Figure 4.8 shows the receiver during operation, at a time in the morning (θ_T around 45°). In this qualitative approach it can be seen that there is a higher incidence of concentrated radiation on the middle tubes, 3 and 4, with a slight tendency to the east side. Although some brightness can be seen on the aluminum walls of the trapezoidal cavity, it is noteworthy that the aluminum has a much higher reflectivity, since the tubes are painted in black selective coat. Overall, most of the concentrated radiation is indeed reaching the absorber tubes.
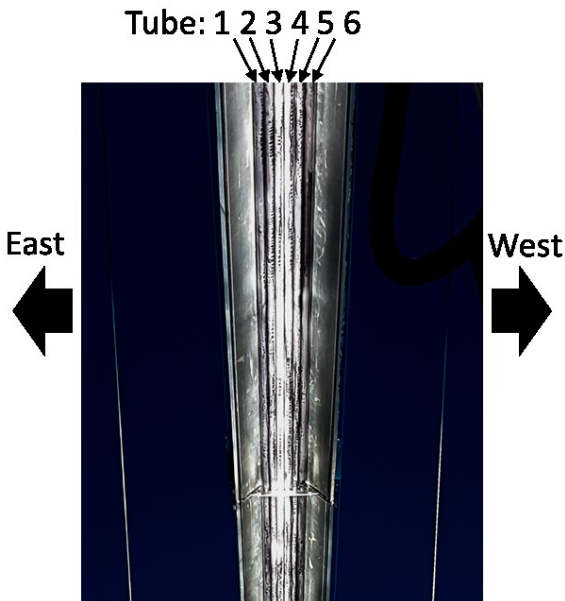
Figure 4.8 - Concentrated radiation reaching the absorber tubes

Ideally, the radiation should only be reaching the most central tubes, however due to errors in both the construction of the curved mirror, and on the specularity of the mirror itself, since common mirrors were used, there is a greater dispersion on the concentrated radiation. This effect was reproduced on SolTrace by altering values of specularity and slope errors. The actual values of these errors were not measured for the actual LFC. Hence, to calibrate this model, an interval close to solar noon of one controlled experimental test was used, and the percentage of heat gain in each tube was considered equal to the percentage of concentrated radiation reaching its respective tube.

Figure 4.9 shows the concentrated radiation simulated on SolTrace for the above condition described. The area presented in the figure is the aperture area of the absorber tubes on the receiver.
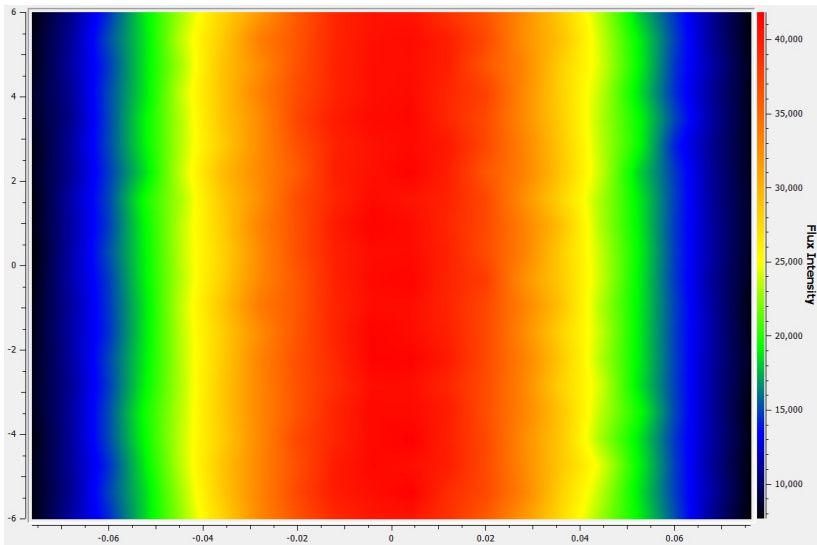
Figure 4.9 - Concentrated radiation reaching the absorber tubes simulated on SolTrace for solar noon.

Figure 4.9, however, only represents the concentrated radiation distribution for the solar noon condition. And further analysis showed that this pattern of concentrated radiation changes throughout the day. For that, the concentration pattern was analyzed regarding the variation of both the transversal and incident angles (θ_T and θ_i). The changes due to the incident angle (longitudinal direction) affects the total reduction on

the heat gain on the solar concentrator, effect that is already included on the longitudinal incidence angle modifier. This direction, however, have little impact on the percentage of concentrated radiation that each tube is receiving.

The transversal angle has a much greater impact on this concentrated radiation distribution. As seen on Figure 4.10, extracted from a simulation on SolTrace, the tubes that tend to receive more concentrated radiation are those turned to the side that the sunrays are incoming. This matches the experimental visualization of Figure 4.8 where for a morning hour (sun on the east) the three east tubes receive the large portion of concentrated radiation.
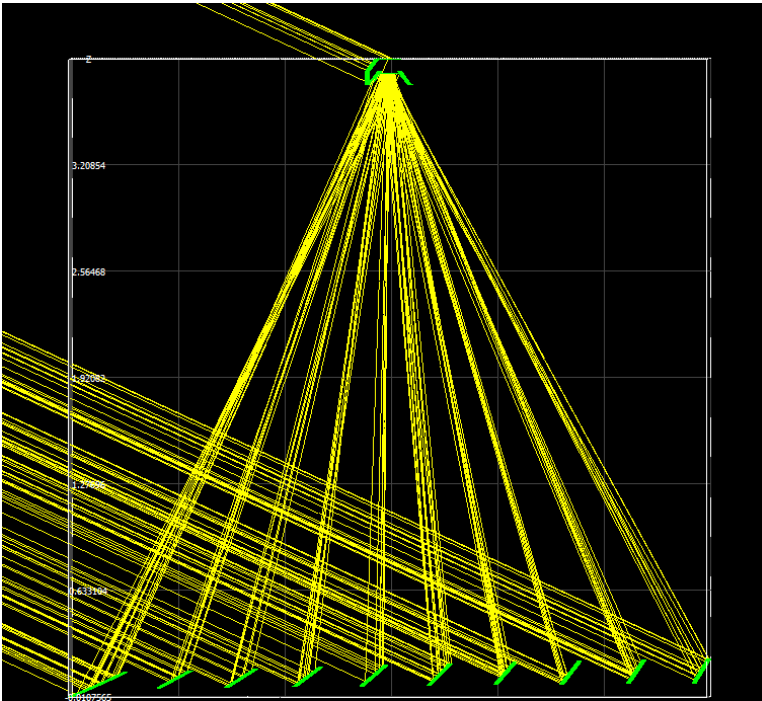
Figure 4.10 – Graphical visualization of the simulation performed on SolTrace.

Figure 4.10 shows the simulated distribution for a case with transversal angle of 65º. The shading of the mirrors mostly causes this change in distribution. SolTrace only shows the portion of the element that receives the sunrays. This can be verified by Figure 4.10, which only shows

the left side of the top of the receiver. This because the DNI is coming from the right side at an inclination of 65°. It can also be seen that the mirrors on the far right of the picture appear to have smaller dimensions due to the shading from the previous mirrors. This causes the effect seen on Figure 4.11. For this inclination, and for the geometry of the mirrors, the right side of the mirror concentrates more on the left side of the absorber, and vice versa. As the left side of most mirrors is shaded, the right side of the receiver receives less radiation.

Initial tests on the tracking system included only one line of mirror tracking the sun, with other lines shifted to prevent shading. On those tests, it was possible to see a much stable concentrated radiation patter throughout the day, reinforcing that shading is the cause of this phenomena.
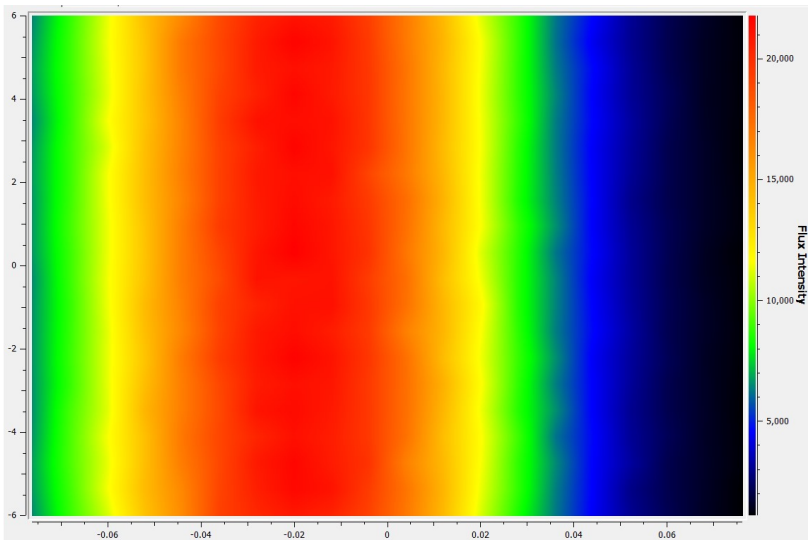
Figure 4.11 - Concentrated radiation reaching the absorber tubes simulated on SolTrace for $\theta_T = 65^o$.

Figure 4.12 presents the percentage of concentrated radiation that each tube receives with the variation of the transversal angle. The transversal angle is positive before solar noon and negative after. As seen in Figure 4.8, the tubes more on the east receives more radiation on the morning, which is verified at the graph when comparing the tube number for positive transversal angle.
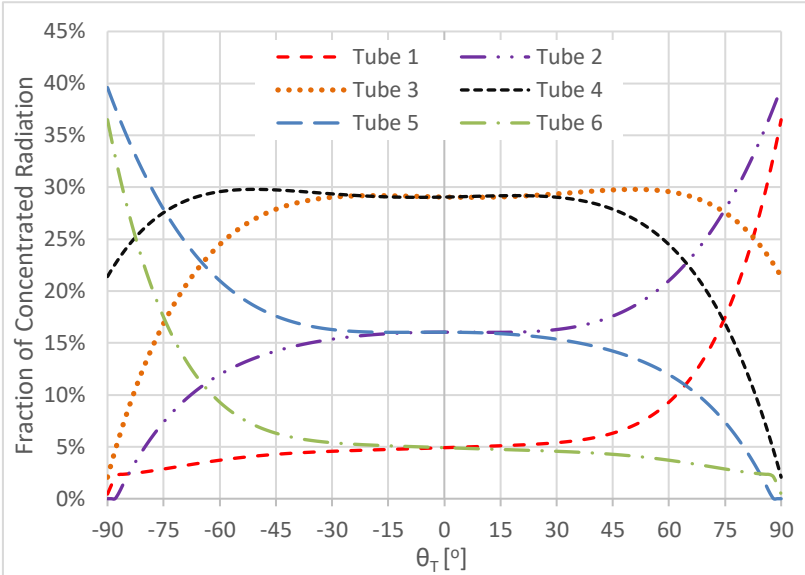
Figure 4.12 - Fraction of concentrated radiation for each absorber tube with the variation of the transversal angle.

This model of concentrated radiation distribution is included on further thermal analysis. The single-phase flow analysis on section 5.2.1 shows the comparison between this and the equal radiation distribution between tubes.

4.3   LFC parameters investigation

4.3.1   LEPTEN LFC

This section describes the procedure used to identify the main parameters of the LEPTEN workbench. They are related to the optical peak efficiency and to the heat loss curve of the receiver. These parameters can be seen on equation (4.1), and an overall scheme of the analysis performed over this equation is showed in Figure 4.13.

$$\dot{Q}_{abs} = A_m \; DNI \; \eta_{0^o} \; IAM_L \; IAM_T - \dot{Q}_{HL}$$
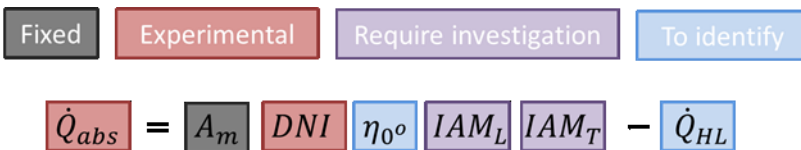
Figure 4.13 - Overall scheme of the analysis performed to identify parameters.

The heat absorbed is obtained by a simple energy balance over the HTF, as seen in equation (4.14), where the subscript o and i represents the outlet and inlet, respectively. This happens because the tests performed to identify this parameter were single-phase, which working fluid was water. All the parameters used in this equation are either a property of the fluid as the mean specific heat ($\bar{c}_p$), or obtained by experimental measurements, just like the DNI.

$$\dot{Q}_{abs} = \dot{m}\ \bar{c}_p \left(T_{HTF,o} - T_{HTF,i}\right) \hspace{2cm} (4.14)$$

The optical efficiency at zero incidence and the heat loss curve are the main parameters to be identified in this analysis. However, during the process of analyzing the experimental data, it appeared the necessity to review the incidence angle modifier curves obtained by SolTrace.

The procedures to find each of these three parameters are described on its respectively subsections, however, it is noteworthy that there is one equation (equation (4.1)) and three parameters to identify (η_{0^o}, IAM and $\dot{Q}_{HL}$). To do so an iterative solution was adopted. The logical scheme was divided in three procedures as showed on Figure 4.14.

The first procedure is dedicated to find the optical efficiency at zero incidence angle, and it does so by minimizing the errors between the right and left sides of the equation (4.1). On the first iteration, the longitudinal IAM curve used was the one obtained by SolTrace, and the heat losses were neglected. After reaching convergence, the η_{0^o} is then fixed at the value obtained, and the IAM is then analyzed. The details of why this procedure was introduced on the overall logic are discussed on section 4.3.1.2. The first procedure is then fed with the new IAM curve, in order to find new η_{0^o} values, and this is repeated until a convergence is reached.

After that, both the IAM curve and η_{0^o} are fixed and used on the third procedure, where a heat loss curve is obtained for a different set of experimental tests. The heat loss curve is used on the first procedure, repeating all cycles until a convergence is reached. In that case, all parameters are identified and can be used on further analysis.
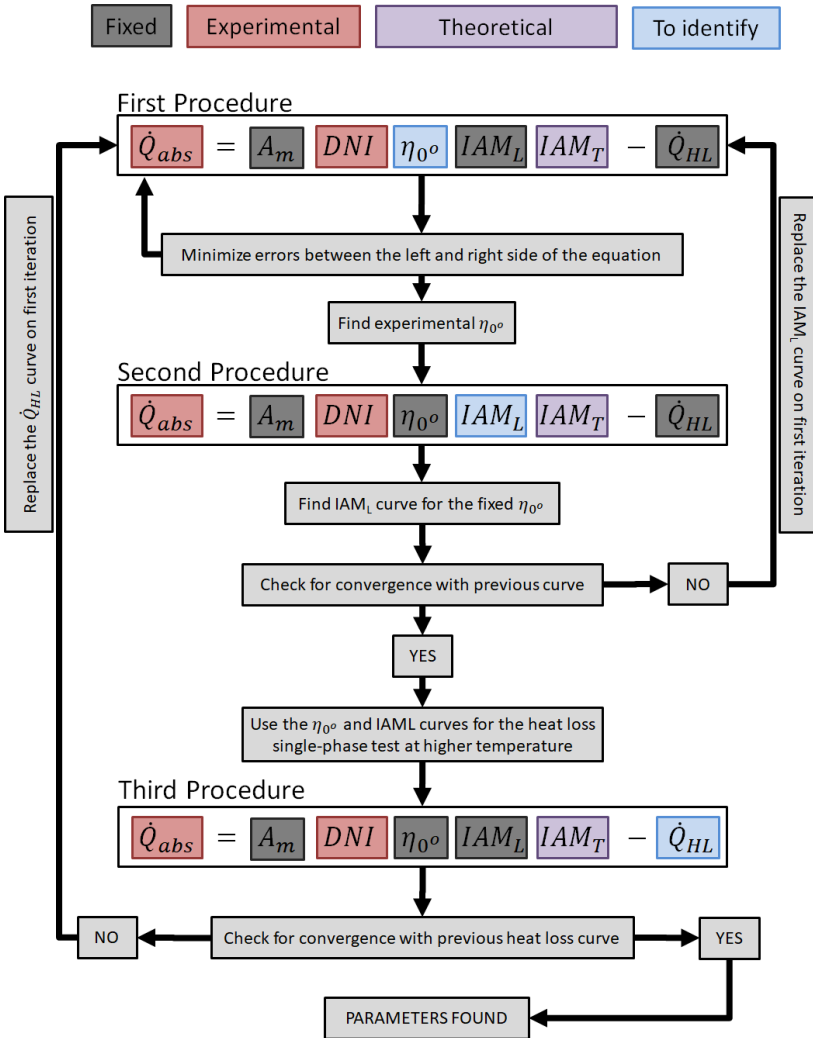
Figure 4.14 - Logical scheme to obtain the LEPTEN LFC parameters.

4.3.1.1 Optical peak efficiency

The optical peak efficiency represents in most cases the best condition that a concentrator can reach. It is an important parameter to define the prototype. The ideal to experimentally define this parameter would be to have a platform in which the collector could rotate and incline in order

for its aperture to be perpendicular to the sunray vector. However, LEP-TEN do not have such equipment, and due to the latitude of Florianopolis, there are no conditions in which the sunrays are completely perpendicular to the aperture of LFC.

In that case, to obtain the η_{0^o}, a large number of tests were performed on different days. The experimental measurements were traced back to the η_{0^o} condition using the IAM curve in equation (4.1). These tests were conducted for the lowest possible temperature, in order to minimize the thermal losses. The ideal would be to use fresh water at the inlet of the absorber and discard it at the outlet, so the mean HTF temperature would be almost equal to the ambient temperature, and the heat losses could be neglected. However, this would implicate in a large wastage of water. Then, for these tests, the HTF is fully routed to the two condensers, in order to maintain a low temperature. The electrical preheater is used just to guarantee a smother inlet temperature, increasing just a few decimates of degree in order to compensate oscillations. Steady flow condition sets of data were extracted from each experimental day and analyzed in order to find the η_{0^o}.

The η_{0^o} takes into account the optical properties of the components of the LFC, such as reflectivity of the mirror, transmissivity of the glass window, and so forth. Since it is property of the LFC it should not be subjected to external factors, and the dirt on the mirrors should be considered separately. However, there were no measurement of such parameter at the beginning of tests, therefore the η_{0^o} was obtained also including the aspect of dirt on mirrors. In addition, the workbench is installed in an urban area with lots of dust, and the cleanness of the mirrors changed visually in a matter of a couple of days. For that, the procedure to obtain the η_{0^o} was performed separately for each experimental day. The η_{0^o} variation with the date of experiment, for several experimental days can be seen on Figure 4.15. Cleaning the mirrors is a time-consuming task and were performed that only on a few occasions that are indicated on Figure 4.15. It is possible to see an increase on the η_{0^o} on tests performed after the mirrors were cleaned. The standard deviation for the η_{0^o} parameter was analyzed for each day of experiments, and the maximum value found was of 1.5 %.
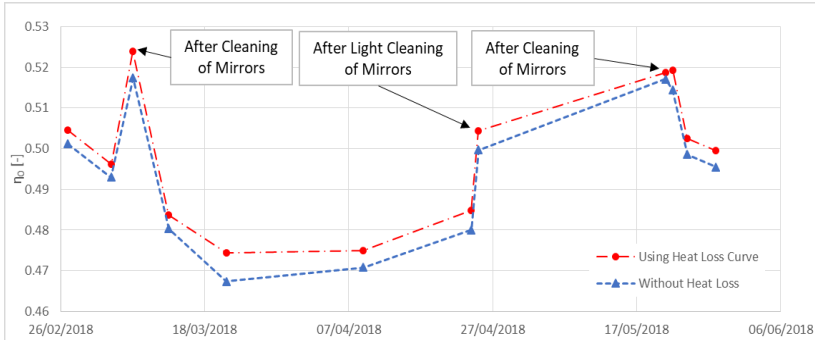
Figure 4.15 – Variation of η_{0^o} throughout the experimental days and influence of the heat losses.

Despite the low HTF inlet temperature used on the tests, the heat loss effect was still present. As described before, the first iteration of the η_{0^o} procedure on Figure 4.14 neglected the heat losses, however they were considered on further iterations until convergence. Figure 4.15 shows the η_{0^o} curves for the first iteration, without heat losses, and for the last iteration, with the heat loss curve obtained after convergence.

The values of some characteristic days from Figure 4.15 are showed on Table 4.2, for the first and last iteration, and with a brief description of the circumstances of the day. It is noteworthy that after the cleaning of the mirrors on 25/04/2018 there was a sequence of rainy days, which prevented further testing. Therefore, there was no testing between the two mirror cleaning, however it is expected that the η_{0^o} would have a drop on the following days, such as it has had after the two other mirror cleanings.

Table 4.2 – values of η_{0^o} for some characteristic days.

Day	Initial η_{0^o} [%]	Final η_{0^o} [%]	Circumstances
08/03/2018	51.7	52.4	After Cleaning of Mirrors
21/03/2018	46.7	47.5	Lowest η_{0^o} found
25/04/2018	50.0	50.4	After Light Cleaning of Mirrors
21/05/2018	51.7	51.9	After Cleaning of Mirrors

A few preliminary experiments were performed to test the response of the workbench and all equipment. They included tests without the glass window installed in the receiver. They were also analyzed, and the η_{0^o} compared with the ones obtained with glass window.

The heat loss curve for a case without glass was not experimentally obtained, since there were not enough tests for this condition. The heat

loss considered on the no glass window analysis was the one obtained with some tests without DNI, also performed to test the response of the workbench and the electrical preheater. They ultimately underestimate the heat losses under real condition tests.

In addition, the tests were performed without a cleaning of the mirrors, so the overall η_{0^o} found for the case without glass window is underestimated regarding what would be found using clean mirrors and a proper heat loss curve. Even then, the η_{0^o} found was higher than the ones found for the case with glass window, as can be seen on Table 4.3.

Table 4.3 - Influence of the glass window on the η_{0^o}.

Overall η_{0^o} for no glass window case [%]	Maximum η_{0^o} for final LFC [%]
56.6	52.4

This shows that, as expected, the glass window has a negative effect on the optical performance. The goal of the glass window is to reduce heat losses, which by accounting equation (4.1) would increase the heat absorbed by the HTF, however, it still decreases the η_{0^o}.

4.3.1.2   IAM

Initially, the idea was to go from procedure 1 directly to procedure 3 from the Figure 4.14. The η_{0^o} found would be used to find the heat losses, and both procedures would converge to the final parameters. For that, the incidence angle modifier curves used were obtained by the software SolTrace. However, using the longitudinal IAM curve from SolTrace to find the η_{0^o} was giving some inconsistent results for incident angles above 30°. The η_{0^o} obtained was below expectations.

This effect was most evident at the experimental results from the 21/05/2018, after a mirror cleanup. The η_{0^o} found using the SolTrace curve was 48.8 %, lower than the expected for the LFC prototype with clean mirror.

After analyzing the data from this day, it was possible to see a direct relation between the incident angle θ_i and the η_{0^o}. The concept of the incident angle modifier is exactly to disassociate the optical performance of the collector at peak solar radiation, with the variation of the overall performance due to inclinations of the solar vector. In order to better investigate this effect, a longer test was performed on the 28/05/2018, including a large range of θ_i. The relation between the incident angle and optical peak efficiency can be seen on Figure 4.16.
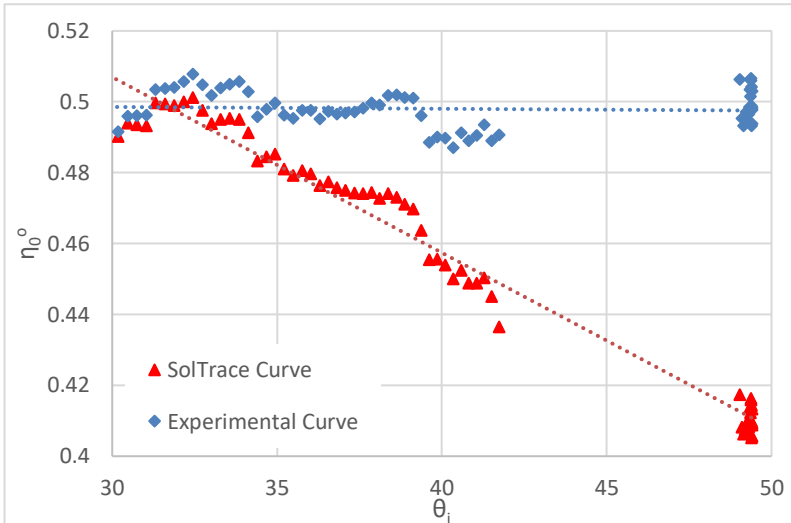
Figure 4.16 - Relation between the incident angle and optical peak efficiency.

A correct IAM curve would give an apparently random distribution of η_{0^o} with the variation of θ_i, and that was indeed verified for tests performed during the summer, where θ_i did not reached values less than 30º.

The goal of this procedure, the second on the diagram of Figure 4.14, is to find a curve that best fits the experimental data, eliminating the dependency of θ_i on the η_{0^o}. The same experimental data used on the first procedure was used in this analysis. The η_{0^o} obtained on the first procedure is said to be constant during all the test interval for each day, and the longitudinal IAM was then set as variable and found. Figure 4.17 shows the dispersion of IAM_L with θ_i found for the several steady state intervals, for different experimental days. The standard deviation between experimental dispersion and the IAM_L was of 7.5 %. A tendency curve was traced in a way to best fit the IAM_L dispersion, and the resultant curve was used on the first procedure to find new η_{0^o} values, and this was repeated until convergence. Figure 4.17 shows the final dispersion of the IAM_L for the experimental days analyzed, and Figure 4.16 shows the final relation between η_{0^o} and θ_i using this converged experimental IAM_L curve. The standard deviation for the η_{0^o} seen on Figure 4.16 for the SolTrace curve was of 3.5 % while for the converged experimental curve it was 0.4 %.
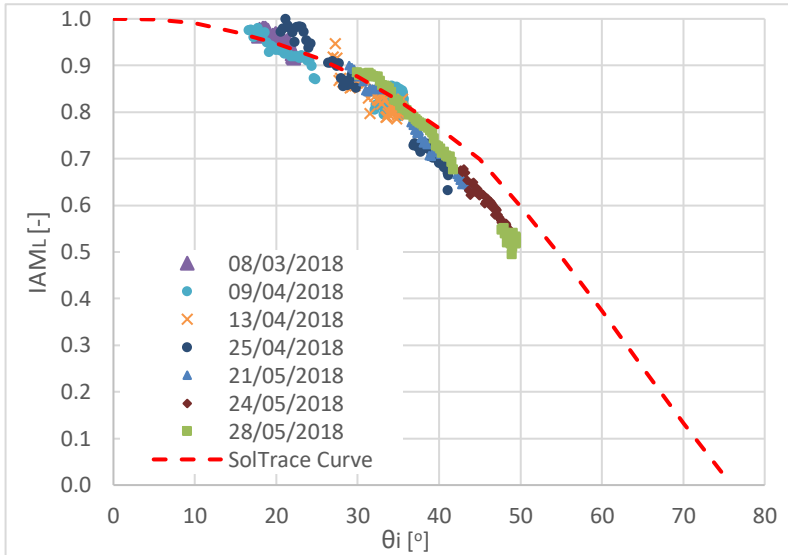
Figure 4.17 - Dispersion of IAM_L by θ_i for several steady state conditions.

It is noteworthy that the shape of the curve was adjusted to follow a path similar to the one of the IAM_L found by SolTrace. This was performed to better extrapolate the experimental curve to regions of θ_i where no experimental data reached. As seen in Figure 4.17, from the day that the workbench was fully functional until the end of the experiments used at this thesis, a range of θ_i from around 15° to 50° was covered.

When tracing the tendency line for the experimental data dispersion similar to the one showed in Figure 4.17, in some iterations the curve would make an inflexion above the unitary value ($IAM_L = 1$) for θ_i below 20°. This is not physically coherent, and in those cases, the IAM_L from SolTrace was used as an upper limit to the experimental curves obtained. Another fact that collaborate with this is that the IAM_L from SolTrace had a satisfactory performance for experiments done in the summer, with θ_i below 30°. The IAM_L curves from SolTrace and obtained experimentally can be seen on Figure 4.18.
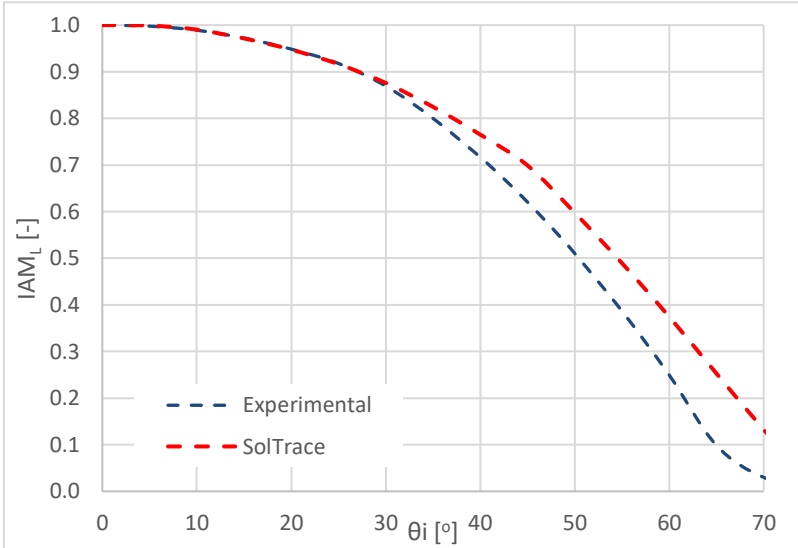
Figure 4.18 – Comparison between the experimental and the SolTrace IAM_L curves.

The difference between curves starts above 30° of incident angle. Several factors may explain this difference. Perhaps the most important is the glass window. Although it is an extra clear glass, it is a commercially found glass, not specifically designed for solar applications. This glass is visually very clear when looked perpendicularly, but when looked with a certain inclination, it is also visible the increase in reflection that it has. Other factors may lead to this decrease of performance with θ_i such as the shading of objects not considered on the SolTrace simulation, which starts influencing when the receiver moves a certain amount, such as part of the pipes and the steam separator. The experimental IAM_L was used on further analysis.

The discrepancy between the theoretical and experimental IAM_L curve raised the question about the performance of the IAM_T curve. However, upon analysis it was possible to see that the experimental data fitted very well with the theoretical curve obtained by SolTrace, as showed on Figure 4.19, with a standard deviation of 2.1 %. Therefore, as presented on the diagram on Figure 4.14, the IAM_T curve used in all analysis was the one obtained theoretically with SolTrace.
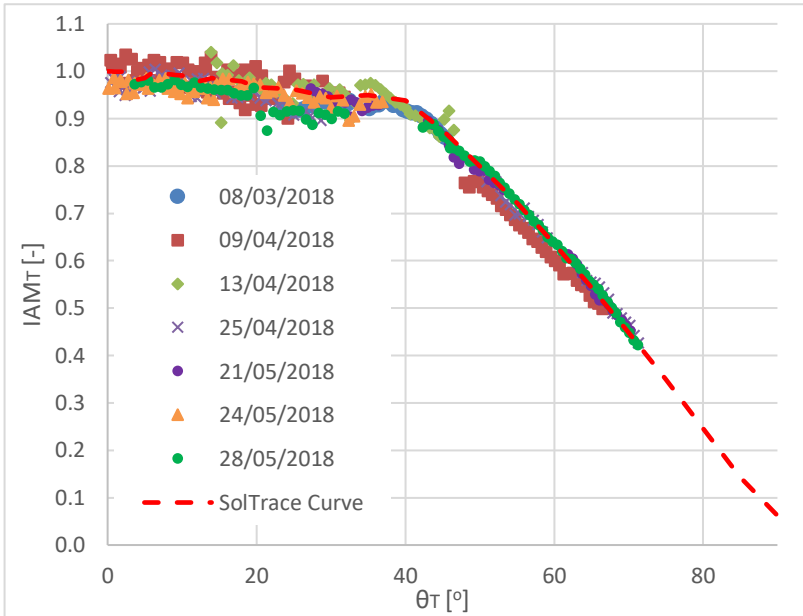
Figure 4.19 – Comparison between the dispersion of experimental IAM$_T$ by θ_T with the SolTrace curve.

4.3.1.3 Heat losses

The last procedure is dedicated to find the heat loss curve of the receiver. For that, a different set of experimental data was used. As stated before, tests at temperature closest to the ambient temperature were used to obtain the η_{0^o}, because they reduce the effects of the heat losses on the analysis. The same tests were used to find the IAM$_L$ experimental curve. However, to evaluate the heat loss curve of the receiver, it is interesting to have a large range of operating temperatures. For that, tests at several temperature levels were performed.

In all tests the HTF was single-phase subcooled liquid, in order to be able to obtain experimentally the heat gain by the HTF from equation (4.14). A two-phase mixture at the outlet would implicate in measuring the quality of the mixture in order to get its enthalpy, which is a task that could not be performed with the equipment available.

Since this analysis uses a different set of tests, some of the test days do not have a η_{0^o} analysis performed previously to the test. For those, the η_{0^o} adopted was one closest to the previous day with an η_{0^o} calculation.

Heat had to be rejected after the outlet of the receiver to maintain a steady state condition at the inlet of the receiver operating with concentrated radiation. To do so, for tests up to 100 ºC the condensers were used. The different temperature levels required different by-pass configurations on the outlet of the steam-separator, which dictates how much of the flow goes to the condensers and how much goes directly to the receiver.

For tests above 100 ºC the valves to the condensers were closed, since these devices were not designed to operate at higher pressures, and the piping leading to them have an operational temperature limit of 100ºC. The temperature of the test was controlled using the control valve, set to the saturation pressure of the desired inlet temperature at the receiver. The rejection of heat to the environment by the control valve ensures the heat rejection that the system needed to maintain a stable condition at the inlet of the receiver. A ball valve was partially closed at the outlet of the receiver, in order to promote a bottleneck effect and pressure drop, to guarantee a subcooled condition of the flow exiting the receiver.

The results of all tests were assembled by temperature difference between the HTF and the ambient, and these mean results of the experimental mean values can be seen on Figure 4.20.
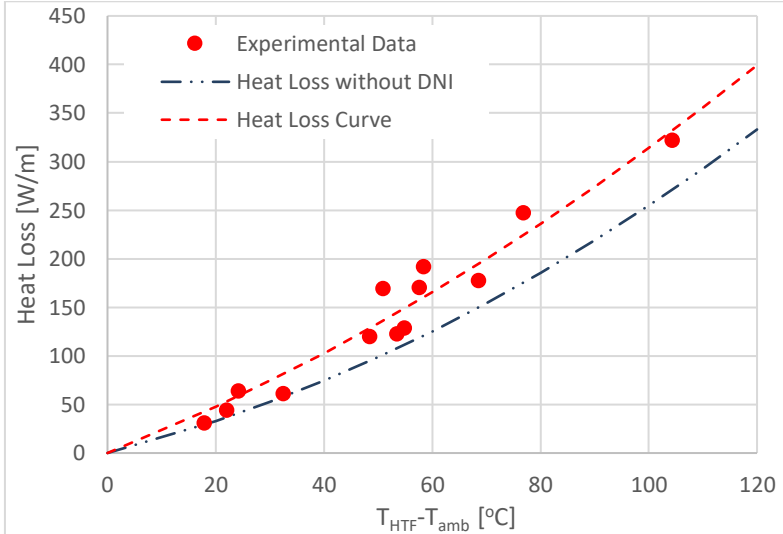
Figure 4.20 - Experimental heat loss curves with and without concentrated radiation.

The heat loss curve and its parameters can be found on equation (4.15) and Table 4.4.

$$\frac{\dot{Q}_{HL}}{L_T} = a \ (T_{HTF} - T_{amb})^2 + b \ (T_{HTF} - T_{amb}) \tag{4.15}$$

Table 4.4 – Heat loss curve parameters.

a	9.44E-03	$W \ m^{-1} \ K^{-2}$
b	2.19	$W \ m^{-1} \ K^{-1}$

Early tests on the workbench were made without concentrating radiation, in order to previously estimate the heat loss. For that, the HTF was heated using the electrical preheater, the drop in the temperature was measured and the heat loss evaluated. The curve resulting from these experiments can also be seen on Figure 4.20.

As reported by (DUDLEY et al., 1994), the heat loss for a linear solar concentrator operating with concentrating radiation is expected to be higher than the heat loss obtained by an experiment without concentrated DNI, for tests where the absorber receives heated HTF at the inlet. This is due to the temperature on the outer surface of the absorber tubes. For the latter case, the temperature is higher on the inside of the tube, since the heat is flowing from the HTF to the environment. On the case with concentrated DNI, the temperature is higher on the outer surface of the absorber tubes, and the heat flows both to the fluid and to the environment. For that, since it has higher temperatures on the outer surface, the heat losses due to convection and radiation are higher for the same HTF temperature.

4.3.2   SunCNIM LFC

For the SunCNIM LFC, due to the few experimental data available, only the η_{0^o} was obtained, using a much simplified version of the procedure presented. SunCNIM provided the heat loss curve used and the IAM curves were obtained using SolTrace. The parameter identification logic considers only the first procedure presented on Figure 4.14, as seen on Figure 4.21.

The model is similar to the one presented for the LEPTEN LFC. It uses the measured meteorological data, sun position information and the input data such as inlet pressure and HTF temperature. In this stage, the zero optical efficiency is estimated.
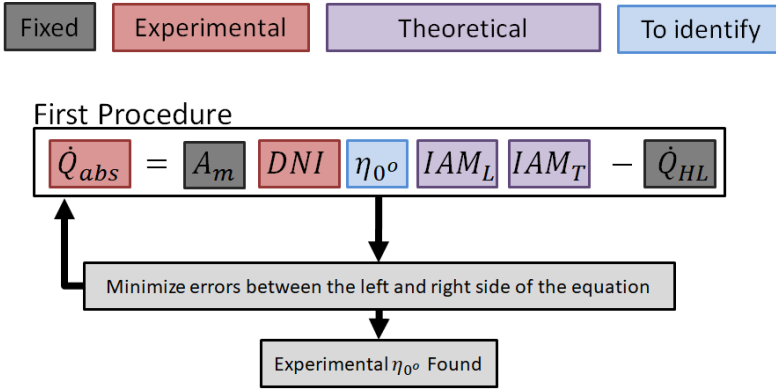
Figure 4.21 - Parameter identification procedure for SunCNIM.

At the end, the calculated and measured heat gains are compared for the entire data interval, and the zero incidence optical efficiency is interactively obtained in order to reduce the difference between them. When the root mean square of the difference between the calculated and the measured heat gain is its lowest, it means that the data is coinciding best and that the zero incidence optical efficiency is obtained.

One difference is how the experimental heat is calculated. Since the experimental data provided by SunCNIM is for the LFC at regular operation, and not for a low temperature operation tests as used on the LEPTEN tests, there is a generation of steam on the receiver. For that, instead of using equation (4.14), equation (4.16) will be used. It takes into account the heat used to saturate the water and the heat to boil the portion of steam measured at the outlet.

$$\dot{Q}_{abs} = \dot{m}\,\bar{c}_p\left(T_{HTF,Sat} - T_{HTF,i}\right) + \dot{m}_V\,\Delta h_{evap} \tag{4.16}$$

Where $\dot{m}_V$ is the outlet vapor mass flow rate that is routed to the environment and $T_{HTF,Sat}$ and Δh_{evap} are the saturation temperature and the evaporation enthalpy of water, respectively, for the saturation pressure measured in the outlet of the receiver.

SunCNIM performed a study on the uncertainties of the measured heat gain based on the uncertainty of the measurement equipment present at the power plant. The overall uncertainty of the measured absorbed energy by the receiver is about $\pm 4.1\%$ at a confidence level of 95% (2σ).

The simulation result for the thermal outlet power calculated using the η_{0^o} obtained can be seen for some intervals analyzed in Figure 4.22 and Figure 4.23. The results are normalized to the mean value of the interval to maintain company confidentiality. The figures show the measured thermal outlet power, and the one obtained by the present model and by calculations performed by SunCNIM.
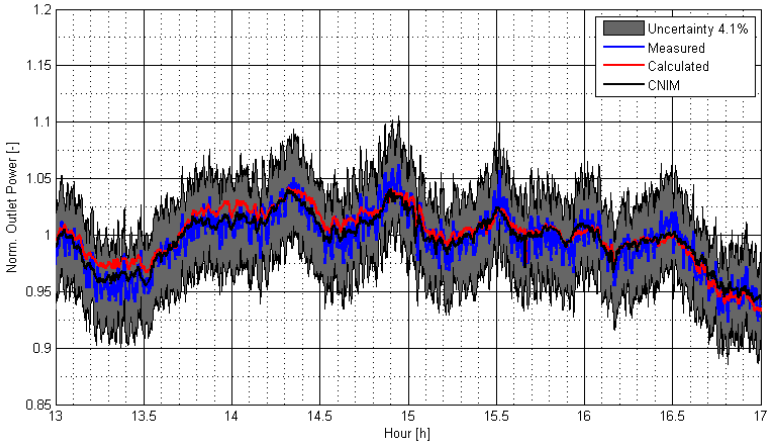
Figure 4.22 - Normalized outlet power analysis for 21 of July of 2015.
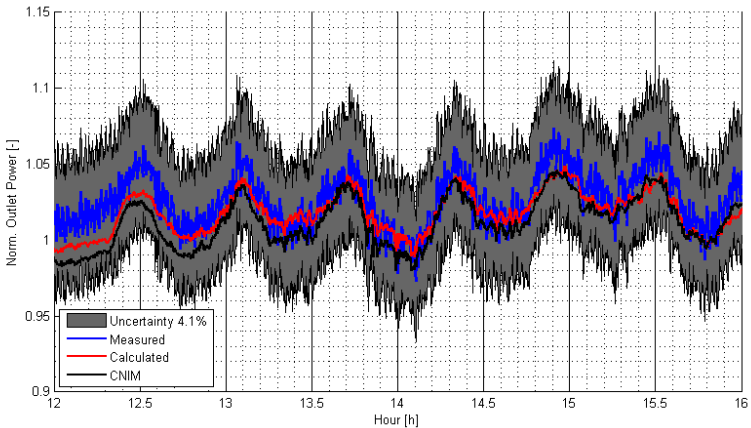
Figure 4.23 - Normalized outlet power analysis for 24 of July of 2015.

As seen, the calculated outlet power from both SunCNIM and the presented model stayed well inside the uncertainties of the data for the

days exposed. All five days of experimental data were analyzed, and the root mean square error (RMSE) is obtained for each day by equation (4.17). The value of the optical efficiency at zero incidence angle is omitted due to the confidentiality agreement.

$$RMSE = \sqrt{\sum_{i=1}^{n} \left(\frac{Y_{mod,i} - Y_{exp,i}}{Y_{exp,i}} \right)^2 / n} \qquad (4.17)$$

Table 4.5 shows the RMSE error by the model used with the one obtained by SunCNIM in previous analysis. It was seen that the last two days presented the higher errors, with one day having errors higher than the uncertainty of the measurements. To search for a reason why these two days had such different results, other experimental measurements were analyzed. Table 4.6 shows the mean wind load for the windows of analyzed data for the experimental days used.

Table 4.5 - RMSE for all five experimental days.

Day	RMSE (Model)	RMSE (Sun CNIM)
21/07/2015	0.9%	1.4%
23/07/2015	1.7%	1.8%
24/07/2015	2.4%	3.6%
19/09/2015	8.0%	2.8%
21/09/2015	3.9%	2.0%

In order to apply the QDT the data chosen must be selected using some criteria. It was seen that the data from the two last days of measurement oscillated during many periods of time. It makes the QDT not reliable for these cases, and the transients would have to be included on the analysis.

In addition, wind loads may be the cause of the oscillation, especially on the 19/09, as can be seen on Table 4.6. This would implicate on a defocusing of some mirrors, which would reduce the concentrated radiation on the receiver and would not allow reproducing an adequate optical efficiency on the simulations. The 21/09 also presented higher gusts than the three first days, however not enough to justify the large operational conditions oscillations. The 21/09 had a constant income of DNI, however in some periods many operational parameters varied, including the pressures. This could indicate a malfunction on the pump on this specific day,

which would make the results nor reliable for this analysis. Considering this analysis, these last two days were removed from the study in order to set a more adequate and reliable η_0, as seen in Table 4.7. This because in order to have a proper optical characterization, the influence of external parameters on the optical efficiency should be minimized. And it was seen that for the last two days, the wind and other parameters cause an oscillation on measurements.

Table 4.6 - Wind gusts for the selected data of the five experimental days.

Day	Mean wind speed [km/h]
21/07/2015	7.5
23/07/2015	10.0
24/07/2015	9.5
19/09/2015	24.4
21/09/2015	13.1

In a strict analysis, all the parameters should be well controlled and maintained for the interval of study (SALLABERRY et al., 2015). However due to the limited experimental data, the analysis was carried out the more stable possible even though some oscillations were found.

Table 4.7 - RMSE for selected experimental days.

Day	RMSE (Model)	RMSE (CNIM)
21/07/2015	1.1%	1.4%
23/07/2015	1.7%	1.8%
24/07/2015	1.8%	3.6%

The analysis of the three first experimental days presented much reliable results, with errors inside the uncertainties of the measurements.

Some steps seen in the work of (DUDLEY et al., 1994) could help to improve the optical analysis, and even start the thermal investigations. One of them is to evaluate the optical efficiency of the plant with zero incident angle (or the closest possible), while it operates with low temperature of the HTF, as it was performed at the LEPTEN LFC. This would reduce the thermal losses, enabling to verify only the optical efficiency of the collector. The same low temperature procedure could be used to analyze other incidence angle points, in order to verify the calculated IAM curve validity. With these parameters well established, the plant could be

studied operating in nominal conditions, in order to evaluate the thermal losses.

4.4   Partial Conclusions

The characterization procedure of an LFC is used to obtain some main key aspects of the concentrator, such as the IAM curves, the peak efficiency and the heat losses experimental curve.

For both cases the IAM curves were obtained using the SolTrace MCRT tool, however, some inconsistences were found for the LEPTEN LFC when analyzing the experimental results. For that, further experiments were performed with the intent to verify the calculated IAM comparing with an experimental one. As a result of this analysis, the longitudinal IAM for the LEPTEN found with SolTrace was adjusted with experimental data. The transversal IAM obtained by SolTrace presented satisfactory results.

For the SunCNIM prototype, the company gave the heat losses curve. As for the LEPTEN, the heat losses curve was experimentally obtained, using a set of experiments conducted at different temperature levels. The peak efficiency for both cases was obtained iteratively, aiming to reduce the errors between experimental measurements and calculations.

The procedures showed in this section presented a satisfactory performance in identifying these main parameters of an LFC. Although they were developed for the two prototypes analyzed, they can, with minor modifications, be used for any LFC that has adequate experimental measurements.

5 FUNDAMENTALS AND PROCEDURE FOR THE THERMO-HYDRAULIC ANALYSIS

This chapter presents the one-dimensional steady-state thermo-hydraulic model for the HTF flowing inside the receiver. This model is divided into two sections, the thermal and the pressure drop. These models were developed part in Engineering Equation Solver (EES) and part in Matlab with the extension CoolProp to obtain the properties of the water. The model was used both to the single tube receiver for the SunCNIM LFC as for the multi-tube receiver from the LEPTEN LFC prototype. Some adjustments were needed in order for the model to fit to each of the different workbench geometries. These adjustments are also described in details, in the following.

5.1 Thermal model

The energy balance for a solar concentrator presented before is repeated at equation (5.1). It represents a balance between the input solar energy reaching the absorber element and the heat that this element exchanges with the environment.

$$\dot{Q}_{abs} = A_m \, DNI \, \eta_{0^o} \, IAM - \dot{Q}_{HL} \tag{5.1}$$

The left side of the equation shows the heat absorbed by the HTF, which represents the useful heat gain. On the right side of the equation, the first term is with respect to the total concentrated radiation heat absorbed by the absorber element. The η_{0^o} was experimentally obtained, and it takes into account the geometrical and optical properties of the elements of the workbench, such as the real curvature of the mirrors, the solar tracking and the reflectivity, transmissivity and absorptivity of the optical elements. The IAM was obtained part experimentally and part theoretically, and it represents the changes of efficiency with respect to the inclination of the sunray vector.

The second term of the right-hand side is the thermal losses. This parameter was also obtained experimentally, and a heat loss curve is used on further calculations as presented in section 4.3.1.3.

The thermal model uses the principle of equation (5.1). The receiver is divided into a number of infinitesimal segments, such as the absorber tubes. This was done to approach both the heat losses and the heat gain on each absorber tube. The use of these equations is straightforward

for the single tube absorber from SunCNIM, however some adaptations were done with respect to the multi-tube receiver from the LEPTEN prototype. Figure 5.1 shows the nodal structure of the model developed to analyze the receiver.
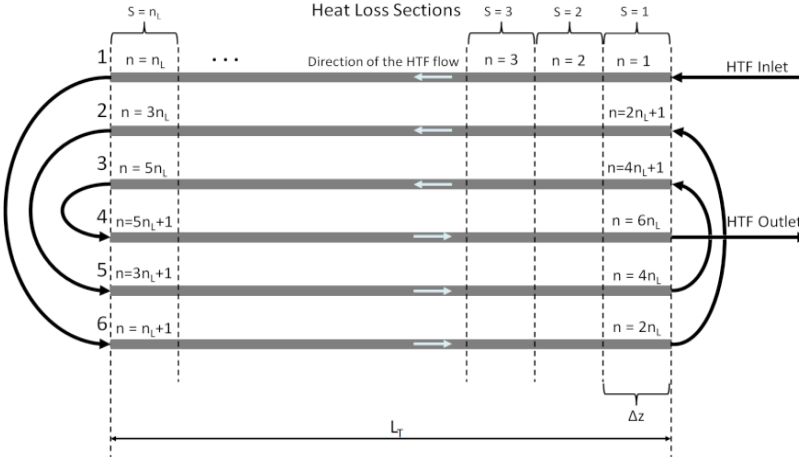
Figure 5.1 - Nodal structure of the model developed to analyze the LEPTEN multi-tube receiver.

The heat losses, in W/m, are usually represented by an empirical correlation for linear concentrators. For the scheme of multi-tube presented above is expressed by the following equation.

$$\dot{Q}_{HL}(S) = \left(a \, (T_{HTF,m}(S) - T_{amb})^2 + b \, (T_{HTF,m}(S) - T_{amb})\right) \Delta z \qquad (5.2)$$

The heat loss is calculated for each section S. The temperature of the HTF used in the sections is the mean temperature of the HTF on all tubes at the respective section, as seen in Figure 5.1. The mean temperature is defined in equation (5.3).

$$\begin{aligned} T_{HTF,m}(S) = \big(&T_{HTF}\,(S) + T_{HTF}\,(2n_L + S) + T_{HTF}\,(4n_L + S) \\ &+ T_{HTF}\,(6n_L + 1 - S) + T_{HTF}\,(4n_L + 1 - S) \\ &+ T_{HTF}\,(2n_L + 1 - S))/6 \end{aligned} \qquad (5.3)$$

The nodal marker S represents the segmentation of the receiver, as the nodal marker n represents the segmentation of the tubes. For the SunCNIM LFC both are the same. This parameter ranges from 1 to n_L,

where $n_L = L_T/\Delta z$. In this iterative procedure, the heat loss at the first section depends on both the temperature on the first segment of the first absorber tube, and the temperature of the last segment of the last absorber tube. First of all, the temperature distribution on the absorber tubes is obtained, followed by the heat losses on all sections. The heat loss distribution is then used to obtain a new distribution of temperature, and this is repeated until it reaches a convergence.

The heat absorbed by the receiver on each section S is described by equation (5.4).

$$\dot{Q}_{abs}(S) = (A_m \, DNI \, \eta_{0^o} \, IAM)\frac{\Delta z}{L_T} - \dot{Q}_{HL}(S) \tag{5.4}$$

It is noteworthy that each section has one segment of each of the six tubes. For each tube, the heat absorber has two different configurations inside the model developed. One, that is the more simplified case, considers the heat equally distributed among all tubes, and other considers the concentrated radiation distribution described in section 4.2.

Taking as example the first absorber tube, with the domain of n from 1 to n_L, where S = n. The heat absorbed by the first tube is $\dot{Q}_{abs,1}$, defined in equation (5.5). The term $\varphi_1(\theta_T)$ represents the curve of concentrated radiation for the first tube. Each tube has a different curve as stated before. The sum of all the six terms, for a respective θ_T, is equal to one.

$$\dot{Q}_{abs,1}(n) = \dot{Q}_{abs}(n) \, \varphi_1(\theta_T) \tag{5.5}$$

The same logic follows to the subsequent tubes. Summarizing, regarding heat losses, the absorber is divided in $L_T/\Delta z$ sections, with $L_T = 12$ m for the LEPTEN workbench. With respect to the heat gain at the HTF, the absorber tubes are considered as one tube of 6 L_T of length. The model is divided into two sections.

At the HTF inside the absorber tubes, from n = 1 to 6 n_L, the energy balance follows equation (5.6), where h is the enthalpy of the HTF.

$$h(n) = \frac{\dot{Q}_{abs,1}(n)}{\dot{m}} + h(n-1) \tag{5.6}$$

The temperature can be found with the outlet enthalpy and pressure on the node. The pressure is obtained through the pressure drop model

that will be discussed furthermore. In addition, the quality (x) of the HTF is checked for each node, to determine which pressure drop model is used, the single-phase of two-phase flow.

5.2 Pressure drop model

5.2.1 Single-phase flow

For estimating the single-phase frictional pressure drop, the Fanning equation is used, as showed in equation (5.7). It is noteworthy that the Darcy-Weisbach friction factor is also commonly used on the literature, and it is related by a factor of four times the Fanning friction factor (FILIP; BĂLTĂREŢU; RADU-MIRCEA, 2014).

$$\left(\frac{dp}{dz}\right) = \frac{f_{1ph} \, u_L{}^2 \, \rho_L}{2 \, D_i} \tag{5.7}$$

Where u_L is the velocity of the liquid, ρ_L is the density of the liquid, D_i is the internal diameter of the absorber tube and f_{1ph} is the single-phase friction factor. The friction factor was obtained by means of the Hagen–Poiseuille correlation for laminar flow ($Re \geq 3000$) and by the Blasius correlation for turbulent flow ($Re \leq 2300$). A transition region between the laminar and turbulent regimes was used as showed by (FILIP; BĂLTĂREŢU; RADU-MIRCEA, 2014).

$$f_{1ph} = 16 \, Re^{-1} \tag{5.8}$$

$$f_{1ph} = f(Re = 2300) + \frac{\left(f(Re = 3000) - f(Re = 2300)\right)}{3000 - 2300} \, (Re - 2300) \tag{5.9}$$

$$f_{1ph} = 0.0791 \, Re^{-0.25} \tag{5.10}$$

Equation (5.8) is used for Re≤2300, equation (5.10) for Re≥3000, and equation (5.9) for 2300<Re<3000.The Reynolds number is given by equation (5.11).

$$Re = G \, \frac{D_i}{\mu} \tag{5.11}$$

Where G is the total mass flow rate per of unit area, called mass velocity, presented at equation (5.12).

$$G = \frac{\dot{m}}{A_{Pipe}}$$ (5.12)

In addition, the Colebrook-White friction factor correlation was also used (BARR; WHITE, 1981), since it was developed for industrial piping, taking into account the surface roughness (ε). The friction factor is obtained iteratively in this correlation.

$$\frac{1}{\sqrt{f_{1ph}}} = -4 \log_{10}\left(\frac{\varepsilon}{3.7 D_i} + \frac{1.26}{Re \sqrt{f_{1ph}}}\right)$$ (5.13)

For the elbows and connections between the six absorber tubes the equivalent length method was used. The equivalent length of the bends and connections can be seen in the Appendix C.

5.2.2 Two-phase flow

One of the goals of the model is to evaluate the pressure drop in a case of DSG. Some models were used in order to compare their pressure drop with experimental data.

The first and simplest case is the homogeneous model, which uses the same equations as for the single phase flow, however with the properties of the fluid modeled as a mixture of steam and liquid (WALLIS, 1969a). This model is only suitable for low qualities of steam, because it considers the two phases of the flow travelling with the same speed, and well mixed in the cross section of the tube. It may reproduce relatively well bubbly flows, but it is not physically representative for a DSG collector that encounters several flow patterns throughout its length. The subscript H on the equations represents the homogeneous mixture, and the subscripts V and L represents the Vapor and Liquid phases. The dynamic viscosity and density of the homogeneous mixture is given by equations (5.14) and (5.15) respectively.

$$\mu_H = \left(\frac{x}{\mu_V} + \frac{1-x}{\mu_L}\right)^{-1}$$ (5.14)

$$\rho_H = \left(\frac{x}{\rho_V} + \frac{1-x}{\rho_L}\right)^{-1} \tag{5.15}$$

All other calculations follow the single-phase procedure, with the properties used being the homogeneous mixture ones. As an example, the Reynolds of the mixture is obtained similarly to equation (5.11), with the μ_H used instead of μ.

Other models use different approaches. In the separated flow models, the two streams are artificially separated, flowing in two separated cylinders, or having an interface between the liquid and vapor phase. This allows different velocities for the two flow streams, the liquid and the steam. The frictional pressure drop models for separated flow do not take into consideration the flow pattern inside the tube.

The Lockhart and Martinelli (LOCKHART; MARTINELLI, 1949) is the first method to predict the pressure drop for two-phase flows based on a two-phase multiplier for the vapor-phase flow or for the liquid-phase flow, represented by ϕ_V^2 and ϕ_L^2 respectively (CAREY, 2018; WALLIS, 1969b). The pressure drop can be obtained using equations (5.16), (5.17) and (5.18).

$$\left(\frac{dp}{dz}\right) = \left(\frac{dp}{dz}\right)_L \phi_L^2 = \left(\frac{dp}{dz}\right)_V \phi_V^2 \tag{5.16}$$

$$\left(\frac{dp}{dz}\right)_L = \frac{2\,f_L\,G^2\,(1-x)^2}{D_i\,\rho_L} \tag{5.17}$$

$$\left(\frac{dp}{dz}\right)_V = \frac{2\,f_V\,G^2\,x^2}{D_i\,\rho_V} \tag{5.18}$$

The two phase friction multipliers are expressed by the following equations (CHISHOLM, 1967).

$$\phi_L^2 = 1 + \frac{C}{X} + \frac{1}{X^2} \tag{5.19}$$

$$\phi_V^2 = 1 + C\,X + X^2 \tag{5.20}$$

where the Lockhart- Martinelli parameter X is obtained as the following dependence (equation (5.21)).

$$X^2 = \left(\frac{dp}{dz}\right)_L \Bigg/ \left(\frac{dp}{dz}\right)_V \tag{5.21}$$

The Chisholm parameter on the specificities of the flow, and rather if each part of the flow is laminar (L) or turbulent (T), as showed in equation (5.22).

$$C = \begin{cases} 5; & Re_L < 1500 \; and \; Re_V < 1500 & \text{L – L case} \\ 10; & Re_L > 1500 \; and \; Re_V < 1500 & \text{T– L case} \\ 12; & Re_L < 1500 \; and \; Re_V > 1500 & \text{L – T case} \\ 20; & Re_L > 1500 \; and \; Re_V > 1500 & \text{T – T case} \end{cases} \tag{5.22}$$

The Reynolds number for the liquid and vapor phase are calculated using the following equations:

$$Re_L = \frac{[G\,(1-x)]D_i}{\mu_L} \tag{5.23}$$

$$Re_V = \frac{(G\,x)\,D_i}{\mu_V} \tag{5.24}$$

Other correlation used was the Friedel correlation (FRIEDEL, 1979). It proposes a liquid-only multiplier for the two-phase flow, as showed in the equations (5.25) and (5.26).

$$\left(\frac{dp}{dz}\right) = \left(\frac{dp}{dz}\right)_L \phi_{LO}^2 \tag{5.25}$$

$$\phi_{LO}^2 = (1-x)^2 + x^2 \left(\frac{\rho_L}{\rho_V}\right)\left(\frac{f_{VO}}{f_{LO}}\right) + 3.24x^{0.78}(1-x)^{0.224} \\ \left(\frac{\rho_L}{\rho_V}\right)^{0.91}\left(\frac{\mu_V}{\mu_L}\right)^{0.19}\left(1-\frac{\mu_V}{\mu_L}\right)^{0.7} Fr_{2ph}^{-0.045}\, We_{2ph}^{-0.035} \tag{5.26}$$

where σ is the surface tension; Fr_{2ph} and We_{2ph} are the Froude and Weber numbers, respectively; f_{VO} and f_{LO} are the friction factors calculated for a case with vapor only and liquid only flow configuration.

$$Fr_{2ph} = \frac{G^2}{g\,D_i\,\rho_H{}^2} \tag{5.27}$$

$$We_{2ph} = \frac{\dot{G}^2 \, D_i}{\sigma \, \rho_H} \tag{5.28}$$

Another correlation used was the one proposed by Müller-Steinhagen and Heck (MÜLLER-STEINHAGEN; HECK, 1986). This approach considers a combination of the flows of each phase similarly, as considered by the Friedel correlation. The subscript "k" on the equations below can be changed for liquid only "LO" or vapor only "VO", depending on the case analyzed.

The Reynolds number for each of the flows are calculated considering the mass velocity, as equation (5.29).

$$Re_k = \frac{G \, D_i}{\mu_k} \tag{5.29}$$

The friction factor follows equation (5.30).

$$f_k = \begin{cases} 16 \, Re_k^{-1}; & for \; Re_k \leq 1187 \\ 0.0791 \, Re_k^{-0.25}; & for \; Re_k > 1187 \end{cases} \tag{5.30}$$

The pressure drop can be obtained for each phase as showed in equation (5.31).

$$\left(\frac{dp}{dz}\right)_k = \frac{2 \, f_k \, G^2}{D_i \, \rho_k} \tag{5.31}$$

The pressure drop for the actual two-phase flow is obtained by the correlation showed on equation (5.32).

$$\left(\frac{dp}{dz}\right) = \left[\left(\frac{dp}{dz}\right)_{LO} + 2\left(\left(\frac{dp}{dz}\right)_{VO} - \left(\frac{dp}{dz}\right)_{LO}\right) x\right] (1-x)^3 + \left(\frac{dp}{dz}\right)_{VO} x^3 \tag{5.32}$$

Finally, the flow pattern based correlation was modeled. This is a phenomenological model proposed by Quibén and Thome (MORENO QUIBÉN; THOME, 2007b, 2007a). It takes into account the physical mechanisms of the flow inside the absorber tube, and therefore it should be more representative of the actual physical situation of the system. The diabatic flow map developed by Wojtan, Ursenbacher and Thome

(WOJTAN; URSENBACHER; THOME, 2005a, 2005b) is used to obtain the flow pattern. The separating conditions between flow patterns are based on the mass velocity of the flow and the vapor quality at transition from intermittent to annular flow. This flow map is based on an experimental work, which included the dynamic void fraction measurements. The flow pattern was obtained from observations of the cross-sectional interface of the liquid–vapor during stratified-types of flow. It is expected that a diabatic flow map carry more information about the physics of the DSG flow from solar concentrator than adiabatic maps. The work of Elsafi (ELSAFI, 2015) had also used this flow map to study DSG on a solar concentrator. Figure 5.2 shows the flow map proposed by Wojtan, Ursenbacher and Thome (WOJTAN; URSENBACHER; THOME, 2005a, 2005b).
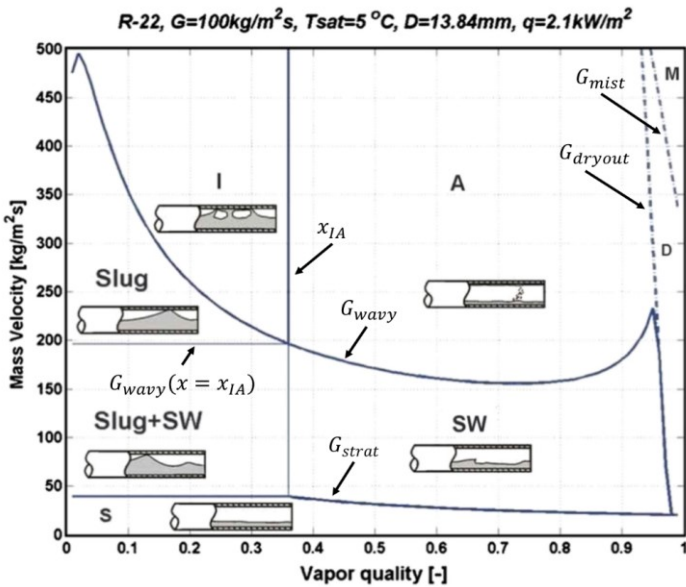
Figure 5.2 – Flow pattern map proposed by Wojtan, Ursenbacher and Thome. Adapted from (WOJTAN; URSENBACHER; THOME, 2005a).

As it can be seen on Figure 5.2, there are some lines dividing the different flow patterns. The regions are divided inside the model by the following logic. If quality is below zero or above one, the single-phase model is running inside the node. Else, for $G < G_{stat}$ the flow is stratified.

Above the stratified line there are some possible flow patter regions. For $x < x_{IA}$, there are three possible regions, one is the slug + stratified wavy flow for $G < G_{wavy}$ $(x = x_{IA})$; another is the slug flow for G_{wavy} $(x = x_{IA}) < G < G_{wavy}$, and the last one is the intermittent flow for $G > G_{wavy}$.

There are four regions for $x > x_{IA}$, that can be obtained by the following sequence of validation; the mist flow for $G > G_{mist}$; the dryout flow for $G > G_{dryout}$; the stratified wavy flow for $G < G_{wavy}$; the annular flow for $G > G_{wavy}$.

The terms G_{strat}, x_{IA}, G_{wavy}, G_{wavy} $(x = x_{IA})$, G_{mist} and G_{dryout} are respectively the stratified mass velocity transition line, the transition quality between intermittent and annular flows, the wavy mass velocity transition line, the wavy flow mass velocity obtained for a quality equal to the x_{IA}, the mist and the dryout mass velocity transition lines. These parameters are obtained through the equations (5.33) to (5.43): The stratified mass velocity transition line follows equation (5.33).

$$G_{strat} = \left[\frac{226.3^2 \ g \ A_L \ A_V{}^2 \ \rho_V \ (\rho_L - \rho_V) \ \mu_L}{x^2 \ (1-x)\pi^3} \right]^{1/3} \tag{5.33}$$

where A_L and A_V are the dimensionless cross-sectional area occupied by liquid and vapor phase respectively.

$$A_L = \frac{A(1-\alpha)}{D_i^2} \tag{5.34}$$

$$A_V = \frac{A\alpha}{D_i^2} \tag{5.35}$$

The void fraction used on calculations is obtained by the Steiner version of the drift flux model of Rouhani and Axelsson for horizontal flows (ROUHANI; AXELSSON, 1970).

$$\alpha = \frac{x}{\rho_V} \left[(1 + 0.12 \ (1-x)) \left(\frac{x}{\rho_V} + \frac{1-x}{\rho_L} \right) \right.$$

$$\left. + 1.18 \ (1-x) \ \frac{(g \ \sigma \ (\rho_L - \rho_V))^{0.25}}{\dot{G} \ \rho_L{}^{0.5}} \right]^{-1} \tag{5.36}$$

The wavy mass velocity transition line is obtained by equation (5.37).

$$G_{Wavy} = \left[\frac{16\,A_{VD}{}^2\,g\,D_i\,\rho_L\,\rho_V}{x^2\,(1-(2\,h_{LD}-1)^2)^{0.5}\pi^2}\left[\frac{\pi^2}{25\,h_{LD}^2}\left(\frac{We}{Fr}\right)_L^{-1}+1\right]\right]^{0.5}+50 \quad (5.37)$$

where h_{LD} is the dimensionless vertical height of liquid, and h_L is the vertical height of liquid. Both can be seen on Figure 5.3, alongside the definition of the dry angle θ_{dry}. The Weber and Froude number on equation (5.37) are obtained for the liquid phase.

$$h_{LD} = \frac{h_L}{D_i} = 0.5\left(1 - \cos\left(\frac{2\pi - \theta_{strat}}{2}\right)\right) \quad (5.38)$$

As seen on the equation (5.38), h_{LD} can also be expressed as a function on the stratified angle, θ_{strat}, that can be obtained by the Biberg approximate expression, showed on equation (5.39) (ELSAFI, 2015).
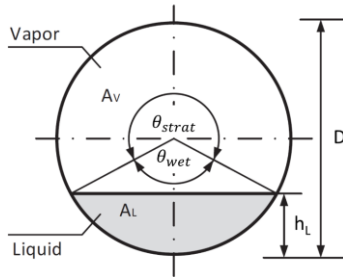
Figure 5.3 - Cross-section of a stratified two-phase flow. Adapted from (ELSAFI, 2015).

$$\theta_{strat} = \{\pi(1-\alpha) + (3\pi/2)^{1/3}[1 - 2(1-\alpha) + (1-\alpha)^{1/3} - \alpha^{1/3}]$$
$$- 1/200\,(1-\alpha)\alpha[1 - 2(1-\alpha)][1 \quad (5.39)$$
$$+ 4((1-\alpha)^2 + \alpha^2)]\}$$

The dryout and mist mass velocity transition curves are given by equations (5.40) and (5.41).

$$G_{dryout} = \left[\frac{1}{0.235}\left(ln\left(\frac{0.58}{x}\right) + 0.52\right)\left(\frac{D_i}{\rho_V\,\sigma}\right)^{-0.17}\right.$$
$$\left.* \left(\frac{1}{g\,D_i\,\rho_V\,(\rho_L - \rho_V)}\right)^{-0.37}\left(\frac{\rho_V}{\rho_L}\right)^{-0.25}\left(\frac{q''}{q''_{crit}}\right)^{-0.7}\right]^{0.926} \qquad (5.40)$$

$$G_{mist} = \left[\frac{1}{0.0058}\left(ln\left(\frac{0.61}{x}\right) + 0.57\right)\left(\frac{D_i}{\rho_V\,\sigma}\right)^{-0.38}\right.$$
$$\left.* \left(\frac{1}{g\,D_i\,\rho_V\,(\rho_L - \rho_V)}\right)^{-0.15}\left(\frac{\rho_V}{\rho_L}\right)^{0.09}\left(\frac{q''}{q''_{crit}}\right)^{-0.27}\right]^{0.943} \qquad (5.41)$$

where q'' is the wall heat flux given by the thermal model presented before, and in q''_{crit} is the critical heat flux for nucleate pool boiling (equation (5.42)) proposed by Zuber (ZUBER, 1959), both given in W/m^2.

$$q''_{crit} = 0.131\,\rho_V^{0.5}\,h_{LV}\,(g\,(\rho_L - \rho_V)\sigma)^{0.25} \qquad (5.42)$$

The transition quality between the intermittent and annular flows is given by equation (5.43).

$$x_{IA} = \left[\left(0.34^{1/0.875}\left(\frac{\rho_V}{\rho_L}\right)^{-1/1.75}\left(\frac{\mu_L}{\mu_V}\right)^{-1/7}\right) + 1\right]^{-1} \qquad (5.43)$$

With the flow pattern model implemented, it is possible to develop a flow pattern dependent pressure drop model. The model used is the one proposed by (MORENO QUIBÉN; THOME, 2007b, 2007a).

The subscripts 2ph, S, Slug, I, SW, A, dryout, mist represent respectively two-phase flow and stratified, slug, intermittent, stratified-wavy, annular, dryout and mist flows.

For stratified flow, the pressure drop can be obtained by equations (5.44) to (5.46):

$$x < x_{IA}: \Delta p_{S\,(x < x_{IA})}$$
$$= \Delta p_{LO}\left(1 - \frac{\alpha}{\alpha_{IA}}\right)^{0.25} + \Delta p_{S\,(x \geq x_{IA})}\left(\frac{\alpha}{\alpha_{IA}}\right)^{0.25} \qquad (5.44)$$

$$x > x_{IA}: \Delta p_{S\,(x \geq x_{IA})} = 4\left(f_{2ph,S}\right)\left(\frac{L}{D_i}\right)\frac{\rho_V\,u_V^2}{2} \qquad (5.45)$$

$$f_{2ph,S} = \left(\frac{\theta_{strat}}{2\pi}\right) f_V + \left[1 - \left(\frac{\theta_{strat}}{2\pi}\right)\right] f_{2ph,A} \tag{5.46}$$

For slug and intermittent flows, the pressure drop follows equation (5.47).

$$\Delta p_{Slug,I} = \Delta p_{LO} \left(1 - \frac{\alpha}{\alpha_{IA}}\right)^{0.25} + \Delta p_A \left(\frac{\alpha}{\alpha_{IA}}\right)^{0.25} \tag{5.47}$$

The annular pressure drop can be seen on equations (5.48) and (5.49).

$$\Delta p_A = 4(f_{2ph,A}) \left(\frac{L}{D_i}\right) \frac{\rho_V \, u_V^2}{2} \tag{5.48}$$

$$f_{2ph,A} = 0.64 \left[\left(\frac{\delta}{D_i}\right)^{1.2} \left(\frac{(\rho_L - \rho_V) \, g \, \delta^2}{\sigma}\right)^{-0.4} \left(\frac{\mu_V}{\mu_L}\right)^{0.08} We_L^{-0.034}\right] \tag{5.49}$$

For slug + stratified wavy, and stratified wavy, the pressure drop can be seen on equations (5.50), (5.51) and (5.52).

$$\Delta p_{Slug+SW} = \Delta p_{LO} \left(1 - \frac{\alpha}{\alpha_{IA}}\right)^{0.25} + \Delta p_{SW} \left(\frac{\alpha}{\alpha_{IA}}\right)^{0.25} \tag{5.50}$$

$$\Delta p_{SW} = 4(f_{2ph,SW}) \left(\frac{L}{D_i}\right) \frac{\rho_V \, u_V^2}{2} \tag{5.51}$$

$$f_{2ph,SW} = \left(\frac{\theta_{strat}}{2\pi}\right) f_V + \left[1 - \left(\frac{\theta_{strat}}{2\pi}\right)\right] f_{2ph,A} \tag{5.52}$$

The liquid only frictional pressure drop on the equations above are evaluated at x = 0. The average velocities are determined using equations (5.53) and (5.54).

$$u_L = \frac{\dot{G}(1 - x)}{\rho_L(1 - \alpha)} \tag{5.53}$$

$$u_V = \frac{\dot{G}x}{\rho_V \alpha} \tag{5.54}$$

The dryout and mist flow pressure drop are showed on equations (5.55) and (5.58).

$$\Delta p_{dryout} = \Delta p_{2ph}(x_{di}) \\ - \frac{x - x_{di}}{x_{de} - x_{di}} \left[\Delta p_{2ph}(x_{di}) \\ - \Delta p_{2ph}(x_{de}) \right] \tag{5.55}$$

where Δp_{2ph} is the frictional pressure drop evaluated at the inception quality (x_{di}). It can be obtained either for annular or stratified-wavy flow. The mist friction pressure drop (Δp_{2ph}) presented on equation (5.55) is evaluated at the dryout completion quality (x_{de}).

$$x_{di} = 0.58 \, e^{\left[0.52 - 0.235 \, We_V^{0.17} \, Fr_V^{0.37} (\rho_V/\rho_L)^{0.25} (q''/q''_{crit})^{0.70} \right]} \tag{5.56}$$

$$x_{de} = 0.61 \, e^{\left[0.57 - 5.8E^{-3} \, We_V^{0.38} \, Fr_V^{0.15} (\rho_V/\rho_L)^{-0.09} (q''/q''_{crit})^{0.27} \right]} \tag{5.57}$$

$$\Delta p_{mist} = 2f_H \left(\frac{L}{D_i} \right) \frac{\dot{G}^2}{\rho_H} \tag{5.58}$$

$$f_H = 0.079 \left(\frac{\dot{G} D_i}{\mu_H} \right)^{-0.25} \tag{5.59}$$

The Chisholm correlation for bends and interconnection was used (CHISHOLM, 1980). The equivalent length of the bends and connections used is the same as described for the single-phase pressure drop case, and can be seen on Appendix C.

The two-phase multiplier proposed by Chisholm is showed on equation (5.19). The constants of the equation are presented on equations (CHISHOLM, 1980; LOBÓN; VALENZUELA, 2013).

$$C = \left(1 + 35 \frac{D_i}{L_{eq}} \right) \left[\left(\frac{\rho_L}{\rho_V} \right)^{0.5} + \left(\frac{\rho_V}{\rho_L} \right)^{0.5} \right] \tag{5.60}$$

$$X = \left(\frac{1 - x}{x} \right)^{0.9} \left(\frac{\mu_L}{\mu_V} \right)^{0.1} \left(\frac{\rho_V}{\rho_L} \right)^{0.5} \tag{5.61}$$

Both the thermal and the pressure drop models were first validated using experimental data from the well instrumented DISS test facility. Results from the model applied to the SunCNIM and LEPTEN LFC are presented in the Chapter 6.

5.3   Model validation with DISS data

The model was compared with experimental data from the DISS facility, obtained from the works of (LOBÓN et al., 2014) and (MOYA; VALENZUELA; ZARZA, 2011). Elbows and interconnections between the PTCs were considered as showed by the work of (LOBÓN et al., 2014).

The main parameters of the experimental cases used to analyze the pressure drop inside the absorber are seen in Table 5.1. Aspects such as heat losses, maximum heat flux in the outer wall and the measurement error can be seen in the work of (LOBÓN et al., 2014).

Table 5.1 – Measurements for different experimental cases for the DISS facility. Extracted from (LOBÓN et al., 2014).

Case	P_{Inlet} [MPa]	T_{Inlet} [ºC]	Mass Flow rate [kg/s]	DNI [W/m^2]
1	3.42	205	0.47	822
2	3.38	196	0.47	807
3	6.25	239	0.55	971
4	6.23	235	0.50	850
5	10.19	237	0.59	960
6	10.20	245	0.62	967

In the study of Lobón et al. (LOBÓN et al., 2014) there are 11 measurement points throughout the absorber tube, and the result of the measured data with the calculated ones for the cases analyzed are showed for three cases, each in one of the three pressure levels showed in Table 5.1.
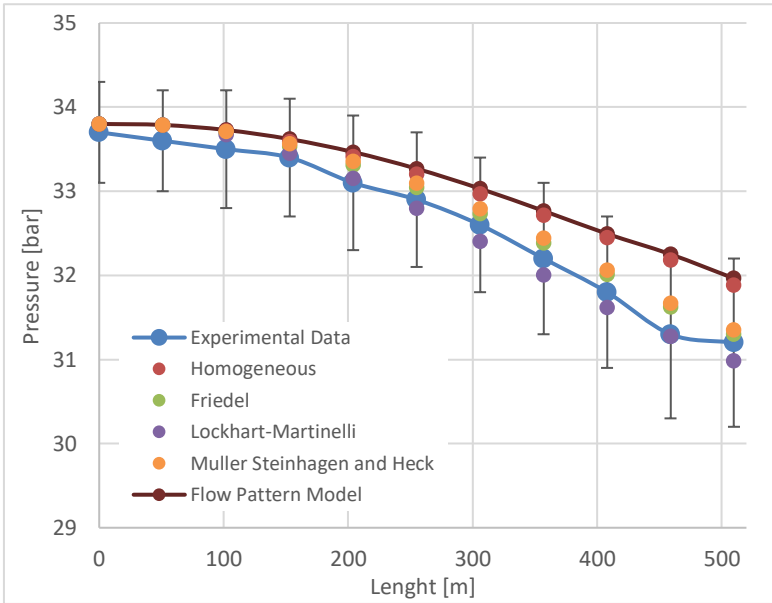
Figure 5.4 - Pressure drop correlations and experimental data for Case 2.
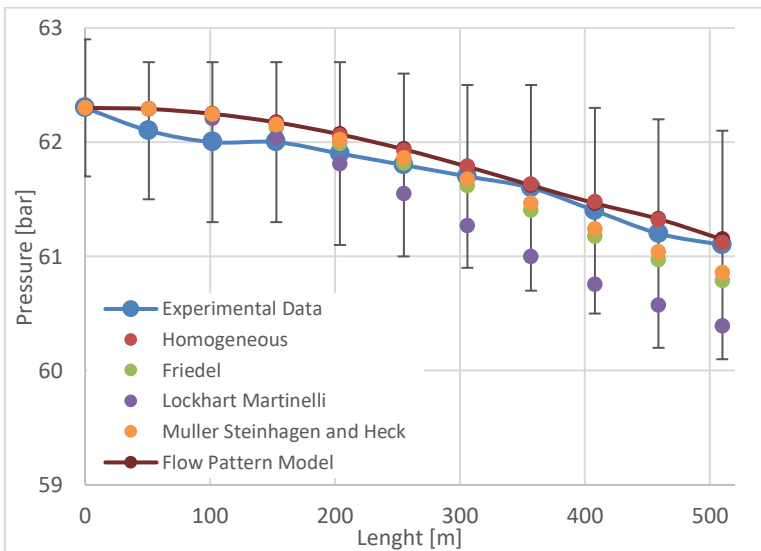
Figure 5.5 - Pressure drop correlations and experimental data for Case 4.
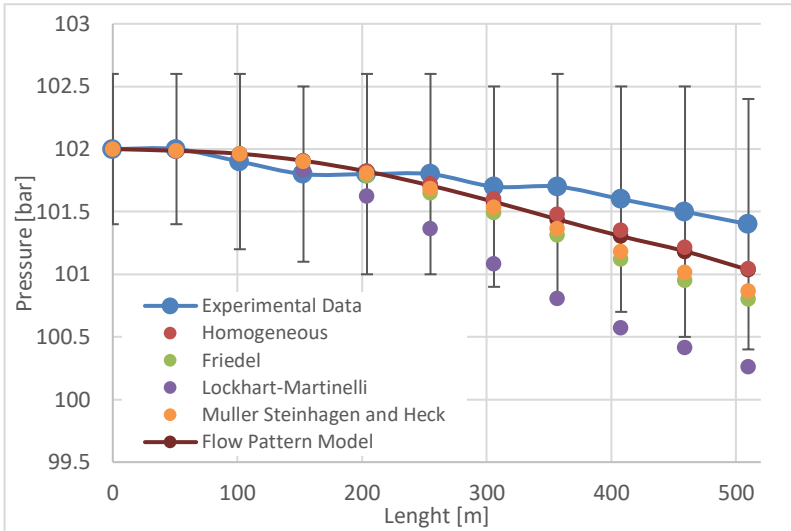
Figure 5.6 - Pressure drop correlations and experimental data for Case 6.

There are two experimental cases for each approximate operational inlet pressure level. The pressure levels are 3.4, 6.25 and 10.2 MPa. The RMSE is obtained for each case of experimental and simulated results, and they are presented in Table 5.2.

Table 5.2 - RMSE in % for all experimental cases analyzed from the DISS facility.

Cases	1	2	3	4	5	6	
Pressure Level [MPa]	3.4	3.4	6.25	6.25	10.2	10.2	RMSE
Homogeneous	1.18	1.25	0.31	0.18	0.11	0.13	0.61
Friedel	0.47	0.54	0.21	0.25	0.19	0.23	0.33
Lockhart Martinelli	0.29	0.41	0.58	0.56	0.40	0.49	0.45
Muller Steinhagen and Heck	0.59	0.65	0.18	0.22	0.17	0.20	0.36
Quibén and Thome Flow Pattern model	1.31	1.38	0.31	0.19	0.12	0.15	0.66

The work of (MOYA; VALENZUELA; ZARZA, 2011) presented the results from simulation using the software RELAP. This software obtained the flow pattern; however, pressure drop was not analyzed. This work is used to verify if the flow pattern obtained by the flow pattern

model used in this work is similar to the one obtained by (MOYA; VALENZUELA; ZARZA, 2011). The results are showed in Figure 5.7.
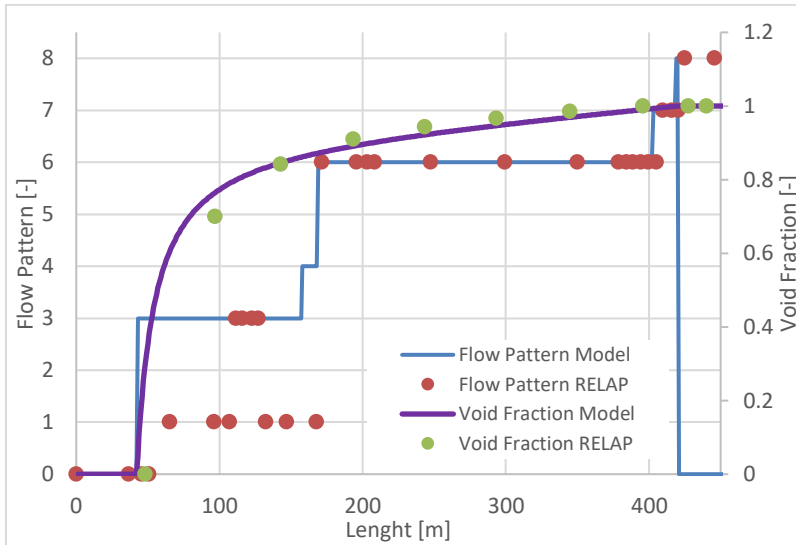
Figure 5.7 - Flow pattern and void fraction comparison to the work of Moya et al. (2011). Flow pattern index: 0 - Single Phase for the Wojtan map and bubbly for RELAP; 1 – Horizontal Stratified; 2 - Slug+SW; 3 - Slug; 4 - Intermittent; 5 - Stratified Wavy; 6 - Annular; 7 - Dryout; 8 – Mist.

5.4   Partial Conclusions

This chapter presented the thermo-hydraulic model used for analyzing the two LFC prototypes. The thermal model is adjusted accordingly to each LFC, and the LEPTEN model also includes the non-uniform concentrated radiation distribution between the six absorber tubes. This non-uniform model presented good agreement with experimental temperature distribution throughout the tubes.

For the pressure drop calculations, two cases were modeled, the single-phase and the two-phase flows. For estimating the single-phase frictional pressure drop, the Fanning equation is used. Two different friction factor correlations were adopted, the Blasius and the Colebrook-White. The latter was developed for industrial piping, taking into account the surface roughness.

For the two-phase flow condition, some correlations were modeled. They are the homogeneous; Lockhart and Martinelli; Friedel; Müller-Steinhagen and Heck; and a pattern-based correlation. The pattern-based correlation is a phenomenological model proposed by Quibén and Thome (MORENO QUIBÉN; THOME, 2007b, 2007a). The diabatic flow map developed by Wojtan, Ursenbacher and Thome (WOJTAN; URSENBACHER; THOME, 2005a, 2005b), is used.

The validation of the model was performed using experimental data from the DISS facility, since it also allows comparing with other works from literature. It was seen that the phenomenological model did not respond particularly well for the low pressure cases. For those, the model underestimated the pressure drop.

Overall, the models that presented the best fit to all the experimental data are those proposed by Friedel and the Muller-Steinhagen and Heck. This confirms the conclusions of (ECK et al., 2003), that showed that the Friedel correlation presents a good agreement for pressure drop when comparing to experimental data from the DISS.

However, for higher pressures the flow pattern based model presented reliable results, with the advantage that this model includes phenomenological considerations of the two-phase flow pattern inside the absorber tube. The flow pattern model presented a maximum RMSE of 1.4% for all cases, and 0.3% for the higher pressure level cases.

Another pressure drop model that presented a surprisingly good fit with the experimental data is the homogeneous. This latter model is not physically representative, since the homogeneous model assumes that both phases have the same velocity and are well mixed. The homogenous model, however, should be carefully evaluated. This because the model will be used to analyze the behavior of the CNIM and LEPTEN LFCs, that is different from the DISS in technology, geometry and operational conditions. In that case, for the extrapolation of the model to different cases with no experimental data, the flow pattern based model carries within also the physics of the flow.

The work of (MOYA; VALENZUELA; ZARZA, 2011) is used to compare the flow pattern obtained with the diabatic flow map developed by Wojtan, Ursenbacher and Thome with results from simulation using the software RELAP.

The annular region occupies almost the same region inside the tube for both models. The main difference is on the beginning of the two-phase region, where RELAP showed regions of bubbly, stratified and slug flow, and the model used in this work showed only slug flow.

This indicates that the flow pattern map model is reliable and, despite some differences, it should indicate reasonably well the flow pattern flowing inside the tube. RELAP showed bubbly flow and mist flow in regions with void fraction was zero and one respectively. For those regions, the model of this work indicated single-phase flow.

Overall, the pressure drop model presented good agreement with the experimental data from DISS presented by (LOBÓN et al., 2014) and the flow pattern predicted presented fitted well with the flow pattern obtained by RELAP on the numerical work of (MOYA; VALENZUELA; ZARZA, 2011).

6 THERMO-HYDRAULIC ANALYSIS RESULTS

6.1 SunCNIM LFC

Five operational days with experimental measurements available were chosen to perform the analysis on the prototype from SunCNIM. In order to study a steady state condition, interval windows of experimental data were selected for these days. These windows were defined due to the stability of the operational conditions during their time interval. It is noteworthy that the LFC length of the prototype is relatively smaller than the LFC length of a plant under construction in Pyrénées-Orientales, using the SunCNIM LFC.

In that manner, the experimental measurements performed on the prototype only indicates the flow conditions at small length compared to the plant under construction. The measurements are used only to indicate if the model is performing well for this smaller scale case. The model is then used to estimate the outlet conditions of the plant under construction, considering some key operational conditions.

These operational cases worked with two main pressure levels at the steam separator and temperature levels at the inlet. They are 3 MPa and 225 °C for cases 1, 4 and 5; and 5 MPa and 250 °C for cases 2 and 3. The other operational condition for the experimental cases can be seen in Table 6.1.

Table 6.1 - Operational cases for the SunCNIM LFC.

Case	DNI $[W/m^2]$	θ_i $[^o]$	θ_T $[^o]$	P_{in} [MPa]	T_{in} [°C]
1	736	22.5	4.4	3	225
2	805	23	3.2	5	250
3	871	23.2	2.4	5	250
4	947	40.9	11.7	3	225
5	900	42.3	2.9	3	225

The flow map for the two pressure levels can be seen in Figure 6.1 and Figure 6.2.
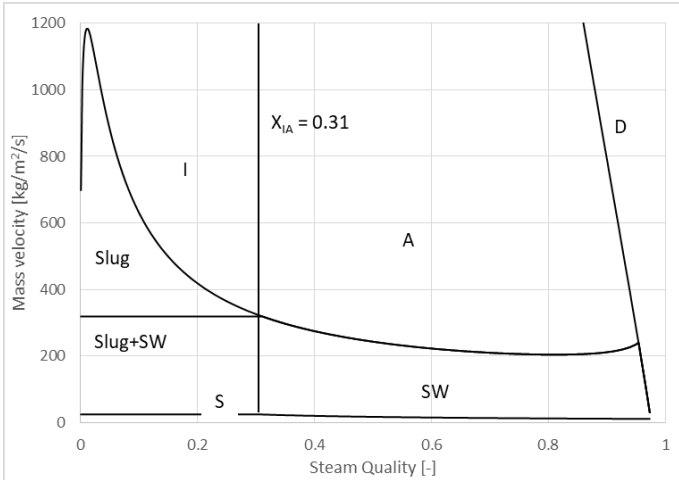
Figure 6.1 - Flow map for the 3MPa operational case.
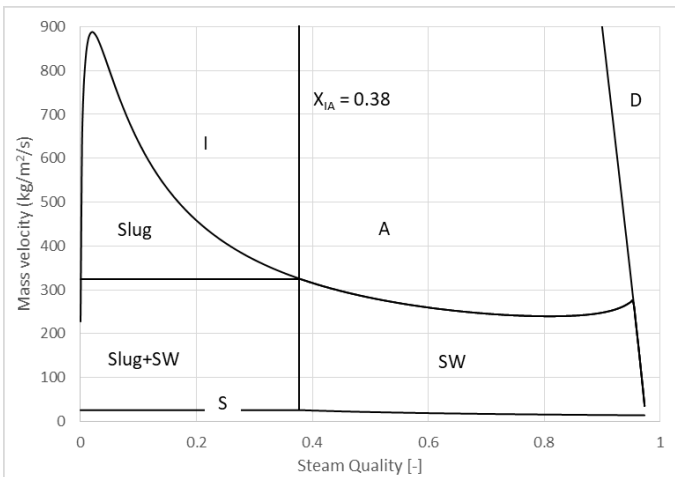
Figure 6.2 - Flow map for the 5MPa operational case.

This work studies the behavior of a line of the same LFC, if it was used for a larger scale, such as the plant under construction. The pressure levels were chosen based on the real operational pressure levels of the power plant as showed by the experimental conditions.

This LFC model is designed to operate with saturated mixture, therefore superheated steam on the solar loop is not desirable, because it

could result in dangerous operational conditions. According to the experimental analysis of (ECK et al., 2008), the best operational condition for the steam separators is an inlet steam quality between 0.7 and 0.8.

The length used in the plant guarantees that, even for the lower pressure level, in nominal condition considering the lowest incidence angle for the region and a high DNI of 900 W/m², the steam quality obtained in the outlet is equal to 0.9. This is not the optimum condition however ensures a safe operational strategy without superheated vapor generation. A mass flow of 1.3 times the nominal mass flow rate would guarantee an outlet steam quality of 0.8. This length also ensures that during average summer days the plant can generate an outlet steam quality on the optimum range, operating at nominal condition, for mass flow rate, pressure and inlet temperature.

The exact inlet pressure is not measured, only the pressure on the outlet of the recirculation pump. For that, the inlet pressure is calculated considering the interconnections, elbow and the piping that goes from ground level to the inlet of the receiver.

The pressure on the steam separator is lower than the pressure on the inlet of the receiver, not only by effects of pressure drop along the flow into the pipe, but also due to the control valves on the outlet of the receiver. Therefore, comparing the pressure measurement on the steam separator with the pressure obtained for the same length by the model is not realistic. In that manner, what is compared between model and measurements is the saturate temperature and outlet steam mass flow rate generated. Table 6.2 shows the error between the calculated and measured steam mass flow rate for the position of the steam generator on the length of the collector.

Table 6.2 - Error between steam mass flow rate measurements and calculations.

Error [%]	Mass flow rate	Temperature
Case 1	2.3	0.36
Case 2	1.3	0.44
Case 3	0.3	0.44
Case 4	0.6	0.37
Case 5	2.8	0.37

The model presented similar pressure drop levels viewed in the DISS project experimental measurements, considering a collector length

equal to the one of the DISS and the geometry of the SunCNIM LFC. Therefore, the model appears to be predicting reasonably well the pressure drop for the plant of SunCNIM. Especially since the operating conditions stays under the superheated steam point, which includes all the experimental data from the DISS.

Figure 6.3 to Figure 6.6 shows the temperature, pressure drop profile throughout the line of LFC of the same length designed for the plant under construction from CNIM. Each figure shows for a different operational condition, as seen in Table 6.1.
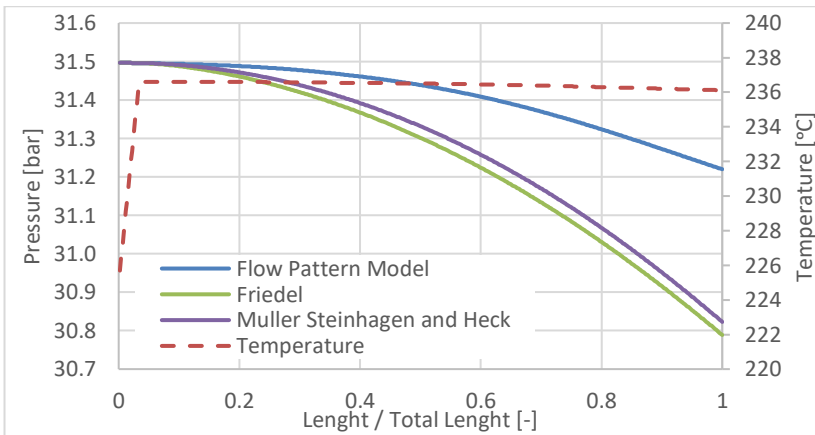
Figure 6.3 - Pressure drop and temperature for Case 1.
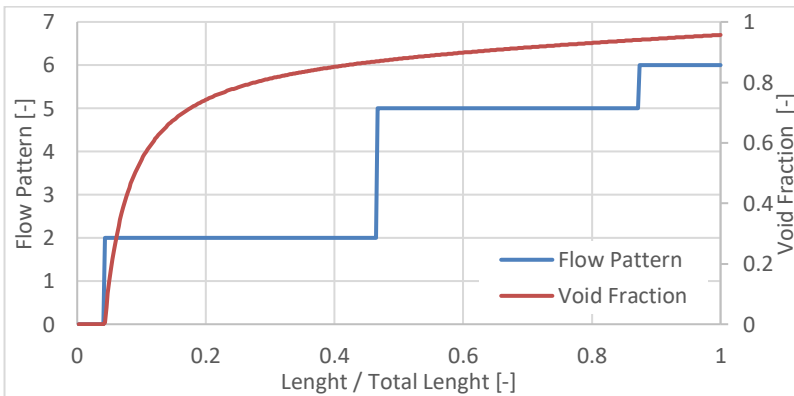
Figure 6.4 - Void fraction and flow pattern for Case 1. Flow pattern index: 0 - Single Phase; 1 – Horizontal Stratified; 2 - Slug+SW; 3 - Slug; 4 - Intermittent; 5 - Stratified Wavy; 6 - Annular; 7 – Dryout.
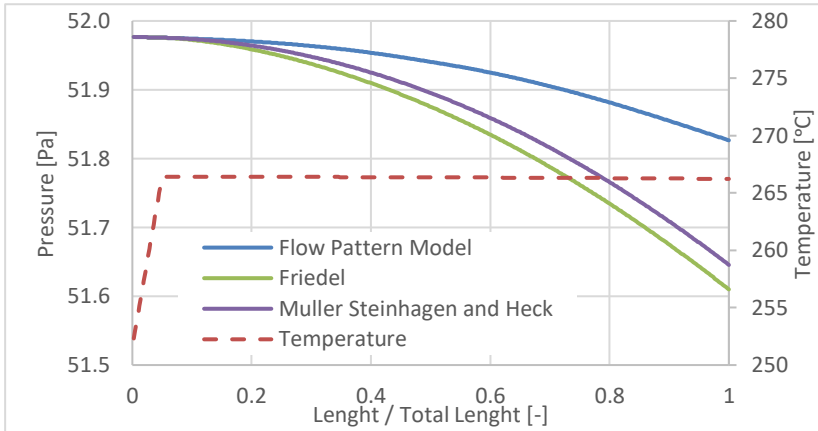
Figure 6.5 - Pressure drop and temperature for Case 2.
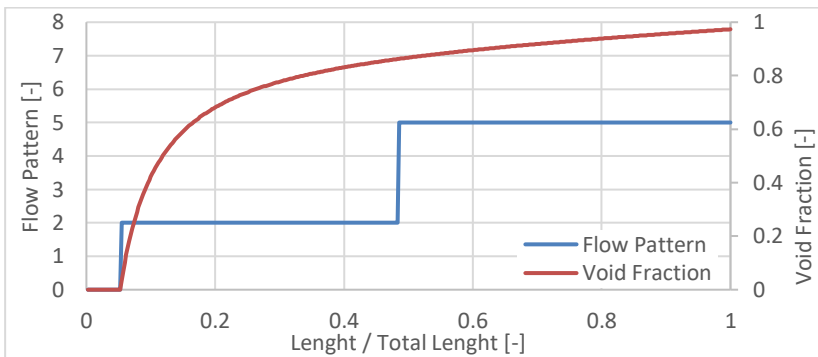
Figure 6.6 - Void fraction and flow pattern for Case 2. Flow pattern index: 0 - Single Phase; 1 – Horizontal Stratified; 2 - Slug+SW; 3 - Slug; 4 - Intermittent; 5 - Stratified Wavy; 6 - Annular; 7 - Dryout; 8 – Mist.

According to the flow map of (WOJTAN; URSENBACHER; THOME, 2005a) for diabatic flows, most of the length of the tube is covered by annular and slug flow, for all test cases. For the mass flow rates analyzed there is no stratified flow.

In a further analysis, the behavior of a larger LFC line, of the plant under construction, is evaluated varying the inlet conditions in order to guarantee the value of 0.8 for the steam quality on the outlet. It is noteworthy that the prototype is designed to operate with saturated steam, and therefore inlet conditions, such as mass flow rate, should change in order not to allow superheating.

Figure 6.7 shows the variation on the efficiency and inlet mass flow due to different DNI. The values are normalized in order to maintain the confidentiality required by SunCNIM. The mass flow rate is normalized with respect to the nominal mass flow found on the experimental data from the LFC prototype. The efficiency from solar to thermal energy is normalized with respect to the collectors' efficiency at zero incidence angle. The inlet mass flow rate changes in order to guarantee the steam quality indicated above. It can be seen that the mass flow rate changes linearly, while the efficiency seems to reach a maximum around 1000 W/m^2.
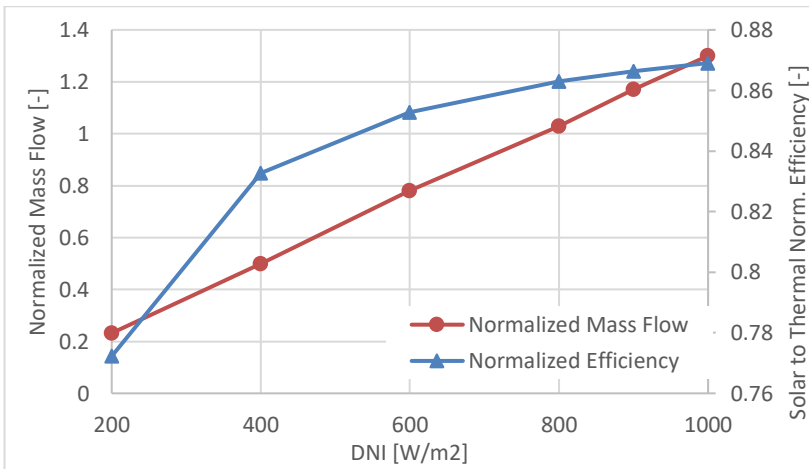
Figure 6.7 - Variation on the calculated efficiency and inlet mass flow rate due to different DNI values.

The flow patterns also suffer changes with different operational conditions, such as the pressure level. Figure 6.8 shows the different flow patterns for 3 and 5 MPa, with a DNI of 800 W/m^2 and the outlet steam quality of 0.8. The higher pressure level tends to hold the single phase condition longer, and it presented a shorter length of annular flow that is preferable for DSG. The influence of the pressure on the flow pattern is visible.
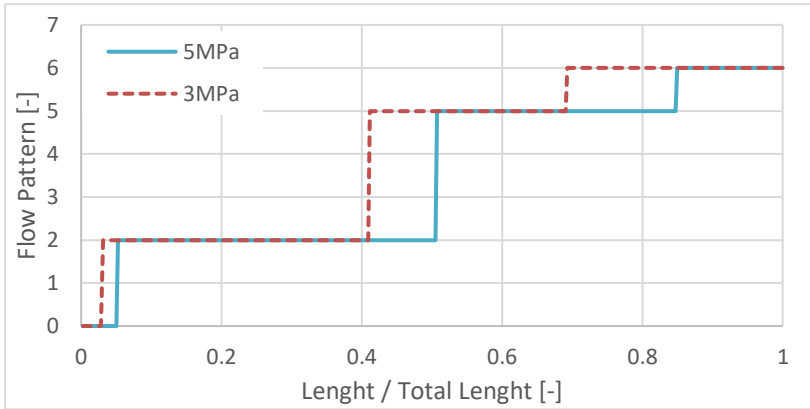
Figure 6.8 - Flow pattern for different inlet pressure and fixed 0.8 outlet steam quality. Flow pattern index: 0 - Single Phase; 1 – Horizontal Stratified; 2 - Slug+SW; 3 - Slug; 4 - Intermittent; 5 - Stratified Wavy; 6 - Annular; 7 – Dryout.

The effect of the DNI on the flow pattern is also analyzed for the 5 MPa pressure level, as showed in Figure 6.9. As seen, higher DNI increases the length of annular flow, while in cases of low DNI as the 400 W/m^2 the annular flow is not even reached. The 3 MPa flow pattern graph for the different DNI presented a similar profile, only slightly dislocated to the left as seen in Figure 6.8.
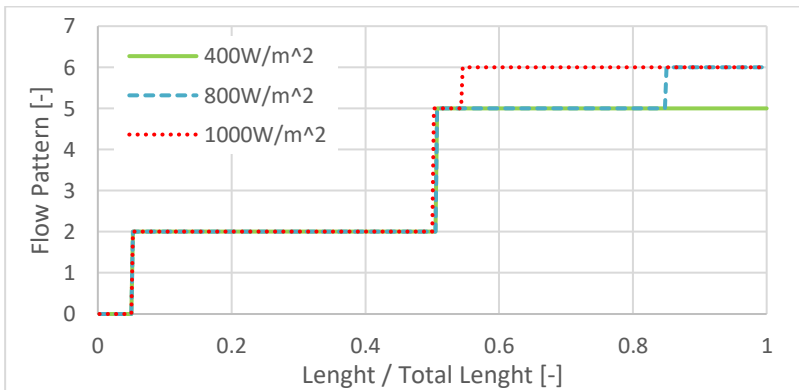
Figure 6.9 - Flow pattern for fixed 5MPa inlet pressure, 0.8 fixed outlet steam quality and different DNI conditions. Flow pattern index: 0 - Single Phase; 1 – Horizontal Stratified; 2 - Slug+SW; 3 - Slug; 4 - Intermittent; 5 - Stratified Wavy; 6 - Annular; 7 – Dryout.

Another analysis was made, changing the inner diameter of the absorber tube in order to see its influence on the flow pattern. Figure 6.10 to Figure 6.11 show the result for the 5 MPa and 3 MPa operational case, considering different DNI levels, with both diameters studied. The reduction made was about 20 % of the diameter.
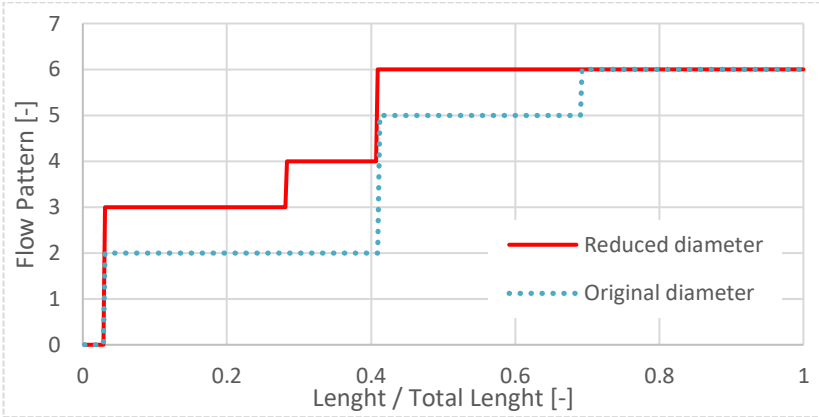
Figure 6.10 - Flow Pattern for original design and reduced diameter, considering 3MPa inlet pressure and 800 W/m^2 of DNI. Flow pattern index: 0 - Single Phase; 1 – Horizontal Stratified; 2 - Slug+SW; 3 - Slug; 4 - Intermittent; 5 - Stratified Wavy; 6 - Annular; 7 – Dryout.
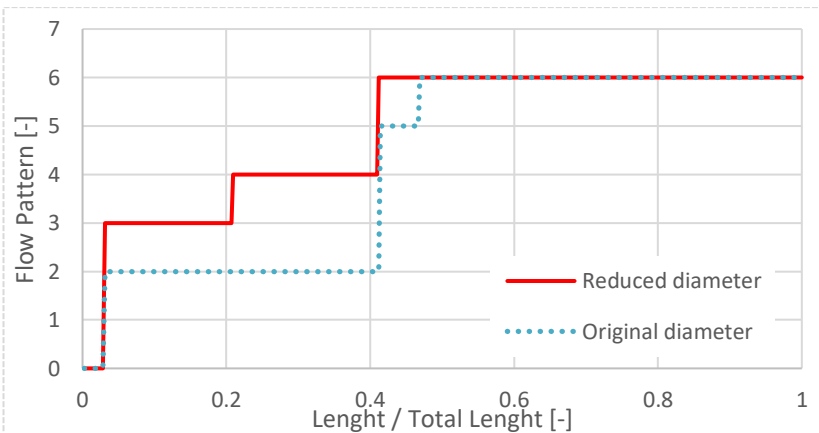
Figure 6.11 - Flow Pattern for original design and reduced diameter, considering 3MPa inlet pressure and 1000 W/m^2 of DNI. Flow pattern index: 0 - Single Phase; 1 – Horizontal Stratified; 2 - Slug+SW; 3 - Slug; 4 - Intermittent; 5 - Stratified Wavy; 6 - Annular; 7 – Dryout.

By changing the inner diameter, the annular flow was encountered for almost 60% of the tube on 3 MPa cases, and almost half of the tube on 5 MPa cases. As seen on the figures, the largest differences are encountered for DNI values around 800 W/m^2. It was also verified that for low DNI values the reduction on the diameter does not affect the flow patter. This is due to the associated low mass flow. For that cases the annular flow is not reached.

6.2   LEPTEN LFC

Initially, the model developed in chapter 5 was analyzed for single-phase experimental data. Later, two-phase flow conditions were studied, and after that, some hypothetical conditions were considered for the LEPTEN LFC.

6.2.1   Single-phase flow test condition

The first set of single-phase flow data included 20 days of tests, from which 55 steady state intervals were extracted for analysis. These tests were performed with heat rejection performed either by the condensers or by the control valve for tests above 100 ºC.

Furthermore, some of the two-phase tests were included on the single-phase section. The initial diagnostic to classify tests as two-phase flow was the visualization of steam exiting the control valve. However, when some of these data sets were analyzed in the model, the exit condition obtained was single phase flow. Since the measured outlet condition gave a temperature close to the saturation temperature, inside the uncertainties of the sensors, it is difficult to affirm the actual exiting condition of these tests.

In addition, the compensation on the overall pressure of the liquid dilatation inside the system could cause the control valve to open. The subcooled liquid when subjected to the ambient pressure would turn to steam.

These tests were then considered here. They include five experimental days, from which 12 steady state intervals were selected. The overall range for all experimental data sets used in this analysis is represented in Table 6.3.

Table 6.3- Range of parameters of tests included on the single-phase flow analysis.

	DNI [W/m²]	P_{in} [bar]	$\dot{v}$ [m³/s]	T_{in} [ºC]	θ_T [º]	θ_i [º]	Days
Max	975	8.7	1.02	155	43	49	27/02
Min	658	1.7	0.3	22	-70	15	28/05

According to the previous analysis, two friction factor correlations were used, the Blasius and the Colebrook. The later considers the roughness of the pipe. All tests intervals stayed inside the turbulent regime. The interconnections between absorber tubes and properties of the tube can be found on Appendix C.

Table 6.4 shows the mean error between measurement and four different model calculations, which included the combination of Blasius and Colebrook with the condition of equal distribution of concentrated radiation on all six tubes, and the model of concentrated radiation presented on section 4.2. The errors (equation (6.1)) were analyzed for thermocouples located in different lengths of the absorber tubes, and for pressure measurement at the outlet. For the distance of 36 m and 60 m, there were two thermocouples installed, indeed the mean value was used. This analysis was performed first for only the first set of data of 55 steady-state intervals

$$Error[\%] = \frac{(X_{Measured} - X_{Calculated})}{X_{Measured}} \frac{1}{100} \qquad (6.1)$$

As expected, the roughness of the tube has an impact on the pressure drop, especially for these types of industrial systems, with welded connections and rusty incrustations. The value of roughness used was of 0.3 mm. This is evidenced by the difference between errors of the Colebrook and Blasius correlations when applied to the LEPTEN LFC system. The measured pressure drop is much higher than the pressure drop obtained using the Blasius correlation, resulting in errors around 50 %. The Colebrook correlation presents much reliable results, with errors around -0.49 %. As stated before, the roughness chosen was taken from table showed in Appendix C, however, for more precise characterization of the LFC, future works could include disassembling the receiver and measurements of the wall roughness.

Table 6.4 – Mean error between measurement and four different model calculations for temperature and pressure drop for the first set of data of 55 steady-state intervals.

	Non-uniform radiation distribution model		Uniform radiation distribution model	
Error [%]	Colebrook	Blasius	Colebrook	Blasius
Temperature - 24 m	1.20	0.98	-5.20	-4.82
Temperature - 36 m	2.83	2.87	-3.52	-4.25
Temperature - 48 m	2.42	2.50	-2.31	-2.62
Temperature - 60 m	1.00	1.05	-1.38	-1.33
Temperature - 66 m	0.89	0.94	-0.47	-0.42
Temperature -72 m	-0.24	-0.18	-0.62	-0.56
ΔP	-0.49	49.86	-0.49	50.11
Mean Temperature	1.35	1.36	-2.25	-2.33

As seen in Table 6.4, the non-uniform concentrated radiation model performed a better prediction of the temperature than the uniform concentrated radiation model. The mean errors considering the non-uniform model stayed around 1.3 %, while for the uniform model these errors were in the order of 2.3 %.

This difference is small, however, as seen on Figure 6.12, the non-uniform concentrated radiation model represents more precisely the temperature profile throughout the absorber tubes. This could have a large impact on the prediction of the LFC behavior, especially for two-phase flow cases, where the position of the beginning of the boiling impacts heavily on the pressure drop.

For the case of the Figure 6.12 the transversal angle during this steady state condition was at -40°. All further analysis will consider only the non-uniform concentrated radiation model presented in section 4.2.

Another typical test day for single-phase flow can be seen in Figure 6.13. The experimental results are plotted alongside with the model results for the Colebrook friction factor. For this case, the pressure drop stayed inside the range of experimental uncertainties. The pressure drop curve obtained with the model presents discontinuities at each 12 meters. They represent the pressure drop on fittings and elbows between susceptive absorber tubes. Since only the absorber tubes lengths are plotted in Figure 6.13, and on all successive graphs of the LEPTEN LFC analysis,

the pressure drop on these interconnections appears as an abrupt drop. The equivalent length from those can be seen in Appendix C.
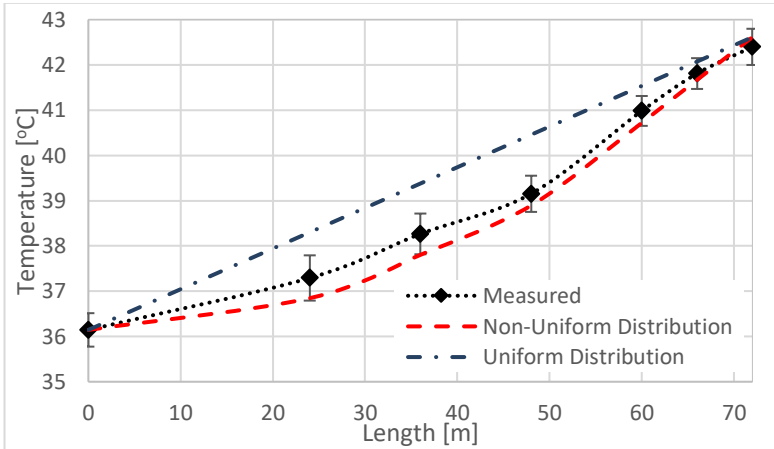
Figure 6.12 - Comparison of the temperature profile throughout the absorber tubes for the uniform and non-uniform radiation distribution models using experimental data from 26/02/2018.
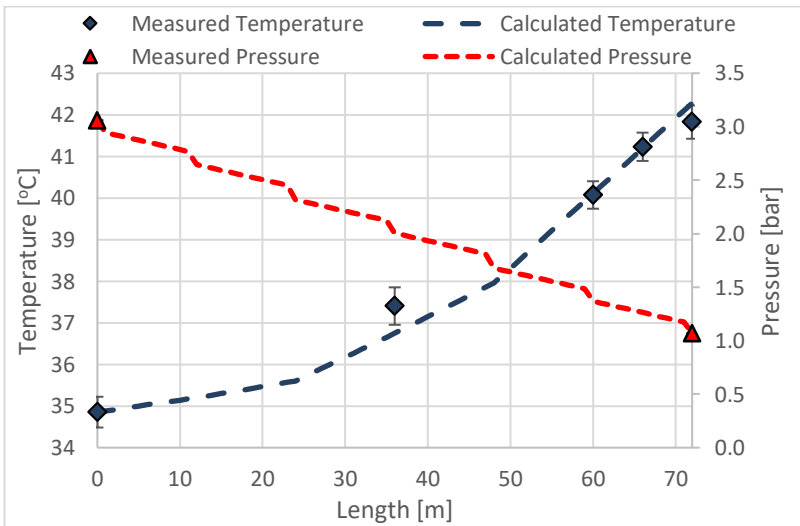
Figure 6.13 – Temperature and pressure throughout the absorber tubes for one steady state interval from the single-phase test of 13/04/2018 compared with model results considering non-uniform concentrated radiation and Colebrook friction factor.

The relation between the mass flow rate and the pressure drop for both friction factor models can be seen in Figure 6.14.
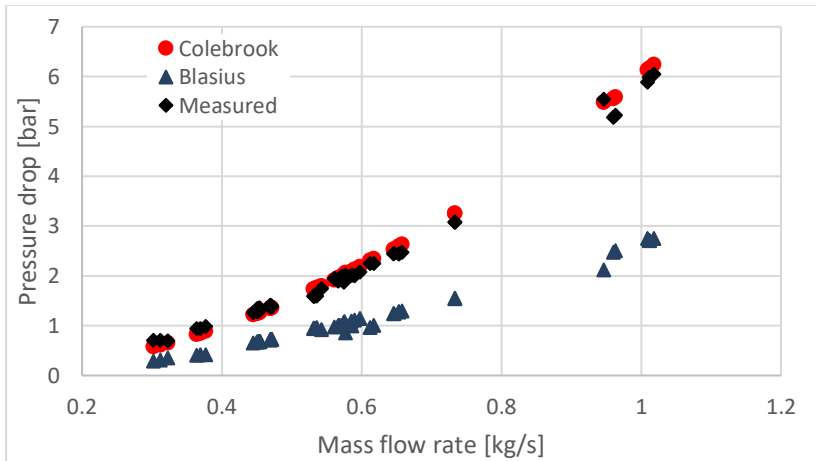
Figure 6.14 - relation between the mass flow rate and the pressure drop for single-phase considering the friction factor correlation of Blasius and Colebrook.

The Blasius correlation underestimates the pressure drop, especially for higher mass flow rate. The Colebrook presented a high concordance with the experimental pressure drop throughout all range of mass flow rate analyzed on this first set of data. The experimental data had a great pressure drop range, varying from less than 1 bar, for mass flow below 0.4 kg/s, up to 6 bar for mass flow around 1 kg/s.

Figure 6.15 shows the pressure drop errors as function of the mass flow rate for the two friction factor models. The higher values of error for the Colebrook model appeared at lower mass flow rate. However, these conditions also presented lower experimental pressure drop, therefore any deviation of the model from the experimental data represents a higher percentage of error. Overall there is not a clear dependency between these two factors. The same can be said from the Figure 6.16, about the pressure drop error and the inlet temperature of the HTF.
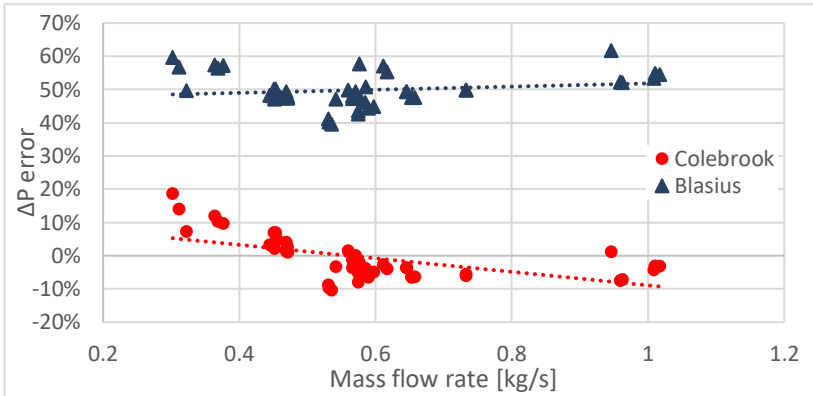
Figure 6.15 - Pressure drop error as function of the mass flow rate for the two friction factor models.
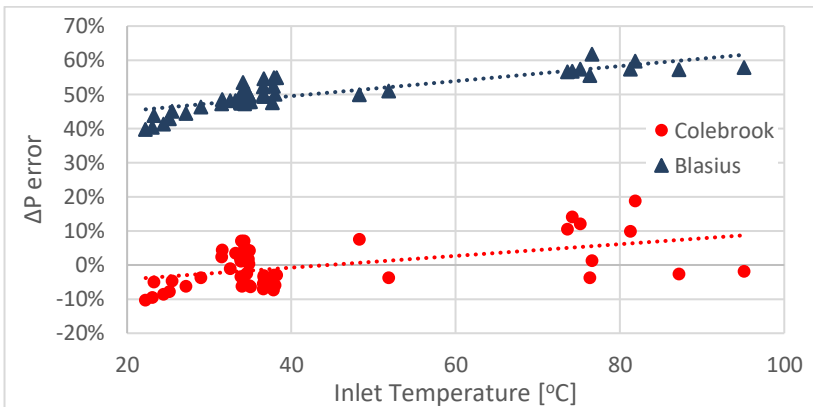
Figure 6.16 - Pressure drop error as function of the inlet temperature for the two friction factor models.

As the Blasius presented such higher errors, this friction factor model will no longer be considered in further analysis. Figure 6.18 summarizes the relation of the pressure drop error for both the temperature and mass flow for the Colebrook case.
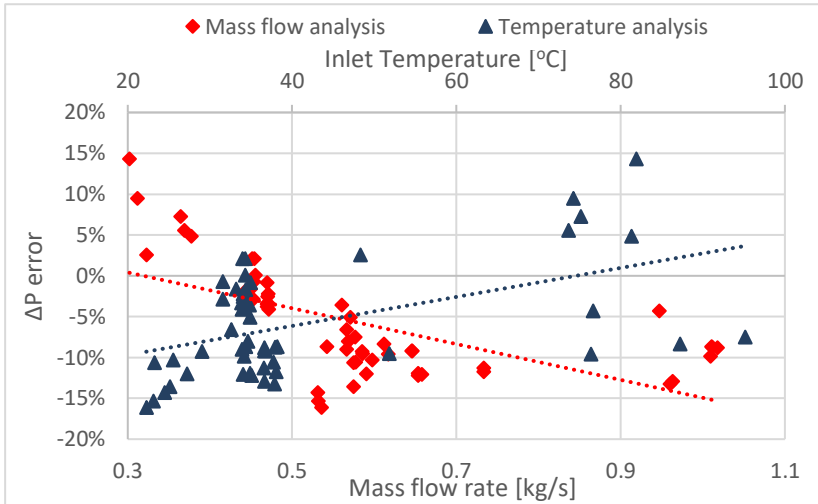
Figure 6.17 - Pressure drop error as function of the inlet temperature and mass flow for the Colebrook friction factor considering the first 55 steady-state intervals.

This graph will be used to compare with the same analysis for the case considering the rest of the single-phase flow data. As stated at the beginning of the section, some of the two-phase flow tests were included in the single-phase flow analysis. These tests include steady-state intervals at higher temperatures. Table 6.5 shows the error comparison between only the first set of data and all the single-phase data. It presents the error between the calculated value of temperature or pressure drop with the value obtained from measurements. This procedure is repeated for only the first 55 steady state intervals, and considering all the 67 steady-state intervals.

It appears that there was not much change on the temperature measurement error. As it can be seen, the measurements at the length of 24 m and 48 m are not showed on the second analysis. This because during the experiments, some thermocouples ceased to operate, and the configuration of the instrumentation changed. The thermocouples of the 24 m and 48 m were deactivated.

Table 6.5 -– Mean error between measurement and model for temperature and pressure drop comparing the first 55 steady-state intervals with all single-phase steady state data.

Error [%]	55 Intervals	67 intervals
Temperature - 24 m	1.20	-
Temperature - 36 m	2.83	2.38
Temperature - 48 m	2.42	-
Temperature - 60 m	1.00	0.81
Temperature - 66 m	0.89	0.75
Temperature -72 m	-0.24	-0.25
ΔP	-0.49	1.97
Mean Temperature	1.35	0.93

These last experiments that came from the two-phase flow tests were performed later, and most of them already had the new instrumentation configuration, without these thermocouples, therefore these two lengths were removed from further work. Figure 6.18 shows the same analysis performed on Figure 6.17 however for the entire set of data.
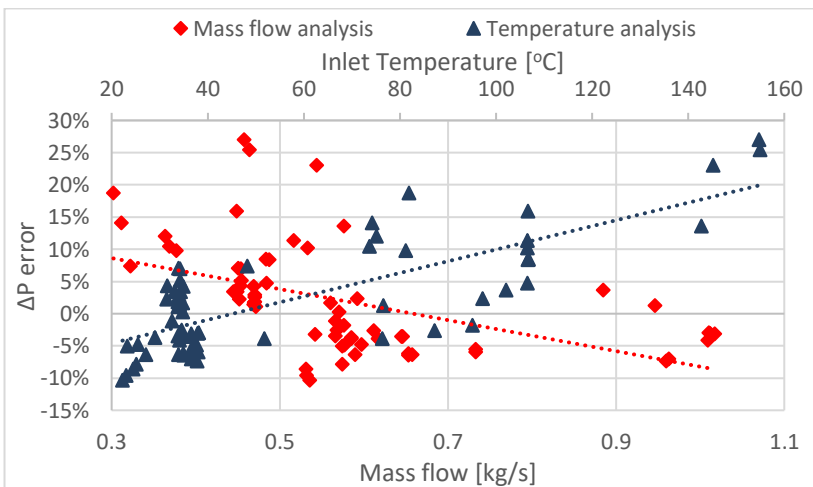
Figure 6.18 - Pressure drop error as function of the inlet temperature and mass flow for the Colebrook friction factor considering all single-phase data.

The last tests added to the analysis were performed at higher temperatures. The influence on the pressure drop error due to the mass flow rate did not had any great change between the points in Figure 6.17 and Figure 6.18, however, it can be seen that the higher errors happened at higher temperatures.

These high errors could also mean that in fact these tests are having a two-phase flow, that is not computed by the model. For that case, the higher temperature values would indeed present a higher experimental pressure drop when comparing with the single-phase model, since in reality they could represent two-phase flow tests. Another possible explanation is that the verification procedure presented in Appendix E is not completely reliable. In addition, leakage at interconnections on higher temperatures could also promote this higher experimental pressure drop. Further analysis is needed to catch the physics on these low mass flow cases. For that, the LFC will receive further instrumentation in the future.

Overall, the single-phase flow model using the Colebrook correlation and the non-uniform concentrated radiation had a satisfactory concordance with the experimental data.

6.2.2   Two-phase flow test condition

Initially, the two-phase flow tests were classified in that manner when steam was visually exiting the control valve. To perform these tests, the pressure inside the steam separator adjusted the desirable saturation temperature. This pressure was set and controlled by the control valve, as described in section 3.2. Only in cases where the desirable temperature was the saturation at ambient pressure that the control valve was not used, and instead the steam was rejected by the by-pass of the control valve, that stayed open during these tests.

At total, 24 steady state conditions were obtained from these tests. However, as stated before, the last 12 of the two-phase flow steady-state conditions did not present a two-phase flow on the outlet when modeled. That leaves only 12 other steady-state intervals with two-phase flow condition at their outlet. This set of data was obtained with a mass flow rate around 0.2 kg/s, a low value comparing to the other tests. For this the two-phase flow condition was obtained. The range of the main parameters for these 12 tests can be seen on Table 6.6.

Table 6.6 - Range of parameters of tests included on the two-phase flow analysis.

	DNI [W/m^2]	P_{in} [bar]	$\dot{v}$ [m^3/s]	T_{in} [ºC]	θ_T [º]	θ_i [º]	Days
Max	965	9.8	0.22	155	12	41	12/04
Min	712	2.0	0.14	22	-70	16	27/05

This set of data was modeled for all the different two-phase flow pressure drop correlations that were considered in the model presented on chapter 5.

Table 6.7 shows the mean error between measurement and different two-phase flow correlations that were implemented in the model. For the single phase flow part of the absorber tubes the Colebrook correlation was used. It was seen that for this set of data, the pressure drop errors were higher, reaching a maximum of 82 % for the homogeneous model, and a minimum of 70 % for the Friedel correlation. The Friedel correlation was reported to be the best one to represent the pressure drop on the DSG solar plant of the DISS facility (FRIEDEL, 1979). The Friedel correlation is used on some further analysis.

This set of two-phase flow data was plotted alongside the single-phase data set, and the influence of both the mass flow and the temperature were evaluated for the pressure drop error, as can be seen in Figure 6.19.

Table 6.7 - Mean error between measurement and model for temperature and pressure drop comparing the set of 12 steady state two-phase flow data. The two-phase flow pressure drop model follows: 1 – Homogeneous; 2 – Friedel; 3 - Lockhart–Martinelli; 4 - Muller-Steinhagen & Heck; 5 – Flow pattern based model.

| Error [%]	1	2	3	4	5
Temperature - 36 m	0.04	0.04	0.04	0.04	0.04
Temperature - 60 m	-1.28	-1.26	-1.26	-1.26	-1.26
Temperature - 66 m	-2.98	-2.54	-2.57	-2.57	-2.58
Temperature - 72 m	-3.95	-2.90	-3.22	-3.21	-3.39
ΔP	81.77	70.26	72.58	72.80	74.05
Mean Temperature	-1.47	-1.27	-1.32	-1.32	-1.34
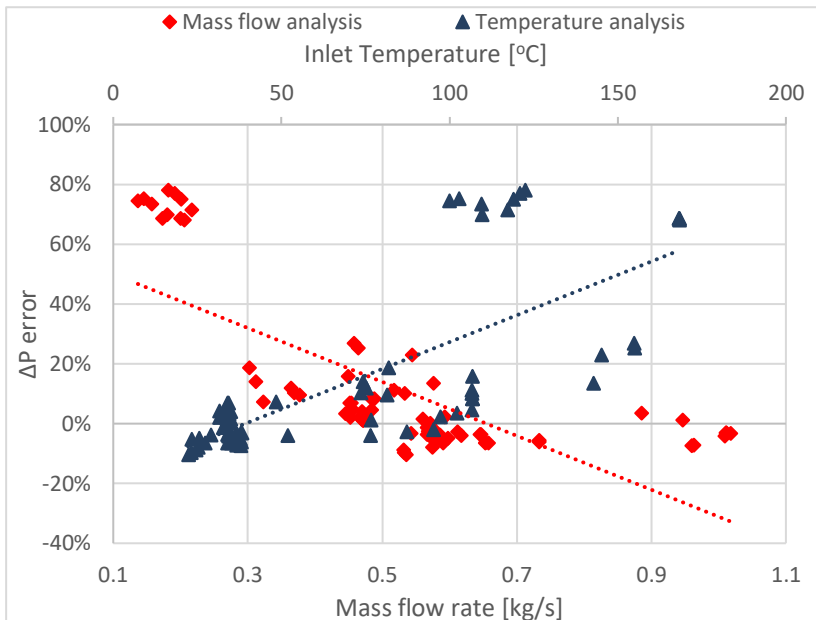
Figure 6.19 - Pressure drop error as function of the inlet temperature and mass flow rate for the Colebrook friction factor and Friedel two-phase pressure drop model, for all set of data.

In this case, it appears that the mass flow rate and the inlet temperature influence the pressure drop error. For higher temperatures, and lower mass flow rate, the pressure drop errors are higher. This was also seen for Figure 6.18, where errors above 15 % were encountered for lower mass flow rate.

It is noteworthy that the higher temperature coincides with the tests at lower mass flow rate. These errors can be related to the volumetric flow rate measured. The calibration test performed was in a qualitative manner, as stated in Appendix B, since no certified agency would calibrate for single phase liquid flow at high temperatures and pressures. The verification, however, is not a rigorous calibration.

The higher temperatures may also favor leakage on the connections between absorber tubes. Actually, on later tests it was possible to see some water dropping from the casing where these connections are insulated. Since it is a closed location, these connections are only going to be tightened when the receiver is lowered for further instrumentation adaptations, on future works. These leakages may also be the reason why the measured pressure drop is much higher than the calculated for these cases.

Another effect that could induce these high errors is if in lower mass flow rate the tube is not completely filled with liquid, especially since at two-phase flow tests the water level at the steam separator drops gradually. This could not be verified experimentally.

In addition, hoses are used to make the interconnection between pipes, and in two-phase flow there is the possibility of steam accumulation inside those curves, which would highly increase the pressure drop.

The pressure drop is also smaller for lower mass flow rate, which implies that these tests are more sensible to errors. Even smaller variations on the output pressure represent a considerable error.

With these assumptions, some other discrepancies were found on the two-phase tests at low mass flow rate. The analysis of one experimental steady-state interval that presented discrepancies is discussed on Appendix F. These discrepancies, however, were not encountered in all the 12 steady state intervals. In fact, for most intervals the measured temperature was much closer to the saturated temperature, staying at the range of uncertainties of both the temperature and pressure sensors. Although for all cases the pressure drop modeled was lower than the one measured.
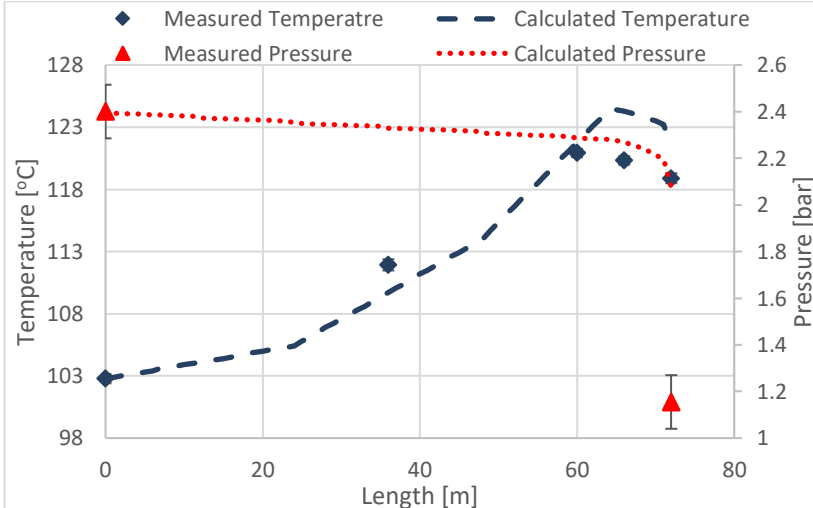
Figure 6.20 – Comparison between measurements and model for the 12/04/2018.

To best understand these behaviors, further adaptation of the receiver is already under study for future works. New pressure sensors will

be installed on other points throughout the absorber tubes. The thermocouples lost will be replaced, and new measurement points added. The flexible hoses will receive a support to stay on the horizontal position during all test, despite the position of the receiver due to the moving receiver. And the circulation pump will be changed in order to achieve more controlled two-phase flow conditions.

As discussed in section 6.1. from the results of the CNIM analysis, for higher pressures the flow pattern based model showed best fitting to the experimental measurements. The tests performed here ranged the inlet pressure from 2.09 to 9.87 bar, with a mean pressure of 4.53. Although the whole system is designed for operating at 23 bar, the pump has a lower pressure limit. As stated, a new pump with magnetic coupling will be acquired for future tests at higher temperature. In sight of current limitations, further analysis is made on a theoretical basis.

Nevertheless, the LFC was capable of operating in DSG satisfactorily, with steam exiting the control valve. The generation of steam was apparently constant, although there was no flowmeter to measure the steam outlet flow. The liquid level sensors presented on the steam separator could verify this constancy. There were three level sensors, equidistant between them, and the time to go from the high level to the medium level sensor was approximately the same as to go to the medium level to the low-level sensor. It can be said that, although more effort should be applied to understand physically what is going on at the receiver, the DSG using the LFC of LEPTEN is feasible.

6.2.3   Further investigation

First, the model is used considering a condition of saturated liquid on the inlet of the receiver. This is a difficult condition to achieve considering the current preheater, pump and control strategy.

Figure 6.21 shows the flow map for the maximum pressure case, of 23 bar, with a volumetric flow rate of 0.2 m^3/s, and a DNI of 900 W/m^2

Figure 6.21 - Flow pattern map for the LEPTEN LFC for 23bar, with a volumetric flow rate of 0.2 m³/s, and a DNI of 900 W/m².

Figure 6.22 shows the flow pattern map for the same conditions, altering only the volumetric flow rate to 0.6 m³/s. The mass flow rate influences only slightly on the peak of the intermittent curve. The DNI also influences the flow pattern map, but only slightly on the dryout curve. However, for all analysis, a DNI of 900 W/m² was considered. The IAM used was 0.9 for all cases, since it represents a typical condition around solar noon for summer.
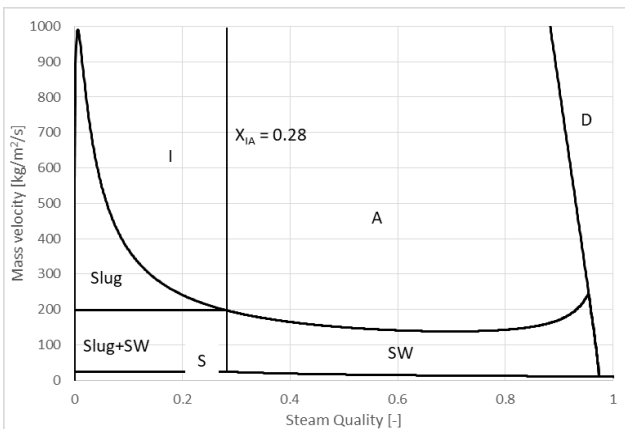
Figure 6.22 - Flow pattern map for the LEPTEN LFC for 23bar, with a volumetric flow rate of 0.6 m³/s, and a DNI of 900 W/m².

To avoid inconsistences on the model, the fluid enters the receiver at a subcooled condition of 0.1 ºC. Figure 6.23 shows the temperature profile throughout the absorber tubes for the different models. As it can be seen the temperature difference is very smaller than the thermocouple uncertainty. These values were obtained by simulation. This is the case for many simulated conditions.

Figure 6.23 - Temperature variation along the absorber tubes calculated with different models considering a saturated condition at the inlet of the LEPTEN LFC for 23 bar and 0.2 m³/s.

The only change in the water temperature along the flow is due to the pressure drop, and the maximum change stayed around 0.7 ºC for the Lockhart-Martinelli correlation, which presented the highest pressure drop off all models. This can be verified on Figure 6.24, that shows the pressure profile throughout the absorber tubes. The pressure drop for this case of low volumetric flow rate stayed at a maximum of 0.3 bar.

150
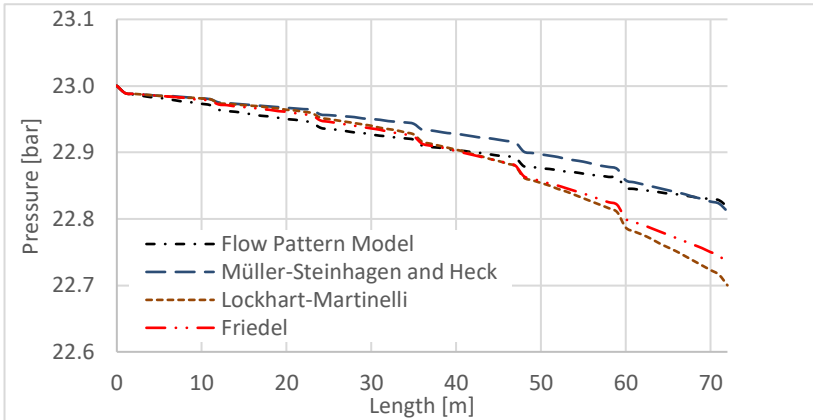
Figure 6.24- Pressure variation along the absorber tubes calculated with different models considering a saturated condition at the inlet of the LEPTEN LFC for 23 bar and 0.2 m³/s.

Table 6.8 shows the outlet conditions for the HTF considering the four models chosen. Regarding the flow pattern pressure drop model, the flow pattern found inside the absorber tubes was slug, throughout all tube.

Table 6.8 - Outlet conditions the LEPTEN LFC considering saturated condition at the inlet for 23 bar and 0.2 m³/s.

Outlet Conditions	Friedel	Lockhart–Martinelli	Müller-Steinhagen and Heck	Flow Pattern Model
Quality [-]	0.0411	0.0412	0.0406	0.0406
Temperature [°C]	218.98	218.91	219.17	219.18
Pressure [Pa]	2.27E+06	2.27E+06	2.28E+06	2.28E+06
ΔP [Pa]	2.69E+04	3.00E+04	1.89E+04	1.82E+04

The same inlet pressure condition was analyzed, however for a different volumetric flow rate, of 0.6 m³/s. Figure 6.25 and Figure 6.26 show respectively the temperature and pressure profile throughout the tube for this case.
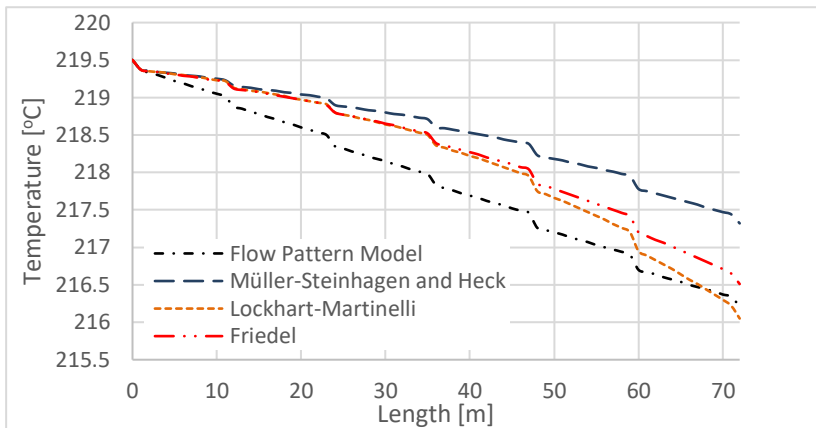
Figure 6.25 - Temperature variation along the absorber tubes calculated with different models considering a saturated condition at the inlet of the LEPTEN LFC for 23 bar and 0.6 m³/s.

Figure 6.26- Pressure variation along the absorber tubes calculated with different models considering a saturated condition at the inlet of the LEPTEN LFC for 23 bar and 0.6 m³/s.

It can be seen on Table 6.9 that for this higher volumetric flow, the pressure drop presented much higher values, with a maximum of around 1.5 bar, which resulted on a maximum temperature difference of water of around 3.5 °C. The flow pattern anticipated by the models throughout all tubes was intermittent.

Table 6.9- Outlet conditions the LEPTEN LFC considering saturated condition at the inlet for 23 bar and 0.6 m³/s.

Outlet Conditions	Friedel	Lockhart–Martinelli	Müller-Steinhagen and Heck	Flow Pattern Model
Quality [-]	0.02032	0.02137	0.0184	0.0211
Temperature [ºC]	216.51	216.05	217.32	216.21
Pressure [Pa]	2.17E+06	2.15E+06	2.20E+06	2.15E+06
ΔP [Pa]	1.33E+05	1.52E+05	9.88E+04	1.46E+05

This shows that for higher volumetric flows, higher are the pressure drop as expected. For this small prototype these values do not make the LFC unfeasible, however, for real applications it is expected a much longer line of LFC. This case will be evaluated further on this section.

For the 0.2 and 0.6 m³/s, the vapor mass flow rate generated was of 24.3 kg/h and 36.5 kg/h respectively. The later condition however, produced steam at saturation temperature of around 3 °C lower.

Another case was analyzed, considering a different pressure level of 10bar. Figure 6.27 shows the flow pattern map for this condition considering a mass flow rate of 0.2 m³/s
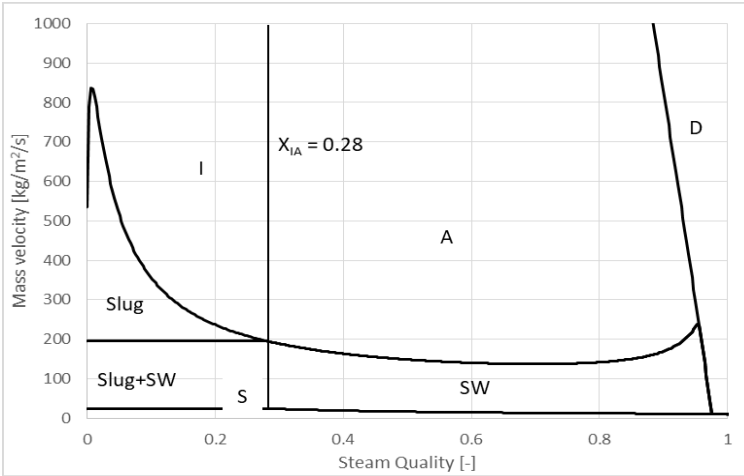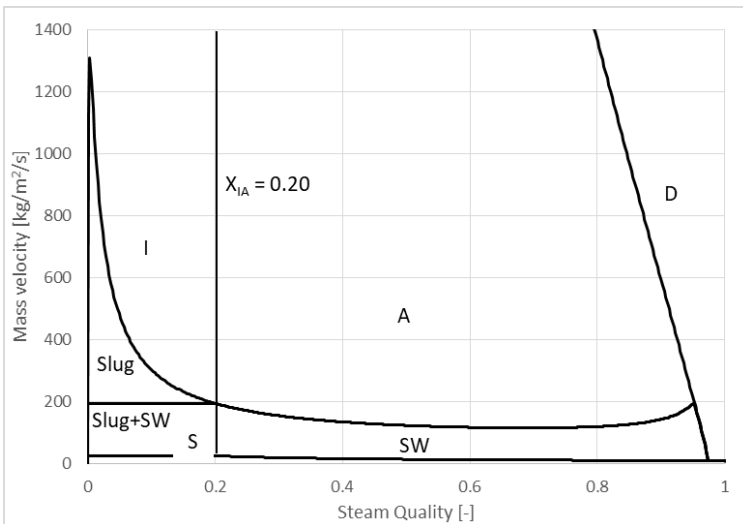

Figure 6.27- Flow pattern map for the LEPTEN LFC for 10 bar, with a volumetric flow rate of 0.2 m³/s, and a DNI of 900 W/m².

Table 6.10 and Table 6.11 shows the results for two different volumetric flow rates of 0.2 and 0.6 m³/s. As it can be seen, for this small prototype only low quality conditions are achieved.

Table 6.10- Outlet conditions the LEPTEN LFC considering saturated condition at the inlet for 10 bar and 0.2 m³/s.

Outlet Conditions	Friedel	Lockhart–Martinelli	Müller-Steinhagen and Heck	Flow Pattern Model
Quality [-]	0.04705	0.04665	0.04535	0.04412
Temperature [ºC]	177.43	177.61	178.23	178.83
Pressure [Pa]	9.44E+05	9.48E+05	9.62E+05	9.75E+05
ΔP	5.60E+04	5.20E+04	3.82E+04	2.47E+04

Table 6.11 - Outlet conditions the LEPTEN LFC considering saturated condition at the inlet for 10 bar and 0.6 m³/s.

Outlet Conditions	Friedel	Lockhart–Martinelli	Müller-Steinhagen and Heck	Flow Pattern Model
Quality [-]	0.0604	0.0597	0.0384	0.0317
Temperature [ºC]	153.99	154.33	166.97	170.74
Pressure [Pa]	5.29E+05	5.34E+05	7.35E+05	8.06E+05
ΔP [Pa]	4.71E+05	4.66E+05	2.65E+05	1.94E+05

Similarly, to the 23 bar case, for the 0.2 m³/s only slug flow is encountered on the receiver. For the 0.6 m³/s however, the flow alternates between slug and intermittent.

Afterwards a different configuration was modeled, considering a more practical application. For that, 10 modules of the LEPTEN LFC were considered mounted in series, resulting on a 120 m line of LFC. For that, the longitudinal IAM curve used was the one calculated for 120 m showed on Figure 4.6 on section 4.1.4.

The electrical preheater is an equipment with experimental use only, it has no purpose on an actual practical application. For that, unlike the previous analysis, it is left out from this one. This means that the inlet temperature on the receiver is no longer the saturation temperature of the fluid for the inlet pressure. This because there is a pressure difference between the inlet to the outlet of the receiver, due to the pressure drop. The steam separator stores a two-phase mixture at the saturation condition of the outlet pressure of the receiver. Therefore, after passing by the pump, the HTF pressure is elevated, and its condition goes to subcooled liquid.

154

This analysis considers that the inlet temperature at the most, equal to the temperature of the steam separator. This approximation, generates a maximum error of 0.4 ℃, if it considers that the actual inlet temperature would be the temperature with the thermodynamic conditions of the inlet pressure and entropy of the condensate from the steam separator. This assuming an isentropic pump. Anyhow, the difference is small, and for all analysis, the outlet temperature will be assumed equal to the inlet temperature, and that will be the convergence criteria for the models.

This configuration also means that the maximum outlet temperature will always be lower than the saturation temperature for 23 bar, since this is the maximum operational pressure for the system, and it will be used as the maximum inlet pressure for subcooled liquid.

Figure 6.28 shows the temperature profile for a case with 23 bar and 0.2 m³/s, comparing the different models, considering that the inlet temperature will be the same as the outlet temperature, which is the saturation temperature on the steam separator. It can be seen that the inlet temperature changes a maximum of 16 ℃ between models, which indicates the importance to correctly estimate the pressure drop and choose an adequate model. Since the results from the two-phase flow tests did not reproduced reliable results, further tests should be performed after the re-instrumentation of the receiver and the acquisition and installation of a new pump.
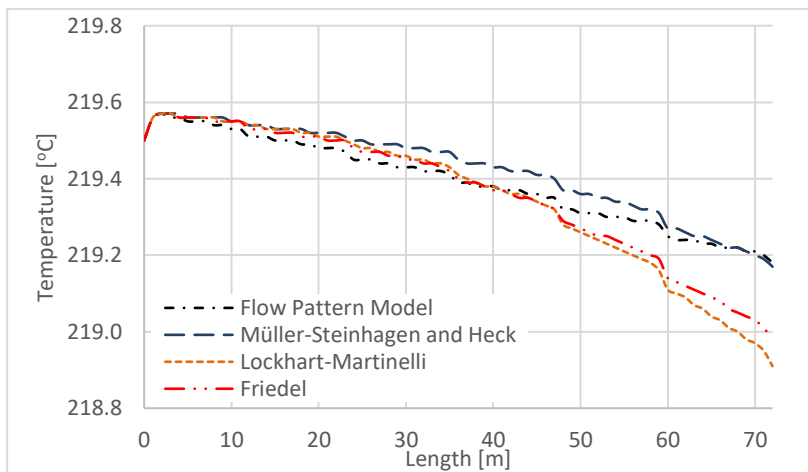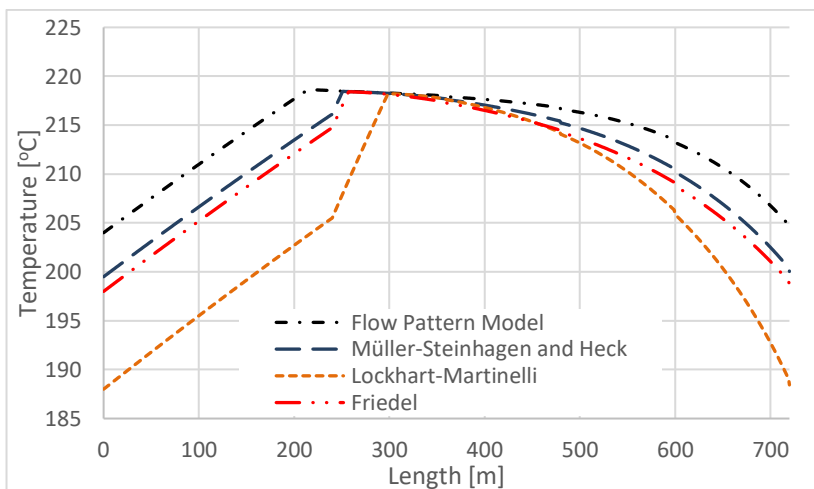

Figure 6.28 - Temperature variation along the absorber tubes calculated with different models considering 10 modules of the LEPTEN LFC for 23 bar and 0.2 m³/s.

This great difference on the temperatures is a consequence of the different pressure drop that the models presented. As showed in Figure 6.29 and Table 6.12, the maximum difference between outlet pressures is around 4.9 bar, from the flow pattern based model that gave the less pressure drop and the Lockhart-Martinelli that provided the greater.
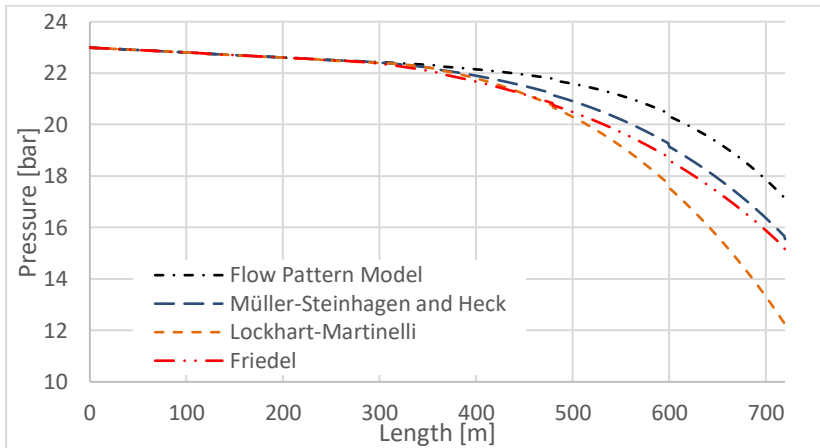
Figure 6.29- Pressure variation along the absorber tubes calculated with different models considering 10 modules of the LEPTEN LFC for 23 bar and 0.2 m³/s

Table 6.12 - Outlet conditions for 10 modules of the LEPTEN LFC for 23 bar and 0.2 m³/s.

Outlet Conditions	Friedel	Lockhart–Martinelli	Müller-Steinhagen and Heck	Flow Pattern Model
Quality [-]	0.385	0.379	0.385	0.387
Temperature [°C]	198.7	188.4	200.0	204.5
Pressure [Pa]	1.51E+06	1.21E+06	1.55E+06	1.70E+06
ΔP	7.89E+05	1.09E+06	7.45E+05	5.95E+05

The flow pattern, as well as the void fraction and quality throughout the absorber tubes can be seen on Figure 6.30. There is a distribution between slug, intermittent and annular flow, with the later happening on the last portion of the absorber tubes.

The same procedure was reproduced for a case with 23 bar and 0.6 m³/s. The temperature distribution can be seen on Figure 6.31. It can be

seen that for this higher volumetric flow rate, the temperature profile obtained by the Lockhart-Martinelli model is much closer to the ones obtained by the Friedel and Müller-Steinhagen and Heck case. Here, the flow pattern based model is giving the highest inlet temperature. Which when analyzing the Figure 6.32 and Table 6.13, is consequence of the lowest pressure drop.
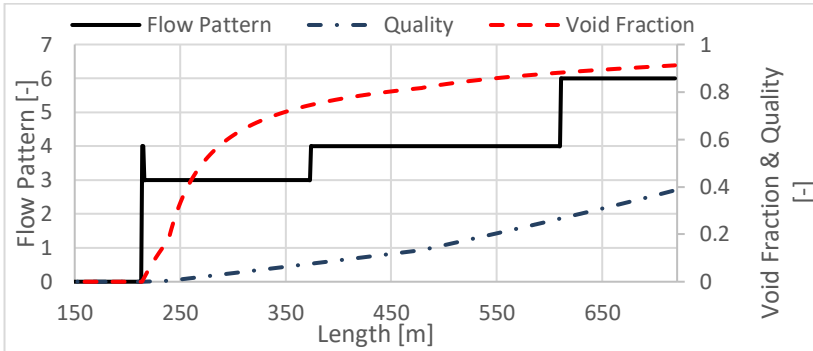
Figure 6.30– Flow pattern, steam quality and void fraction distribution considering 10 modules of the LEPTEN LFC for 23 bar and 0.2 m³/s. Flow pattern index: 0 - Single Phase; 1 – Horizontal Stratiffied; 2 - Slug+SW; 3 - Slug; 4 - Intermitent; 5 - Stratiffied Wavy; 6 - Annular; 7 - Dryout; 8 – Mist.

   In this case, the maximum inlet temperature difference obtained was of around 28 °C, and the pressure drop of around 3.4 bar, both for the flow pattern based model when comparting to the Lockhart-Martinelli.

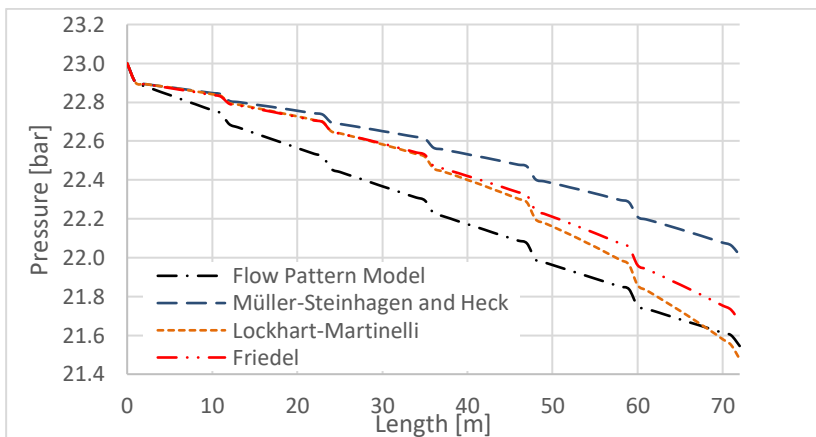Figure 6.31- Temperature variation along the absorber tubes calculated with different models considering 10 modules of the LEPTEN LFC for 23 bar and 0.6 m³/s.

Figure 6.32- Pressure variation along the absorber tubes calculated with different models considering 10 modules of the LEPTEN LFC for 23 bar and 0.6 m³/s.

Table 6.13 - Outlet conditions for 10 modules of the LEPTEN LFC for 23 bar and 0.6 m³/s.

Outlet Conditions	Friedel	Lockhart–Martinelli	Müller-Steinhagen and Heck	Flow Pattern Model
Quality [-]	0.1096	0.1056	0.1099	0.1220
Temperature [ºC]	132.1	131.26	138.73	159.81
Pressure [Pa]	2.87E+05	2.80E+05	3.48E+05	6.15E+05
ΔP	2.01E+06	2.02E+06	1.95E+06	1.69E+06

Since this case presented higher pressure drop, the inlet temperature is lower in order for the system to achieve the outlet temperature equal to the inlet. This means, as seen on Figure 6.33, that the two-phase flow starts only latter on the absorber tubes when compared to the 0.2 m³/s case. This figure also shows the evolution of the void fraction and quality of the HTF.

Figure 6.33 – Flow pattern, steam quality and void fraction distribution considering 10 modules of the LEPTEN LFC for 23 bar and 0.6m³/s. Flow pattern index: 0 - Single Phase; 1 – Horizontal Stratified; 2 - Slug+SW; 3 - Slug; 4 - Intermittent; 5 - Stratified Wavy; 6 - Annular; 7 - Dryout; 8 – Mist.

Other configuration analyzed was a case considering a demand of saturate steam at ambient pressure, around 100 °C. Similarly, as before, the outlet temperature is the same as the inlet. Figure 6.34 shows the temperature profile considering the different models, for a volumetric rate of 0.2 m³/s.

Figure 6.34- Temperature variation along the absorber tubes calculated with different models considering 10 modules of the LEPTEN LFC for 100 °C and 0.2 m³/s.

In this case, since the temperature is fixed, what changes is the inlet pressure that each pressure drop model demands in order to achieve the final condition. This can be seen on Figure 6.35 and Table 6.14.

Figure 6.35- Pressure variation along the absorber tubes calculated with different models considering 10 modules of the LEPTEN LFC 100 ºC and 0.2 m³/s

Table 6.14 - Outlet conditions for 10 modules of the LEPTEN LFC for 100 ºC and 0.2 m³/s.

	Friedel	Lockhart–Martinelli	Müller-Steinhagen and Heck	Flow Pattern Model
Quality [-]	0.345	0.347	0.344	0.357
Inlet Pressure [Pa]	1.23E+06	1.30E+06	1.24E+06	1.07E+06
ΔP [Pa]	1.13E+06	1.20E+06	1.14E+06	9.65E+05

Similarly, as the other analysis, the Lockhart-Martinelli presented the highest pressure drop, demeaning a higher initial pressure of the system. It can be seen in this and all previous analysis that the Müller-Steinhagen and Heck and the Friedel model always presented a good agreement between them. For this case, the evolution of the flow pattern, void fraction and steam quality can be seen on Figure 6.36.

Figure 6.36– Flow pattern, steam quality and void fraction distribution considering 10 modules of the LEPTEN LFC for 100 °C and 0.2 m³/s. Flow pattern index: 0 - Single Phase; 1 – Horizontal Stratified; 2 - Slug+SW; 3 - Slug; 4 - Intermittent; 5 - Stratified Wavy; 6 - Annular; 7 - Dryout; 8 – Mist.

Regardless of the model, it can be seen that for the LEPTEN LFC, the pressure drop plays an important role. Considering the 23 bar case, for the Friedel mode with 0.2 m³/s, the operational temperature stayed around 199 °C, while for 0.6 m³/s it stayed at 132 °C. Even for the lower volumetric flow rate, the operational temperature is still around 20 °C below the saturation temperature, while for higher flow rate such as 0.6 m³/s, it stayed 88 °C below.

All this shows that the six-tube configuration, with the current diameter represents to great of a pressure drop for large systems, although it works fine for a small-scale testing LFC.

For that, another configuration of receiver is analyzed. Here, the six absorber tubes of the receiver are replaced by four absorber tubes with wider diameter. The overall aperture of the absorber element, of 152.4 mm (6 x 25.4 mm) is maintained, by using four tubes with an OD of 38.1 mm (1 ½ inch).

The flow map for this configuration, considering an operational pressure of 23 bar and a volumetric flow rate of 0.2 m³/s is showed in Figure 6.37. The maps changes due to the diameter change, which results on different mass velocities on calculations.
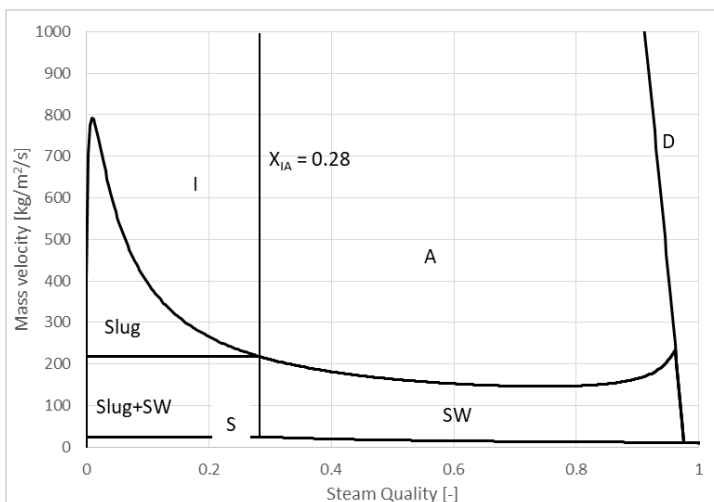
Figure 6.37- Flow pattern map for the LEPTEN LFC considering four absorber tubes of OD=38.1 mm for 23 bar, with a volumetric flow rate of 0.2 m³/s, and a DNI of 900 W/m².

In all analysis the volumetric flow rate is being used, since it is the property that is directly assessed on experiments by the flowmeter. For previous analysis the relation between volumetric flow and mass flow rate can also be seen on Table 6.15. This table also shows the different mass velocities for different diameters.

Table 6.15 - Relation of volumetric flow with mass flow rate for two different saturation conditions and relation with the mass flow velocity for two different absorber tube OD.

Saturation Temperature	≈220 [°C]			≈178 [°C]		
Pressure	23 [bar]			10 [bar]		
$\dot{v}$ [m³/s]	$\dot{m}$ [kg/s]	$G_{(Di=25.4mm)}$ [kg/m²s]	$G_{(Di=38.1mm)}$ [kg/m²s]	$\dot{m}$ [kg/s]	$G_{(Di=25.4mm)}$ [kg/m²s]	$G_{(Di=38.1mm)}$ [kg/m²s]
0.2	0.1687	406	175.3	0.178	428.1	184.9
0.4	0.3374	812	350.7	0.356	856.2	369.7
0.6	0.5061	1218	526	0.534	1284	554.6
0.8	0.6748	1624	701.3	0.711	1712	739.5
1	0.8435	2030	876.7	0.889	2140	924.3

The first condition analyzed is for 23 bar and 0.2 m³/s. The overall length of the absorber tubes is now 480 m, since it is only for tubes considered. The concentrated radiation distribution model was reevaluated for the case of four tubes. Figure 6.38 shows the temperature distribution throughout the absorber tube, considering the different models for a calculation where the output temperature is equal to the inlet.

Figure 6.38- Temperature variation along the absorber tubes calculated with different models considering 10 modules of the LEPTEN LFC with four absorber tubes of OD=38.1 mm for 23 bar and 0.2 m³/s.

Here, the maximum difference temperature between models is of 2 °C, as seen on Table 6.16. The outlet temperature for the Friedel correlation stayed around 217 °C, while for the same conditions considering the six tubes case this temperature stayed around 198.2 °C. The steam quality at the outlet also increased from 38.5 % for the six-tubes case for 39.7 %. This because the steady state temperature is higher. This new configuration is delivering more steam, at a higher temperature, and still satisfies the absorber aperture area required for satisfactorily concentrating the radiation. These advantages come from the reduced pressure drop, as seen on Figure 6.39. The pressure drop for the Friedel case is of 0.92 bar, while for the six tubes case it was 7.9 bar.
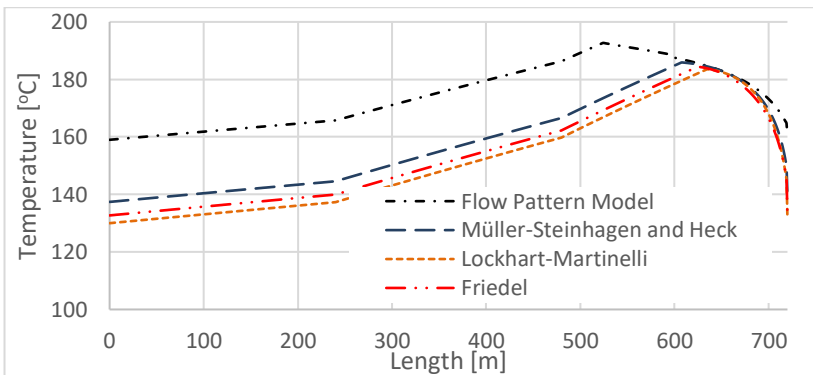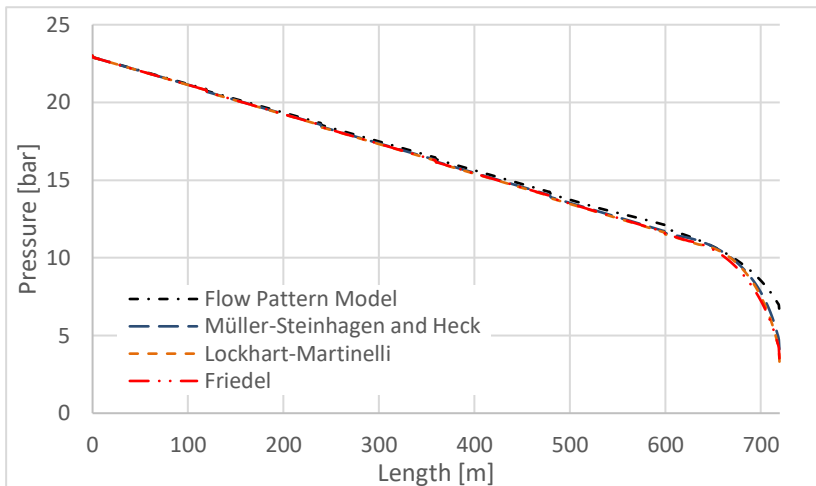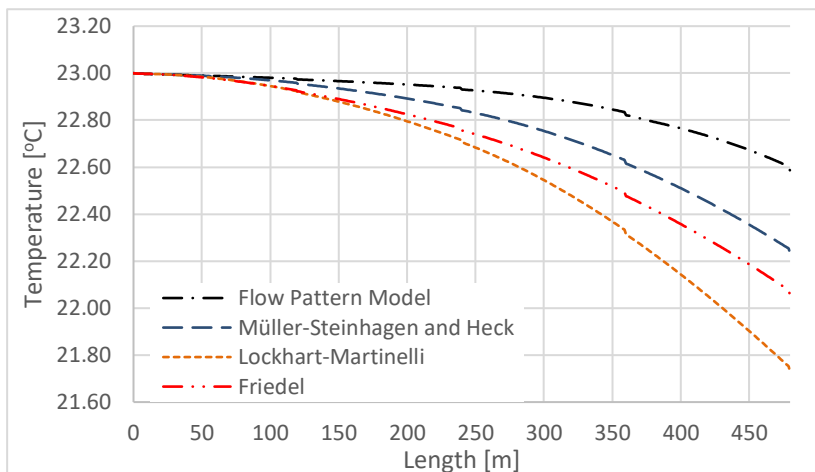
Figure 6.39- Pressure variation along the absorber tubes calculated with different models considering 10 modules of the LEPTEN LFC with four absorber tubes of OD=38.1 mm for 23 bar and 0.2 m^3/s

Table 6.16 - Outlet conditions for 10 modules of the LEPTEN LFC with four absorber tubes of OD=38.1mm for 23 bar and 0.2 m^3/s.

Outlet Conditions	Friedel	Lockhart–Martinelli	Müller-Steinhagen and Heck	Flow Pattern Model
Quality [-]	0.397	0.396	0.392	0.396
Temperature [^{o}C]	217.4	216.7	217.9	218.7
Pressure [Pa]	2.21E+06	2.17E+06	2.22E+06	2.26E+06
ΔP	9.24E+04	1.25E+05	7.47E+04	3.97E+04
Temperature [^{o}C]	217.6	216.6	216.6	218.6

Since the inlet temperature is higher and closer to the saturation, the two-phase flow starts earlier on the absorber tubes, as seen on Figure 6.40. This figure also shows the evolution of the quality and void fraction. The flow pattern slug + stratified wavy and stratified.
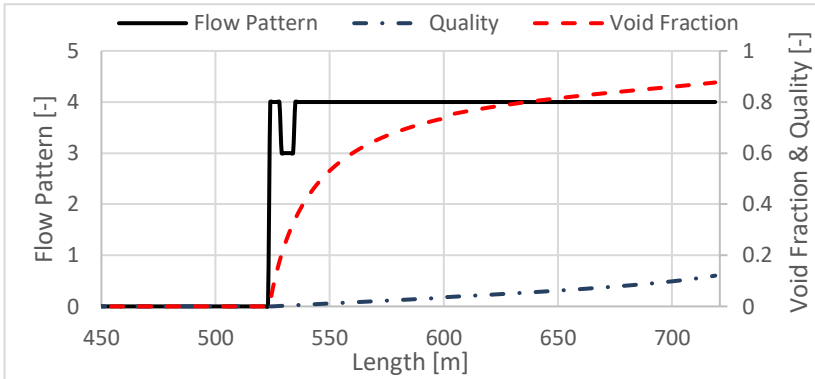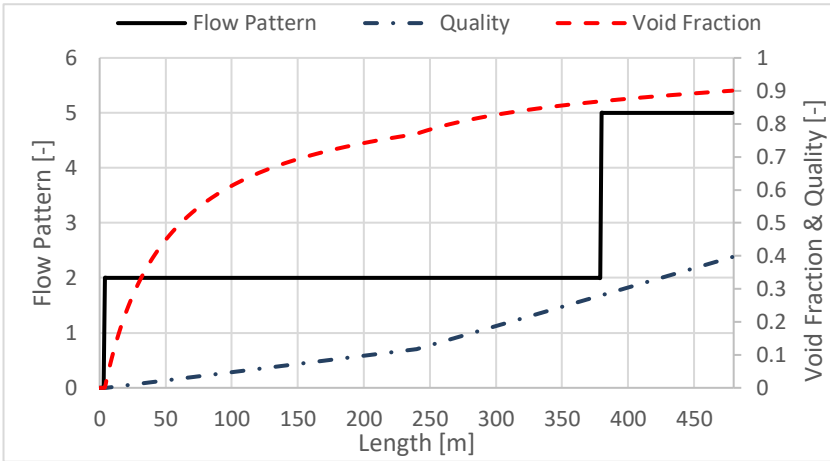
Figure 6.40 – Flow pattern, steam quality and void fraction distribution considering 10 modules of the LEPTEN LFC with four absorber tubes of OD=38.1 mm for 23 bar and 0.2 m³/s. Flow pattern index: 0 - Single Phase; 1 – Horizontal Stratified; 2 - Slug+SW; 3 - Slug; 4 - Intermittent; 5 - Stratified Wavy; 6 - Annular; 7 - Dryout; 8 – Mist.

The same analysis was performed for a volumetric flow rate of 0.6 m³/s, at the same pressure of 23 bar. Figure 6.41 shows the temperature profile througout the tube.
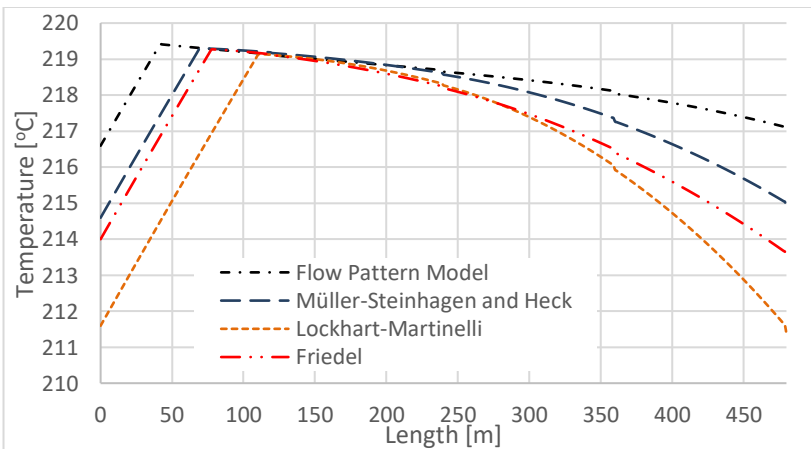
Figure 6.41- Temperature variation along the absorber tubes calculated with different models considering 10 modules of the LEPTEN LFC with four absorber tubes of OD=38.1 mm for 23 bar and 0.6 m³/s

For this case, the temperature for the Friedel correlation stayed around 213 ºC as seen on Table 6.17, which is around 80 ºC above the six-tube configuration for the same condition. As it can be seen, for higher volume flows, this difference in pressure drop becomes more evident, as can be seen on Figure 6.42.
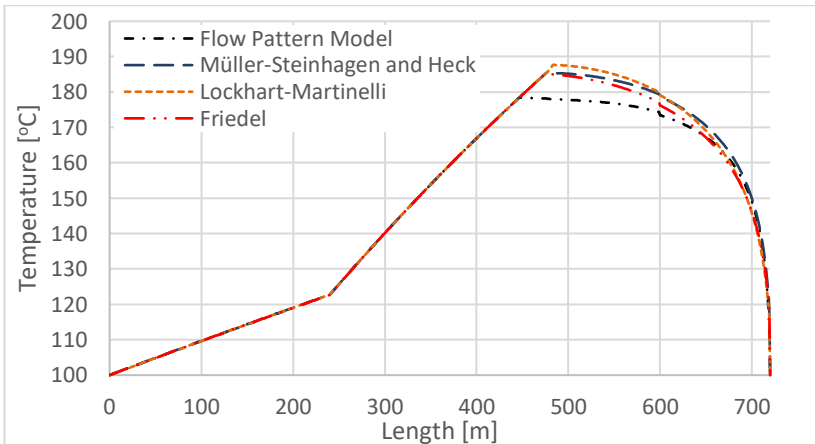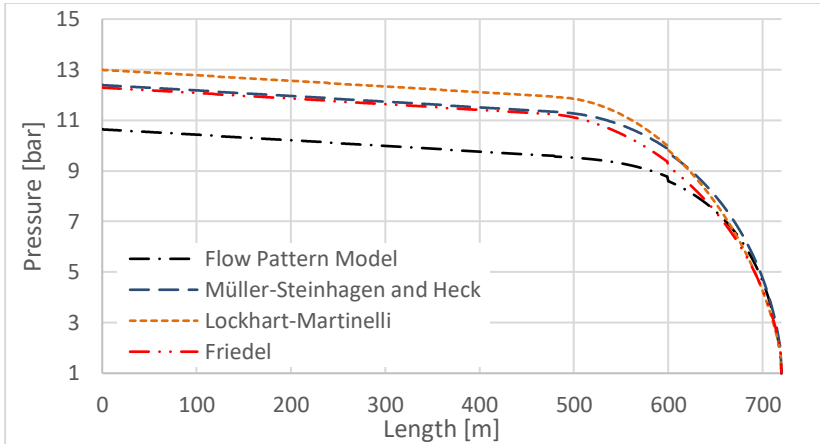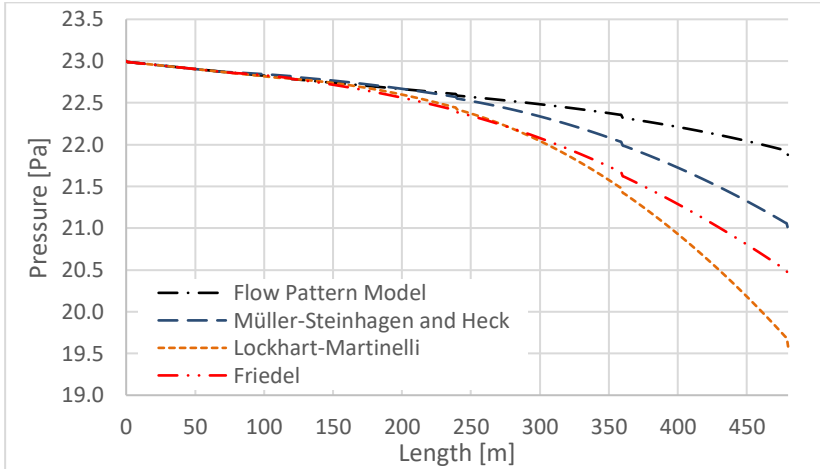

Figure 6.42- Pressure variation along the absorber tubes calculated with different models considering 10 modules of the LEPTEN LFC with four absorber tubes of OD=38.1 mm for 23 bar and 0.6 m³/s.

The pressure drop of the Friedel model drops from 20 bar to 2.5 bar when considering the four tubes case. The six tube case is already unfeasible for this flow rate, considering a line of LFC of 120 m.

Table 6.17- Outlet conditions for 10 modules of the LEPTEN LFC with four absorber tubes of OD=38.1mm for 23 bar and 0.6 m³/s.

Outlet Conditions	Friedel	Lockhart–Martinelli	Müller-Steinhagen and Heck	Flow Pattern Model
Quality [-]	0.132	0.131	0.131	0.131
Temperature [ºC]	213.6	211.6	215.0	217.1
Pressure [Pa]	2.04E+06	1.96E+06	2.10E+06	2.19E+06
ΔP	2.51E+05	3.32E+05	1.94E+05	1.07E+05

Figure 6.43 shows the evolution of void fraction, steam quality and flow pattern. For this condition, the flow pattern most encountered is the

slug flow, that changes to intermittent further on the absorber tubes. This higher flow rate makes the flow escape the undesirable condition of stratified flow. At larger lines, following the flow map of Figure 6.37, the flow would enter the annular condition.
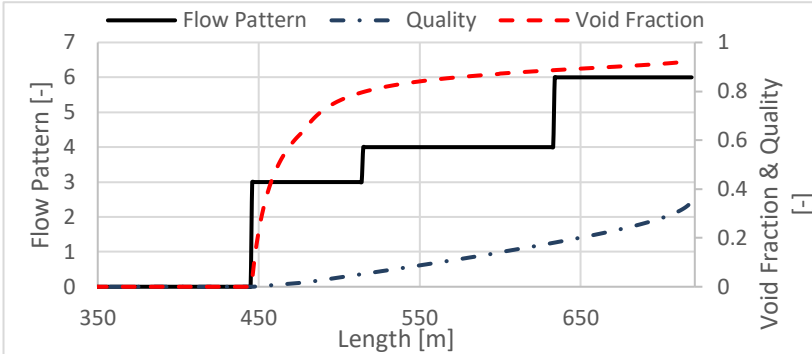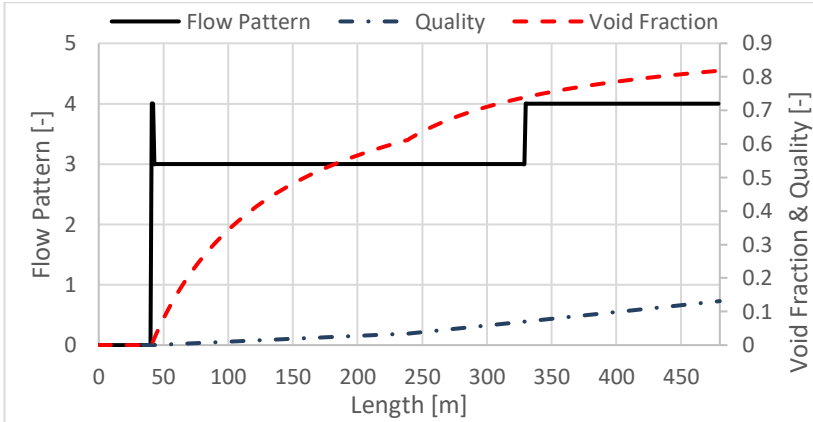

Figure 6.43 – Flow pattern, steam quality and void fraction distribution considering 10 modules of the LEPTEN LFC with four absorber tubes of OD=38.1 mm for 23 bar and 0.6 m³/s. Flow pattern index: 0 - Single Phase; 1 – Horizontal Stratified; 2 - Slug+SW; 3 - Slug; 4 - Intermittent; 5 - Stratified Wavy.

The last condition analyzed is for an even higher volumetric flow rate, of 1 m³/s. This flow rate was used in experiments with the LEPTEN LFC, however it would be unfeasible for the same configuration of LFC but longer lines. By changing to four tubes, considering the 120 m line of LFC, this situation changes a little. The temperature profile can be seen on Figure 6.44. As seen on Table 6.18 the inlet temperature for the Friedel case is around 210 °C, which is still around 78 °C higher than the six-tube case for the lower volumetric flow of 0.6 m³/s. This shows the improvement in performance that this new configuration would achieve.
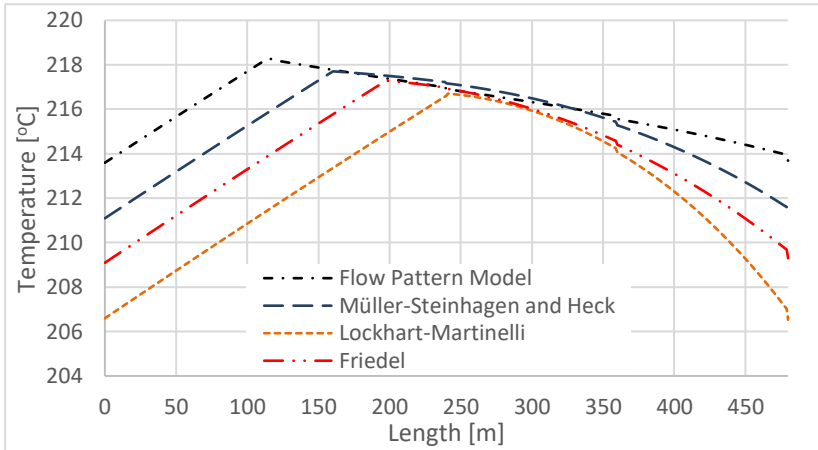
Figure 6.44- Temperature variation along the absorber tubes calculated with different models considering 10 modules of the LEPTEN LFC with four absorber tubes of OD=38.1 mm for 23 bar and 1 m³/s.

As for the pressure drop, it can be seen on Figure 6.45 and on Table 6.18 that it stayed around 4 bar for the Friedel case. It could be argued that increasing even more the tube diameter would decrease the pressure drop, however, larger diameters means thicker walls, if they are to operate at the same pressure.
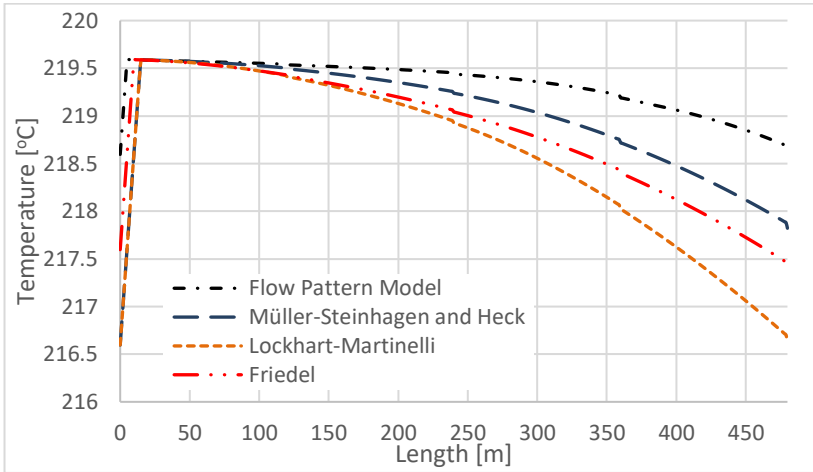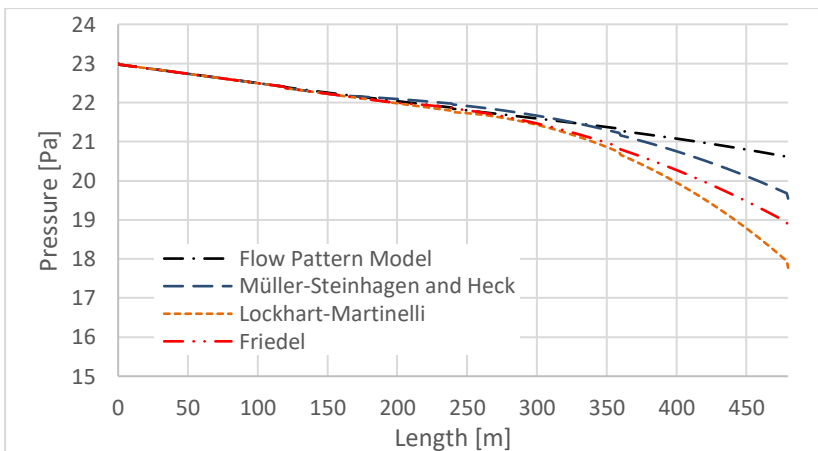

Figure 6.45- Pressure variation along the absorber tubes calculated with different models considering 10 modules of the LEPTEN LFC with four absorber tubes of OD=38.1 mm for 23 bar and 1 m³/s.

Table 6.18- Outlet conditions for 10 modules of the LEPTEN LFC with four absorber tubes of OD=38.1 mm for 23 bar and 1 m³/s.

Outlet Conditions	Friedel	Lockhart–Martinelli	Müller-Steinhagen and Heck	Flow Pattern Model
Quality [-]	0.077	0.078	0.078	0.079
Temperature [°C]	209.7	207.0	211.6	213.9
Pressure [Pa]	1.88E+06	1.78E+06	1.95E+06	2.05E+06
ΔP	4.06E+05	5.05E+05	3.32E+05	2.39E+05

This increase in wall thickness is not very appreciable when changing from six to four tubes case, considering that they will operate at the same pressure. All these cases considered the same heat losses obtained experimentally for the LEPTEN LFC. On the four tubes, the heat losses would probably be slightly higher due to this wall thickness increase.

Figure 6.46 shows that for this higher flow rate the flow pattern varies between slug and intermittent.
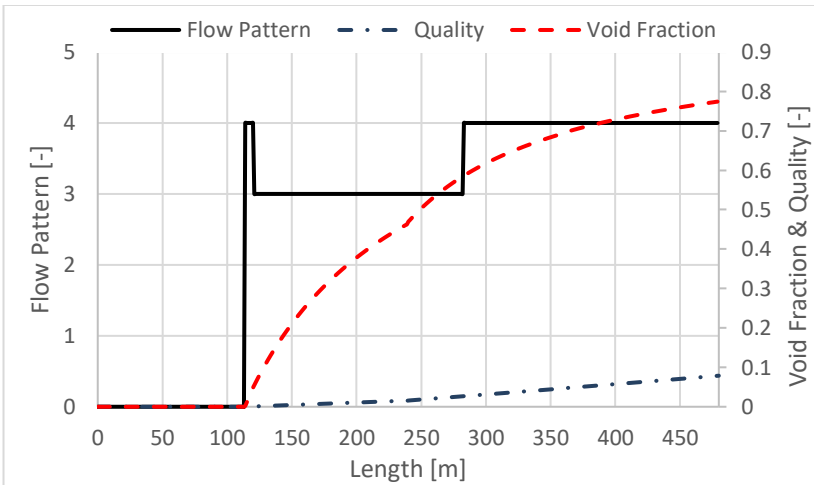
Figure 6.46 – Flow pattern, steam quality and void fraction distribution considering 10 modules of the LEPTEN LFC with four absorber tubes of OD=38.1mm for 23 bar and 1 m³/s. Flow pattern index: 0 - Single Phase; 1 – Horizontal Stratified; 2 - Slug+SW; 3 - Slug; 4 - Intermittent; 5 - Stratified Wavy.

It can be said that although for a small scale LFC, the receiver from the LEPTEN LFC has a satisfactory performance, it is not adequate for longer

lines of LFC. For that, the four-tube configuration presented a much better performance.

6.3   Partial Conclusions

The model presented in Chapter 5 was used to analyze the two LFC benches. For the one of SunCNIM, a longer line, of industrial proportions, was studied. It was verified that for all operational conditions, most of the length of the tube is covered with annular and slug flow. For the flow rate analyzed there was no stratified flow.

It was possible to verify the influence of some parameters on the flow pattern. Higher operational pressures tend to hold the single phase condition longer, and it presented a shorter length of annular flow that is preferable for DSG. Higher DNI increased the length of annular flow on the absorber tube.

Another aspect that influenced on the flow pattern is the geometry of the tube. By reducing the inner diameter, the annular flow was encountered for almost 60% of the tube on 3 MPa cases, and almost half of the tube on 5 MPa cases. It was also verified that for low DNI values the reduction on the diameter does not affect the flow pattern, due to the associated low mass flow rate. For these cases the annular flow rate is not reached.

For the LEPTEN LFC, two sets of experimental tests were compared with the model developed. First is the single-phase flow experiments. These tests served to validate the model for single-phase flow, and to study the behavior of the workbench in more controlled conditions than the ones found on two-phase flow tests.

It was seen the roughness of the tube has an impact on the pressure drop, especially since the LFC counts with welded connections and incrustations. This is evidenced by the results of the Colebrook and Blasius correlations when applied to the LFC. Measured values of pressure drop were around 50 % higher than the ones found with the Blasius correlation, and the difference between measurements and the Colebrook correlation was only around -0.49 %.

The non-uniform concentrated radiation model also presented a better fit with experimental data, although the error difference reduced only from 2.3 % to 1.3 %. This model, however, better represents the development of the temperature profile throughout the tube.

The Colebrook correlation with the non-uniform concentrated radiation model is used on the two-phase flow analysis.

When analyzing the set of data, it appears that the mass flow rate and temperature influence the pressure drop error. For higher temperatures, and lower mass flow rate, the pressure drop errors are higher.

These errors can be related to the volumetric flow rate measured. Other factors that are not included on the model and may cause the difference in pressure drop are leakage on the connections, tubes not completely filled with liquid and steam accumulation on the flexible hoses. It is noteworthy that the higher temperature coincides with the lower mass flow rate tests. The pressure drop is also smaller for lower mass flow rate. This makes these tests more sensible to errors. Even smaller variations on the output pressure can generate high errors.

After analyzing the experimental data, the model was used to study three hypothetical cases. The first two used the LEPTEN LFC geometry as it is and were presented to show that the current receiver with six tubes is unpractical for larger solar fields.

The first case considered as if the experimental equipment were enough to deliver the water at saturated condition at the inlet of the receiver. For that, it was seen that for 23 bar and 0.2 m^3/s it was achieved a quality of around 0.04 at the outlet, with temperatures around 220 ℃. For 10 bar and 0.2 m^3/s the quality found at the outlet was around 0.05 at temperatures around 177 ℃.

Later ten modules of the LEPTEN LFC were modeled in line. This showed that the longer line of LFC is unpractical. Considering the same inlet and outlet temperature for operation, for 23 bar and 0.2 m^3/s, the difference in temperature between models reached maximum of 16 ℃ which indicates the importance to correctly estimate the pressure drop and choose an adequate model. To do so, further instrumentation is required.

Generally, the flow pattern based model presented the lower pressure drop, followed by Müller-Steinhagen and Heck then the Friedel correlation, and the highest pressure drop was found for the Lockhart–Martinelli correlation. Regardless of the model, it can be seen that for the LEPTEN LFC, the pressure drop plays an important role. Even for the lower volumetric flow rate, the operational temperature stayed around 20 ℃ below the saturation temperature at the inlet. For 0.6 m^3/s, this temperature difference reached 88 ℃.

This evidences that the six-tube configuration, with the current diameter, presents unpractical pressure drops for larger systems. Therefore, another configuration of receiver was analyzed, considering four tubes instead of six. The diameter of the four tubes was dimensioned to give an aperture area equal to the six tubes. The comparison for 23 bar and 0.2

m^3/s showed a pressure drop for the Friedel correlation of 0.92 bar, while for the six-tube case it was 7.9 bar.

Although for a small scale LFC such as the LEPTEN LFC the six-tube receiver has a satisfactory performance, it is not adequate for larger systems. For that, the four-tube configuration presented a much feasible performance.

7 CONCLUSIONS AND SUGGESTIONS FOR FUTURE WORKS

In this Chapter, the main conclusions regarding the analysis of the two linear Fresnel collector, LFC, prototypes are presented, and suggestions for future work are given. These two LFCs are a small experimental setup, built at LEPTEN/UFSC, and a commercial one from the French Sun CNIM company.

7.1 Conclusions

The relatively new operational strategy called Direct Steam Generation, DSG, appears to have a promising future due to its advantages such as the possibility of performance improvement and cost reductions. Several works have already been performed on this subject, with the DISS facility (ZARZA et al., 2004) as the major milestone. However, the two-phase flow inside the solar field adds some complexities, and so does the higher temperature and pressures, therefore further studies must be performed to better understand the DSG process. Studies on the DISS facility have proven the feasibility of the DSG with parabolic trough collector, PTC, however, it was seen that LFC have a great potential to operate under DSG.

In addition, experiments from the DISS were used to verify two-phase flow models on evacuated absorbers (AGUILAR-GASTELUM et al., 2014; ECK; HIRSCH, 2007; MOYA; VALENZUELA; ZARZA, 2011; XU; WIESNER, 2015), and different operational control strategies (VALENZUELA et al., 2005, 2006). The most reliable and stable operational mode experimentally found was the recirculation (ECK et al., 2003; ZARZA et al., 2004). This operational mode is used on both LFC benches studied on this work.

The model developed used a detailed literature review as base. Many models can be found in literature, and they use several correlations to analyze the two-phase flow on DSG. Perhaps the most recurrent is the Friedel correlation, which according to Pye et al. (PYE; MORRISON; BEHNIA, 2007) presents the best fit with the DISS data. The thermal part of the models found approach the thermal losses differently, with some using a semi-analytical analysis (ODEH; MORRISON; BEHNIA, 1998; RUSSELL, 2003; YAN et al., 2010), while some consider an empirical heat loss curve found experimentally (ECK; STEINMANN, 2005; FRAIDENRAICH et al., 2013; ROLDÁN; VALENZUELA; ZARZA,

2013). The present work used the later method, using experimental data to find the heat loss curves.

The present study proposed a methodology to evaluate new LFC, obtaining aspects such as the geometric characterization; the optical characterization using experimental data; the heat loss evaluation using experimental data; a thermo-hydraulic two-phase flow model for the heat transfer fluid and a comparison between model results with experiment and analysis of the results.

The thermo-hydraulic model used for analyzing the two LFC prototypes was adjusted accordingly to each LFC. The LEPTEN model also included the non-uniform concentrated radiation distribution between the six absorber tubes, which presented good agreement with experimental temperature distribution throughout the tubes.

The pressure drop was modeled for both single and two-phase flows. The Fanning equation was used for single-phase pressure drop, with the Blasius and the Colebrook-White friction factors used for comparison. The latter was developed for industrial piping, taking into account the surface roughness.

The two-phase pressure drop used different models: homogeneous; Lockhart and Martinelli; Friedel; Müller-Steinhagen and Heck; and a pattern-based correlation. The pattern-based correlation is a phenomenological model proposed by Quibén and Thome (MORENO QUIBÉN; THOME, 2007b, 2007a). This correlation used the diabatic flow map developed by Wojtan, Ursenbacher and Thome (WOJTAN; URSENBACHER; THOME, 2005a, 2005b).

The correlations were verified with experimental data from the DISS facility, allowing comparison with other works from literature. It was seen that the phenomenological model did not responded particularly well for the low-pressure cases, underestimating the pressure drop. The models that presented the best fit to all experimental data was the Friedel and the Muller-Steinhagen and Heck. For higher pressures the flow pattern-based model also presented reliable results. This model includes phenomenological considerations of the flow pattern inside the absorber tube. The flow pattern model presented a maximum RMSE of 1.4 % for all cases, and 0.3 % for the higher-pressure level cases.

The flow-pattern based model also indicates the flow pattern inside the absorber tube. This model was compared with a numerical work (MOYA; VALENZUELA; ZARZA, 2011), that simulated the two-phase flow in RELAP, in order to verify if it is predicting reasonably well the flow pattern. Both models presented similar results. The annular region occupies almost the same region inside the tube for both models. The

main difference is on the beginning of the two-phase region, where RE-LAP showed regions of bubbly, stratified and slug flow, and the model used in this work showed only slug flow.

Overall, the pressure drop model presented good agreement with the experimental data from DISS presented by (LOBÓN et al., 2014). Specific conclusions regarding each of the LFC benches are presented on the next sections.

7.1.1   SunCNIM LFC

One of the LFC prototypes analyzed on this work was the SunCNIM workbench, located at La Seyne-sur-Mer, in south France. It is an LFC of industrial proportions, already in operation for several years. For this case, the heat loss curve was given by SunCNIM. The IAM curves used on analysis were obtained using SolTrace, therefore, the parametrical evaluation of the SunCNIM LFC served only to obtain the optical peak efficiency. These parameters were used on the thermo-hydraulic analysis.

The thermo-hydraulic model was used considering a longer line of LFC, using modules of the SunCNIM LFC. For all operational conditions it was found that most of the absorber tube was under either annular flow or slug flow. No stratified flow was encountered.

Parameters were varied in order to evaluate their influence on the flow pattern. Higher operational pressures ensured the single-phase condition longer, and it presented a shorter length of annular flow. Higher values of DNI increased the length of annular flow on the absorber tube. Annular flow is a desirable condition since it ensures a wetting of all internal wall of the absorber tube, reducing thermal stresses and improving the heat transfer.

The geometry of the tube also plays an important role on the flow pattern. A reduction on of 20 % on the inner diameter showed annular flow for almost 60 % of the tube on 3 MPa cases, and almost half of the tube on 5 MPa cases.

The thermal benefits of the diameter reduction come associated with a mean increase in pressure drop of about 3.5 % on the lower pressure level, which may be considered acceptable.

A great issue regarding the reduction of the diameter is associated with the optical design of the collector, especially the secondary reflector design. For that, one option would to increase the height of the receiver and change the design of the secondary reflector. These changes may be the main limiting factor on this design change of the tube diameter.

7.1.2   LEPTEN LFC

The other LFC studied is the LEPTEN workbench, installed at the Federal University of Santa Catarina, south Brazil. It represents a small scale LFC prototype, able to supply steam for industry, however at lower temperatures as the ones from SunCNIM.

For this case, the parameter characterization was used to obtain the peak efficiency and the heat losses experimental curve. The IAM curves were initially obtained using SolTrace, however, the longitudinal IAM showed discrepancies with experimental data. For that, further experiments were performed with the intent to verify the calculated IAM comparing with an experimental one. As a result of this analysis, the longitudinal IAM for the LEPTEN found with SolTrace was adjusted with experimental data. The transversal IAM obtained by SolTrace presented satisfactory results.

The procedures for parameter characterization showed a satisfactory performance in identifying these main parameters of an LFC.

The moving absorber design was also analyzed in Appendix D. The mean end losses, considering the movement due to south for periods when the maximum displacement cannot fully compensate the incidence angle is of 4 %. For a fixed absorber this value reaches 35 %. The analysis showed that the moving absorber present great advantage for small scale prototypes, and that it is not viable for large scale LFC.

As regarding the thermo-hydraulic analysis, two sets of experimental tests were used. First there was the single-phase experiments, which were used to validate the model for single-phase flow, and to study the behavior of the workbench in more controlled conditions than the ones found on two-phase flow tests.

It was seen that the roughness of the tube has impact on the pressure drop. Results of the Colebrook correlation presented a difference from measurements of around -0.5 %; while for the Blasius correlation measured values of pressure drop were around 50 % higher than the ones found. The non-uniform concentrated radiation model also presented a best fit with experimental data, better representing the development of the temperature profile throughout the tube. The Colebrook correlation with the non-uniform concentrated radiation model was used on the two-phase flow analysis.

When comparing the two-phase flow experimental data with the model, it appears that the mass flow rate and temperature influence the pressure drop error. The pressure drop errors are higher for higher tem-

peratures, and lower mass flow rate. There are some aspects that can justify these errors, such as errors on the volumetric flow rate measured, leakage on the connections, tubes not completely filled with liquid and steam accumulation on the flexible hoses. The errors for some tests reached a value of around 80 %.

It is important to have in mind that the higher temperature tests coincide with the lower mass flow rate tests. The pressure drop is smaller for lower mass flow rate, which makes these tests more sensible to errors.

For the cases analyzed, the flow pattern based model presented the lower pressure drop, followed by Müller-Steinhagen and Heck then the Friedel correlation, and the highest pressure drop was found for the Lockhart–Martinelli correlation.

The model was later used to study three hypothetical cases. First it was considered as if the experimental equipment were enough to deliver the water at saturated condition at the inlet of the receiver. Later 10 modules of the LEPTEN LFC were modeled in line. Even for the lower volumetric flow rate, the operational temperature stayed around 20 °C below the saturation temperature at the inlet, indicating a large pressure drop. For 0.6 m³/s, this temperature difference reached 88 °C. It could be seen that for the LEPTEN LFC, the pressure drop plays an important role, making it unpractical to use this design for larger lines.

Therefore, another configuration of receiver was analyzed, considering four tubes instead of six. The comparison for 23 bar and 0.2m³/s showed a pressure drop for the Friedel correlation of 0.92 bar, while for the six-tube case it was 7.9 bar.

Although for a small scale LFC such as the LEPTEN LFC the six-tube receiver has a satisfactory performance, it is not adequate for larger systems. For that, the four-tube configuration presented a much feasible performance.

7.2   Suggestions for future work

Some steps seen in the work of (DUDLEY et al., 1994) could be used to improve the experimental analysis of both LFC. The optical efficiency of the LFC could be evaluated with zero incident angle (or the closest possible), while it operates with low temperature of the HTF. This was performed for the LEPTEN LFC, however more tests could be done on the next summer to improve this analysis. The same low temperature procedure could be used to analyze other incidence angle points, in order to verify the calculated IAM curve validity. It was also performed for the LEPTEN LFC; however, a larger set of data would increase the reliability

of the work. With these parameters well established, the SunCNIM plant could be studied operating in nominal conditions, in order to evaluate the thermal losses, as it was done for the LEPTEN LFC.

The heat loss coefficients, as a function of the HTF temperature and the ambient temperature, were provided by SunCNIM. The same is obtained for the LEPTEN LFC. Future analysis could include a heat loss model. It could also include the inner wall wetting effect due to the flow pattern encountered throughout the tube, as well as the non-concentrated radiation profile on the outer wall of the absorber tube.

Some specific suggestions for the LEPTEN LFC follows:

- Improvement of the receiver instrumentation, with further temperature measurements and pressure measurement throughout the tubes.

- Achieve a better fixation of the thermocouples on the outer surface of the tubes.

- Make a heat loss model to compare with experimental data, and for that use the external wall thermocouples.

- Exchange the six absorber tubes of 25.4 mm of external diameter for four tubes of 38.1mm of external diameter.

- Exchange some auxiliary equipment such as the pump, that are limiting the full operation of the workbench.

- Improve the fixation of the flexible hoses, to ensure that they are at the horizontal position even when the receiver moves.

- Study higher temperature two-phase flow with the future new equipment installed.

- Study different flow configurations on the multi-tube receiver.

- Change the insulating glass for a clearer one, with less reflection, and test later for the longitudinal IAM curve to verify the assumptions made on this work.

The LEPTEN LFC is a sophisticated workbench, that can lead to several future works. It must be continuously improved and used to study the DSG process. It is expected that this work is just one of many that has and will still surge from this experimental bench.

REFERENCES

AGUILAR-GASTELUM, F. et al. Theoretical study of direct steam generation in two parallel pipes. **Energy Procedia**, v. 57, p. 2265–2274, 2014.

ALGUACIL, M. et al. Direct steam generation in parabolic trough collectors. **Energy Procedia**, v. 49, p. 21–29, 2013.

AUROUSSEAU, A.; VUILLERME, V.; BEZIAN, J.-J. Control systems for direct steam generation in linear concentrating solar power plants – A review. **Renewable and Sustainable Energy Reviews**, v. 56, p. 611–630, 1 abr. 2016.

BARLEV, D.; VIDU, R.; STROEVE, P. Innovation in concentrated solar power. **Solar Energy Materials and Solar Cells**, v. 95, n. 10, p. 2703–2725, 2011.

BARR, D.; WHITE, C. Technical note. Solutions of the Colebrook-White function for resistance to uniform turbulent flow. **Proceedings of the Institution of Civil Engineers**, v. 71, n. 2, p. 529–535, 17 jun. 1981.

BAYÓN, R. et al. Analysis of the experimental behaviour of a 100 kWth latent heat storage system for direct steam generation in solar thermal power plants. **Applied Thermal Engineering**, v. 30, n. 17–18, p. 2643–2651, 1 dez. 2010.

BIENCINTO, M.; GONZÁLEZ, L.; VALENZUELA, L. A quasi-dynamic simulation model for direct steam generation in parabolic troughs using TRNSYS. **Applied Energy**, v. 161, p. 133–142, 2016.

BIRNBAUM, J. et al. Steam temperature stability in a direct steam generation solar power plant. **Solar Energy**, v. 85, n. 4, p. 660–668, 2011.

BITTENCOURT, A. et al. **Geometrical Parametric Analysis to Find Optimum Configuration of a Solar Concentrator Workbench Using Linear Fresnel Technology**. Solar World Congress 2015 Conference Proceedings. **Anais**...2015

BROGNI, P. M. et al. **Conception and evaluation of a tracking system for a linear Fresnel concentrator**. Procceedings of the 24th ABCM International Congress of Mechanical Engineering. **Anais**...ABCM, 2017

BURIGO, A. et al. **Geometric design and optimization of a linear Fresnel solar collector**. 23rd ABCM International Congress of Mechanical Engineering. **Anais**...Rio de Janeiro: 2015Available in: <http://www.swge.inf.br/proceedings/paper/?P=COB-2015-0665>. Accessed in: 20 jun. 2018

CAREY, V. Liquid vapor phase change phenomena: an introduction to the thermophysics of vaporization and condensation processes in heat transfer equipment. 2018.

CHISHOLM, D. A theoretical basis for the Lockhart-Martinelli correlation for two-phase flow. **International Journal of Heat and Mass Transfer**, v.

10, n. 12, p. 1767–1778, 1 dez. 1967.

CHISHOLM, D. Two-Phase Flow in Bends. **Int J Multiphase Flow**, v. 6, n. 4, p. 363–367, 1980.

DE SÁ, A. B. Procedimento para modelagem de uma planta termossolar utilizando a tecnologia de coletores cilindro parabólicos. 2013.

DE SÁ, A. B. et al. Direct steam generation in linear solar concentration: Experimental and modeling investigation – A review. **Renewable and Sustainable Energy Reviews**, v. 90, p. 910–936, 1 jul. 2018.

DELATORRE, J. et al. Monte Carlo advances and concentrated solar applications. **Solar Energy**, v. 103, p. 653–681, 1 maio 2014.

DESIDERI, U. et al. Comparative analysis of concentrating solar power and photovoltaic technologies: Technical and environmental evaluations. **Applied Energy**, v. 102, p. 765–784, 1 fev. 2013.

DUDLEY, V. E. et al. **Test results: SEGS LS-2 solar collector**, 1 dez. 1994. Available in: <https://www.osti.gov/scitech/biblio/70756>. Accessed in: 9 nov. 2017

DUFFIE, J. A.; BECKMAN, W. A.; WOREK, W. M. **Solar Engineering of Thermal Processes, 4nd ed.** [s.l: s.n.]. v. 116

ECK, M. et al. Applied research concerning the direct steam generation in parabolic troughs. **Solar Energy**, v. 74, n. 4, p. 341–351, 2003.

ECK, M. et al. Field Test of Water-Steam Separators for Direct Steam Generation in Parabolic Troughs. **Journal of Solar Energy Engineering**, v. 130, n. 1, p. 011002, 2008.

ECK, M. et al. Direct steam generation in parabolic troughs at 500°C – First results of the REAL-DISS project. **17th SolarPACES conference, 20-23 Sep, 2011, Granada**, n. April 2016, p. 1–10, 2011.

ECK, M.; HIRSCH, T. Dynamics and control of parabolic trough collector loops with direct steam generation. **Solar Energy**, v. 81, n. 2, p. 268–279, 2007.

ECK, M.; STEINMANN, W. Modeling and design of direct solar steam generating collector fields. **ASME 2004**, 2004.

ECK, M.; STEINMANN, W. D. Modelling and design of direct solar steam generating collector fields. **Journal of Solar Energy Engineering-Transactions of the Asme**, v. 127, n. 3, p. 371–380, 2005.

ECK, M.; STEINMANN, W. D.; RHEINLÄNDER, J. Maximum temperature difference in horizontal and tilted absorber pipes with direct steam generation. **Energy**, v. 29, n. 5–6, p. 665–676, 2004.

ELSAFI, A. M. On thermo-hydraulic modeling of direct steam generation. **Solar Energy**, v. 120, p. 636–650, 2015.

ENGINEERING TOOLBOX. **Equivalent Length Method - Calculating Minor Pressure Loss in Piping Systems**. Available in: <https://www.engineeringtoolbox.com/equivalent-pipe-length-method-d_804.html>. Accessed in: 5 jun. 2018.

FERNÁNDEZ-GARCÍA, A. et al. Parabolic-trough solar collectors and their applications. **Renewable and Sustainable Energy Reviews**, v. 14, n. 7, p. 1695–1721, 2010.

FILHO, V. C. P. et al. Experimental and Numerical Analysis of Thermal Losses of a Parabolic Trough Solar Collector. **Energy Procedia**, v. 57, p. 381–390, 1 jan. 2014.

FILIP, A.; BĂLTĂREȚU, F.; RADU-MIRCEA, D. Comparison of two-phase pressure drop models for condensing flows in horizontal tubes. **Mathematical Modelling in Civil Engineering**, v. 10, n. 4, 2014.

FRAIDENRAICH, N. et al. Analytical modeling of direct steam generation solar power plants. **Solar Energy**, v. 98, n. PC, p. 511–522, 2013.

FRIEDEL, L. Improved friction pressure drop correlations for horizontal and vertical two-phase pipe flow. **European two-phase group meeting, Ispra, Italy**, 1979.

GIOSTRI, A. et al. Comparison of Two Linear Collectors in Solar Thermal Plants: Parabolic Trough Versus Fresnel. **Journal of Solar Energy Engineering**, v. 135, n. 1, p. 011001, 22 jun. 2012.

HEIMSATH, A. et al. Quantifying Optical Loss Factors of Small Linear Concentrating Collectors for Process Heat Application. **Energy Procedia**, v. 48, p. 77–86, 1 jan. 2014.

HERTEL, J. D.; MARTINEZ-MOLL, V.; PUJOL-NADAL, R. Estimation of the influence of different incidence angle modifier models on the biaxial factorization approach. **Energy Conversion and Management**, v. 106, p. 249–259, 1 dez. 2015.

HIRSCH, T.; STEINMANN, W.; ECK, M. Simulation of transient two-phase flow in parabolic trough collectors using Modelica. **Proceedings of the 4th International Modelica Conference**, p. 1–11, 2005.

HOFFMANN, A. et al. Simulation of thermal fluid dynamics in parabolic trough receiver tubes with direct steam generation using the computer code ATHLET. **Kerntechnik**, 2014.

HORTA, P.; OSÓRIO, T. Optical Characterization Parameters for Line-focusing Solar Concentrators: Measurement Procedures and Extended Simulation Results. **Energy Procedia**, v. 49, p. 98–108, 1 jan. 2014.

LIPPKE, F. Direct steam generation in parabolic trough solar power plants: Numerical investigation of the transients and the control of a once-through system. **Journal of Solar Energy Engineering-Transactions of the Asme**, v. 118, n. 1, p. 9–14, 1996.

LOBÓN, D. H. et al. Modeling direct steam generation in solar collectors with multiphase CFD. **Applied Energy**, v. 113, p. 1338–1348, 2014.

LOBÓN, D. H.; VALENZUELA, L. Impact of pressure losses in small-sized parabolic-trough collectors fordirect steam generation. **Energy**, v. 61, p. 502–512, 2013.

LOCKHART, R.; MARTINELLI, R. Proposed correlation of data for

isothermal two-phase, two-component flow in pipes. **Chem. Eng. Prog**, 1949.

LU, J. et al. Nonuniform heat transfer model and performance of parabolic trough solar receiver. **Energy**, v. 59, p. 666–675, 2013.

LUQUE, A.; HEGEDUS, S. **Handbook of Photovoltaic Science and Engineering Handbook of Photovoltaic Science and Engineering**. [s.l.] Wiley, 2011.

MAY, E. K.; MURPHY, L. M. Performance Benefits of the Direct Generation of Steam in Line-Focus Solar Collectors. **Journal of Solar Energy Engineering**, v. 105, n. 2, p. 126, 1983.

MCINTIRE, W. R. Factored approximations for biaxial incident angle modifiers. **Solar Energy**, v. 29, n. 4, p. 315–322, 1 jan. 1982.

MONTES, M. J.; ABÁNADES, A.; MARTÍNEZ-VAL, J. M. Thermofluidynamic Model and Comparative Analysis of Parabolic Trough Collectors Using Oil, Water/Steam, or Molten Salt as Heat Transfer Fluids. **Journal of Solar Energy Engineering**, v. 132, n. 2, p. 021001, 2010.

MORENO QUIBÉN, J.; THOME, J. R. Flow pattern based two-phase frictional pressure drop model for horizontal tubes, Part II: New phenomenological model. **International Journal of Heat and Fluid Flow**, v. 28, n. 5, p. 1060–1072, 1 out. 2007a.

MORENO QUIBÉN, J.; THOME, J. R. Flow pattern based two-phase frictional pressure drop model for horizontal tubes. Part I: Diabatic and adiabatic experimental study. **International Journal of Heat and Fluid Flow**, v. 28, n. 5, p. 1049–1059, 1 out. 2007b.

MORIN, G. et al. Comparison of Linear Fresnel and Parabolic Trough Collector power plants. **Solar Energy**, v. 86, n. 1, p. 1–12, 2012.

MOYA, S. L.; VALENZUELA, L.; ZARZA, E. Numerical Study of the Thermal-Hydraulic Behavior of Water-Steam Flow in the Absorber Tube of the Diss System Using Relap. **SolarPACES**, p. 1–2, 2011.

MÜLLER-STEINHAGEN, H.; HECK, K. A simple friction pressure drop correlation for two-phase flow in pipes. **Chemical Engineering and Processing: Process Intensification**, v. 20, n. 6, p. 297–308, 1 nov. 1986.

MÜLLER-STEINHAGEN, H.; TRIEB, F.; TRIEB, F. Concentrating solar power: A review of the technology. **Ingenia Online**, p. 1–9, 2004.

MUÑOZ-ANTÓN, J. et al. Going further with Fresnel receiver: new design window for direct steam generation. **Energy Procedia**, 2014.

NATIONAL RENEWABLE ENERGY LABORATORY. **MIDC: Solar Position Algorithm (SPA) Calculator**. Available in: <https://midcdmz.nrel.gov/solpos/spa.html>. Accessed in: 28 jun. 2018.

NEUTRIUM. Pressure Loss from Fittings – Equivalent Length Method. **Fluid flow**, 2012.

ODEH, S. D.; MORRISON, G. L.; BEHNIA, M. Modelling of parabolic trough direct steam generation solar collectors. **Solar Energy**, v. 62, n. 6, p.

395–406, 1998.

ORÓ, E. et al. Comparative life cycle assessment of thermal energy storage systems for solar power plants. **Renewable Energy**, v. 44, p. 166–173, 1 ago. 2012.

PATNODE, A. Simulation and performance evaluation of parabolic trough solar power plants. **University of Wisconsin-Madison**, v. Master, p. 5–271, 2006.

PAVLOVIĆ, T. M. et al. A review of concentrating solar power plants in the world and their potential use in Serbia. **Renewable and Sustainable Energy Reviews**, v. 16, n. 6, p. 3891–3902, 1 ago. 2012.

PHILIBERT C. **Technology roadmap – solar thermal electricity. International Energy AgencyInternational Energy Agency**. [s.l: s.n.].

PIGOZZO FILHO, V. C. Análise experimental de um sistema solar com concentrador cilindro parabólico. 2013.

PIGOZZO FILHO, V. C. et al. **Projeto , construção e testes de um protótipo concentrador solar Fresnel linear para geração direta de vapor para processos industriais**. VII Congresso Brasileiro de Energia Solar. **Anais**...Gramado: 2018Available in: <http://anaiscbens.emnuvens.com.br/cbens/article/view/399>. Accessed in: 20 jun. 2018

PIGOZZO, V.; SÁ, A. DE; PASSOS, J. Desempenho de um absorvedor multi-tubos para geração direta de vapor em concentradores Fresnel lineares. **agenda.uib.es**, [s.d.].

PYE, J. D.; MORRISON, G. L.; BEHNIA, M. Unsteady effects in direct steam generation in the CLFR. **Anzses**, p. 1–9, 2007.

PYE, J.; MORRISON, G.; BEHNIA, M. Pressure drops for direct steam generation in line-focus solar thermal systems. **Australia and New Zealand Solar Energy Society (ANZSES) Conference**, n. Romero 2002, 2006.

REDA, I.; ANDREAS, A.; NREL, A. A. Solar Position Algorithm for Solar Radiation Applications (Revised). **Nrel/Tp-560-34302**, n. January, p. 1–56, 2008.

ROJAS, M. E.; DE ANDRÉS, M. C.; GONZÁLEZ, L. Designing capillary systems to enhance heat transfer in LS3 parabolic trough collectors for direct steam generation (DSG). **Solar Energy**, v. 82, n. 1, p. 53–60, 2008.

ROLDÁN, M. I.; VALENZUELA, L.; ZARZA, E. Thermal analysis of solar receiver pipes with superheated steam. **Applied Energy**, v. 103, p. 73–84, 2013.

ROUHANI, S. .; AXELSSON, E. Calculation of void volume fraction in the subcooled and quality boiling regions. **International Journal of Heat and Mass Transfer**, v. 13, n. 2, p. 383–393, 1 fev. 1970.

RUSSELL, F. 27--Heat Transfer Analysis and Modeling of a Parabolic Trough Solar Receiver Implemented in Engineering Equation Solver.

National Renewable Energy Laboratory, n. October, p. 164, 2003.

SÁ, A. B. et al. **Geometrical Parametric Analysis to Find Optimum Configuration of a Solar Concentrator Workbench Using Linear Fresnel Technology**. Proceedings of the ISES Solar World Congress 2015. **Anais**...Freiburg, Germany: International Solar Energy Society, 2016Available in: <http://proceedings.ises.org/citation?doi=swc.2015.10.06>. Accessed in: 20 jun. 2018

SALLABERRY, F. et al. Toward a standard testing methodology for solar thermal collectors with variable-geometry: The direct radiation incidence angle modifier issue. **Solar Energy**, v. 121, p. 31–40, 1 nov. 2015.

SERRANO-AGUILERA, J. J.; VALENZUELA, L.; PARRAS, L. Thermal 3D model for Direct Solar Steam Generation under superheated conditions. **Applied Energy**, v. 132, p. 370–382, 2014.

SOLANGI, K. H. et al. A review on global solar energy policy. **Renewable and Sustainable Energy Reviews**, v. 15, n. 4, p. 2149–2163, 1 maio 2011.

SOLEC. **Solar Selective Absorbing Coating for Concentrating Collectors**. Available in: <https://www.solec.org/solkote/concentrating-applications/>. Accessed in: 28 jun. 2018.

SOUSA, S. et al. **Experimental evaluation of heat loss from a multi-tube trapezoidal cavity receiver for a linear Fresnel solar concentrator considering natural and forced convection conditions**. Procceedings of the 24th ABCM International Congress of Mechanical Engineering. **Anais**...ABCM, 2017Available in: <http://abcm.org.br/anais-de-eventos/COB17/1304>. Accessed in: 20 jun. 2018

SUN, J.; LIU, Q.; HONG, H. Numerical study of parabolic-trough direct steam generation loop in recirculation mode: Characteristics, performance and general operation strategy. **Energy Conversion and Management**, v. 96, p. 287–302, 2015.

SUNCNIM. **Solar steam generators | Suncnim**. Available in: <https://www.suncnim.com/en/solar-steam-generators>. Accessed in: 28 jun. 2018.

TAITEL, Y.; DUKLER, A. E. A model for predicting flow regime transitions in horizontal and near horizontal gas-liquid flow. **AIChE Journal**, v. 22, n. 1, p. 47–55, 1 jan. 1976.

VALENZUELA, L. et al. Control concepts for direct steam generation in parabolic troughs. **Solar Energy**, v. 78, n. 2, p. 301–311, 2005.

VALENZUELA, L. et al. Control scheme for direct steam generation in parabolic troughs under recirculation operation mode. **Solar Energy**, v. 80, n. 1, p. 1–17, 2006.

VALENZUELA, L.; HERNÁNDEZ-LOBÓN, D.; ZARZA, E. Sensitivity analysis of saturated steam production in parabolic trough collectors. **Energy Procedia**, v. 30, p. 765–774, 2012.

VDI-GESELLSCHAFT VERFAHRENSTECHNIK UND
CHEMIEINGENIEURWESEN. **VDI Heat Atlas**. [s.l.] Springer, 2010.
VIJ, A.; DUNN, W. Modeling of two-phase flows in horizontal tubes. 1996.
WALKER, G. S. **Development of a Low Cost Linear Fresnel Solar
Concentrator.** [s.l.] Stellenbosch : Stellenbosch University, 2013.
WALLIS, G. **One-dimensional two-phase flow**. New York, NY: McGraw-
Hill, 1969a.
WALLIS, G. One-dimensional two-phase flow. 1969b.
WENDELIN, T.; DOBOS, A.; LEWANDOWSKI, A. **SolTrace: A Ray-
Tracing Code for Complex Solar Optical Systems**. Golden, CO (United
States): [s.n.]. Available in: <http://www.osti.gov/servlets/purl/1260924/>.
Accessed in: 5 jun. 2018.
WOJTAN, L.; URSENBACHER, T.; THOME, J. R. Investigation of flow
boiling in horizontal tubes: Part I—A new diabatic two-phase flow pattern
map. **International Journal of Heat and Mass Transfer**, v. 48, n. 14, p.
2955–2969, 1 jul. 2005a.
WOJTAN, L.; URSENBACHER, T.; THOME, J. R. Investigation of flow
boiling in horizontal tubes: Part II—Development of a new heat transfer
model for stratified-wavy, dryout and mist flow regimes. **International
Journal of Heat and Mass Transfer**, v. 48, n. 14, p. 2970–2985, 1 jul.
2005b.
XU, R.; WIESNER, T. F. Closed-form modeling of direct steam generation
in a parabolic trough solar receiver. **Energy**, v. 79, n. C, p. 163–176, 2015.
YAN, Q. et al. Dynamic modeling and simulation of a solar direct steam-
generating system. **International Journal of Energy**, 2010.
ZARZA, E. et al. The DISS Project: Direct Steam Generation in Parabolic
Trough Systems. Operation and Maintenance Experience and Update on
Project Status. **Journal of Solar Energy Engineering**, v. 124, n. 2, p. 126,
2002.
ZARZA, E. et al. Direct steam generation in parabolic troughs: Final results
and conclusions of the DISS project. **Energy**, v. 29, n. 5–6, p. 635–644,
2004.
ZHU, G. Development of an analytical optical method for linear fresnel
collectors. **Solar Energy**, v. 94, p. 240–252, 1 ago. 2013.
ZHU, G. et al. History, current state, and future of linear Fresnel
concentrating solar collectors. **Solar Energy**, v. 103, p. 639–652, 2014.
ZUBER, N. Hydrodynamic aspects of boiling heat transfer (thesis). 1959.

APPENDIX A - SUMMARY OF THE WORK PUBLISHED BY THE GROUP HELIOTÉRMICA SO FAR

This appendix gathers the works presented or published, performed by the Heliotérmica group of the LEPTEN laboratory, of the Federal University of Santa Catarina.

Some works were performed previous to the LFC project and are related to investigations on PTC technology. They are:

- 2013 - ISES Solar World Congress.

The work entitled "Experimental and numerical analysis of thermal losses of a parabolic trough solar collector" which makes a comparison between an experimental PTC work performed by LEPTEN with results from modeling (FILHO et al., 2014). It was published on the energy procedia, and orally presented in Cancun, Mexico on November of 2013

- 2013 – SBPC 65ª Reunião Anual da Sociedade Brasileira para o Progresso da Ciência.

The poster entitled "Análise teórica e experimental de coletores solares concentradores cilindro-parabólicos" was presented on the event, showing the results of comparison between an experimental PTC work performed by LEPTEN with results from modeling. It was presented on July of 2013.

First, at the beginning of the project Heliotérmica, an extensive review work was performed, to assess the experimental and theoretical works performed on the DSG subject. The result of this study follows:

- 2018 - Renewable and Sustainable Energy Reviews.

The work entitled "Direct steam generation in linear solar concentration: Experimental and modeling investigation – A review" was published on the 90th edition of the Renewable and Sustainable Energy Reviews, and it gathers the main experimental and theoretical works performed on DSG. This work was received in revised form in 18 March 2018 and accepted on 24 March 2018.

Later, an investigative work was performed in order to find the adequate LFC geometry. The following works are the result of these studies.

- 2015 - ISES Solar World Congress.

The work entitled "Geometrical parametric analysis to find optimum configuration of a solar concentrator workbench using linear Fresnel technology" shows the steps in development of the design of the LEPTEN LFC (BITTENCOURT et al., 2015). It was orally presented in Daegu, Korea, on November of 2015.

- 2015 - COBEM 2015 - 23rd ABCM International Congress of Mechanical Engineering.

The work entitled "Geometric design and optimization of a linear Fresnel solar collector" follows the same line of research as the previous, showing some new results (BURIGO et al., 2015). It was orally presented in Rio de Janeiro, Brazil, on December of 2015.

- 2015 - All About Energy 2015

A poster entitled "Desenvolvimento de um concentrador solar tipo Fresnel linear" was presented in this event, which is the largest event of renewable energy of the Latin America. It showed the development steps of the LEPTEN LFC. It happened in Praia Mansa/CE, Brazil, on July of 2015.

In parallel, an indoors test bench was built as part of master studies. This workbench intended to study the heat losses of the receiver designed for the LEPTEN LFC.

- 2017 - 23rd SolarPACES

The work entitled "Experimental Evaluation of Heat Loss from a LFC's Multi-tube Trapezoidal Cavity Absorber Considering Strategic Painting of the Tubes" shows the main results of the indoors bench (SOUSA et al., 2017). It was presented in Santiago, Chile, on September 2017.

- 2017 - COBEM 2017 - 24th ABCM International Congress of Mechanical Engineering

Another results of the indoors bench can be seen on the work entitled "Experimental evaluation of heat loss from a multi-tube trapezoidal cavity receiver for a linear Fresnel solar concentrator considering natural and forced convection conditions" (SOUSA et al., 2017). It was presented in Curitiba, Brazil on December of 2017,

Later, with the LEPTEN LFC in operation, further works were produced. They approach topics such as construction, operation, control strategy and preliminary results of the LFC.

- 2017 - 69ª Reunião Anual da SBPC

The poster entitled "DESENVOLVIMENTO DE ESPELHOS CURVOS PARA UM CONCENTRADOR HELIOTÉRMICO DO TIPO FRESNEL LINEAR" was presented during event, and it shows the construction steps for the curved mirror system of the LEPTEN LFC. This took place on Belo Horizonte/MG, Brazil, in July of 2017.

- 2017 - COBEM 2017 - 24th ABCM International Congress of Mechanical Engineering

The work entitled "Conception and evaluation of a tracking system for a linear Fresnel concentrator" shows the steps in developing the tracking system of the LEPTEN LFC, and a study of its performance (BROGNI et al., 2017). It was presented in Curitiba, Brazil on December of 2017,

- 2018 - CEBENS 2018 - VII Congresso Brasileiro de Energia Solar

The work entitled "Projeto, construção e testes de um protótipo concentrador solar Fresnel linear para geração direta de vapor para processos industriais" shows an overview of the experimental LFC from LEPTEN, with some preliminary results (PIGOZZO FILHO et al., 2018). It was presented in Gramado, Brazil on April of 2018.

- 2018 - CIES 2018 - XVI Congreso Ibérico y XII Congreso Iberoamericano de Energía Solar

The work entitled "Desempenho de um absorvedor multi-tubos para geração direta de vapor em concentradores fresnel lineares" shows the behaviour of the multi-tube receiver from the LEPTEN LFC (PIGOZZO; SÁ; PASSOS, [s.d.]). It was presented in Madrid, Spain, on June of 2018.

- 2018 - ENCIT 2018 - 17th Brazilian Congress of Thermal Sciences and Engineering

The extended abstract entitled "on the heat transfer of a multi-tube absorber for a linear Fresnel solar concentrator operating with direct steam generation" was submitted and further work is in development.

- 2018 - XXIV Jornadas Jóvenes Investigadores

The extended abstract entitled "Geração de vapor em concentradores solares Fresnel linear – projeto, construção e aspectos da transferência de calor" was submitted and further work is in development.

APPENDIX B - LEPTEN LFC WORKBENCH DETAILS

- Project and conception

The first step inside the project was to design an LFC with satisfactory geometrical efficiency and viable costs. The design of an LFC must take into account several parameters, such as the number of mirror lines (n), the width of the receiver and mirrors (W_r; W_m), the total collector area ($W_{col}*L_{col}$), the height of the receiver (h_r), the curvature of the mirrors (r_m) and the spacing between mirrors (c_m). All these parameters can be seen in Figure B-1, and they have an influence on the final optical efficiency of the LFC system. Different configurations of receiver were studied, both considering single tube with parabolic compound secondary reflector, and multi-tube trapezoidal cavity receiver.
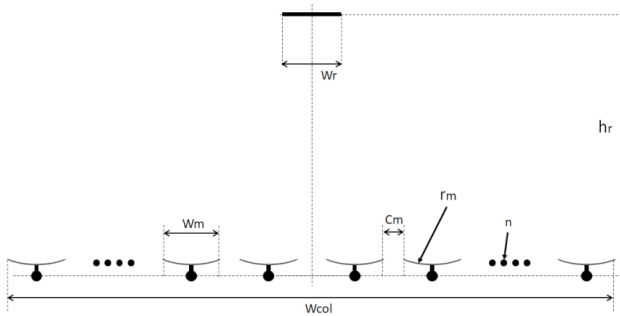
Figure B- 1- LFC geometrical parameters.

To evaluate this effect, the Heliotérmica group developed a Monte Carlo Ray Tracing (MCRT) software in Matlab, that allowed to automatically change these parameters either one at a time or several at a time.

The MCRT consists on the generation of a predefined number of solar rays that are traced throughout the optical system, taking into account its iteration with the optical elements. Iterations of both probabilistic and deterministic nature are computed (DELATORRE et al., 2014). This method uses geometric relations and optical properties to obtain optical and geometric efficiencies of the collector (ZHU, 2013). In this step, only the optical performance is analyzed, the thermal losses are left out of this design stage.

To validate the Matlab model, another MCRT software was used. This software is called SolTrace and it was developed by the National Renewable Energy Laboratory. This well-known software has already been compared and validated to experimental data in several works from

literature (WENDELIN; DOBOS; LEWANDOWSKI, 2013). To validate, some LFC configurations were modeled in both software, and the results were compared. The maximum heat flux difference on the receiver was 1.1%

Although it is an already consistent MCRT software, SolTrace has some limitations. The main is that it does not allow for an automatic and fast change of the parameters, in order to evaluate several different LFC configurations. Therefore, after validated, the Matlab model was used to perform a sensitivity analysis, to obtain the final design configuration of the LEPTEN LFC. A more detailed version of this sensitivity analysis and conclusions of this work can be seen on (BURIGO et al., 2015) and (SÁ et al., 2016).

One main aspect that influenced on the LFC configuration was the available area on the platform. In order to leave space to work and move around the workbench, the maximum collector width was set on 5m. The total length was set on 12 m, in order to make the best use of the space available. Due to safety reasons, the height of the receiver was limited on 4.5 m.

The final configuration of the workbench is an LFC of 5 m x 12 m, with ten mirror lines, each containing 12 mirrors of 1000 mm x 450 mm. the spacing between mirror lines is equal for all lines. The receiver was set on a multi-tube trapezoidal cavity configuration, with 346 mm of aperture on its bottom, and located at a height of 3.75 m.

- Curved mirrors

One of the main advantages of the LFC technology is its potential of cost reduction when compared with the PTC (MORIN et al., 2012). One of the factors that allows this cost reduction is the possibility to use flat mirrors, while PTC have a complex mirror geometry.

These flat mirrors can later be cold bended to create a small curvature, with either a parabolic or cylindrical shape. Usually this curvature is so small that there is almost no constructive difference between the two shapes. This allows increasing the concentration factor, reducing the absorber element size, and achieving higher temperatures.

Considering the presented facts, the mirror configuration chosen was small modules of 1000 mm x 450 mm of curved mirror, using common mirrors locally manufactured to reduce costs. Each two lines, equidistant from the center of the LFC, have a different curvature from the other lines. The focal distance of these lines can be seen on Table B-1. The lines are counted from east to west.

Table B- 1- Focal distances of the mirror lines.

Lines	1 & 10	2 & 9	3 & 8	4 & 7	5 & 6
Focal distance [mm]	4560.60	4306.40	4105.40	3965.80	3894.10

Several modular prototype configurations to fixate and bend the mirrors were developed and tested. This task was time consuming and many prototypes concentrated tensions on the bended mirrors, which leaded to their breakage within a few days. Other configurations would not maintain the desired curvature for long. The final configuration succeeded on the task, and there are some mirrors on the workbench that are exposed to inclement weather for over 3 years now, and still maintain the mirror curvature.

For that, the design of the fixation model developed consists on a structure of four laser cut galvanized steel profiles bound together by five aluminum U profiles, as can be seen in Figure B-2. The laser cut guarantees a great precision, and the profiles have both the required curvature for each line, as the cut to fixate the modular structure on the square axis of the mirror line. The U profiles are responsible for distributing the tension throughout the mirror.
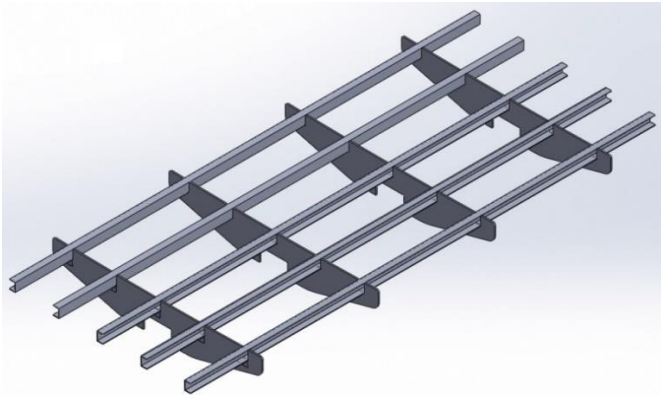
Figure B- 2 - Scheme of the fixation of the mirrors.

To perform the bonding of the glass with the structural module, MDF presses were developed, also laser cut to give precision and repeatability to the process. The glass-metal bonding was done with an MS polymer type glue. The process of fixation of the mirror can be seen in Figure

B-3. Figure B-3(a) shows the application of glue on the modular structure supported by the MDF template, in order to fixate the mirror. Figure B-3(b) shows the weights pressing the mirror against the modular structure, to promote a proper fixation.

Figure B- 3– Fixation of the mirror. a) Application of glue on the modular structure supported by the MDF template in order to fixate the mirror. b) weights pressing the mirror against the modular structure.

During the initial phases of the set-up of the bench, some mirrors were broken, and this modular configuration worked great in face of these setbacks. It is relatively easy to exchange modules of mirrors on the mirror line. Figure B-4 shows the modules of curved mirrors installed at the LFC workbench.
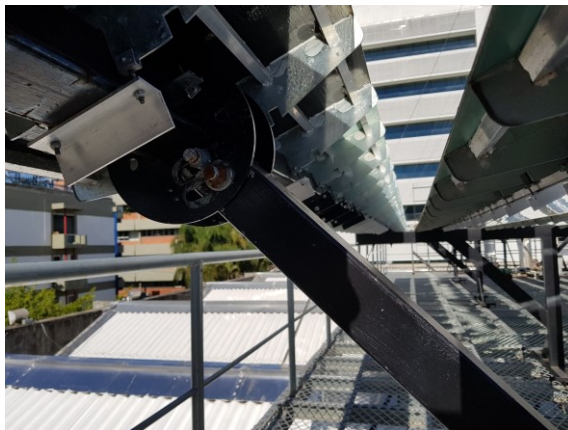
Figure B- 4 - Mirrors fixated on the axis of the mirror line of the LFC prototype.

- • Trapezoidal cavity receiver

The trapezoidal cavity with multi-tubes configuration was adopted for the receiver of the LEPTEN LFC. This component is the most important for the present work, for it represents the testing section itself. It is inside the absorber element of the receiver that the HTF will absorb heat from the concentrated radiation, and in some tests, change from subcooled liquid to a saturated mixture. The absorber element is composed by six tubes of 25,40 mm of outside diameter (OD), totaling a width of 152.40 mm (i.e., 6 x 25.4 mm).

The multi-tubes configuration was based on economic and constructive aspects. The evacuated tube, usually found on linear CSP, is usually more expensive and not sold in small quantities, which is the case of the test prototype.

In addition, the curvature of the mirrors would have to be very precise and accentuated to concentrate the radiation in only one tube. Another possibility would be to use a secondary parabolic compound reflector, which would also need a very precise geometry that did not deform much with the increase of the temperature, and a reflectance that did not deteriorate with concentrated radiation. The multi-tube configuration allows simplified manufacturing of curved mirrors, requiring only stainless-steel tubes, welding and the subsequent application of selective ink.

The trapezoidal cavity is composed by two folded structures, the internal and external, welded together. These structures were made from two folded aluminum plates, each 2 mm thick. The space between the plates is on average 75 mm thick and is filled with rock wool for thermal insulation. Figure B-5 shows a front view of the receiver being fixed on the workbench, without the absorber element.

A flat glass plate of high transparency is positioned on the lower part of the cavity in order to minimize the convective losses to the environment while allowing the entrance of the solar irradiation. This glass was commercially found as the type "Extra Clear Diamond", and although it is not specific for CSP, it is used to protect some photovoltaic systems. The ideal would be to use a borosilicate glass; however, these types of glass are very expensive.

The absorber was built in modules. Each module is two meters long and has its ends closed with a welded aluminum cap. This cap can be seen in Figure B-5, and it is also responsible for the structural fixation of the six absorber tubes. In total, six modules were used, totaling 12 m of length.
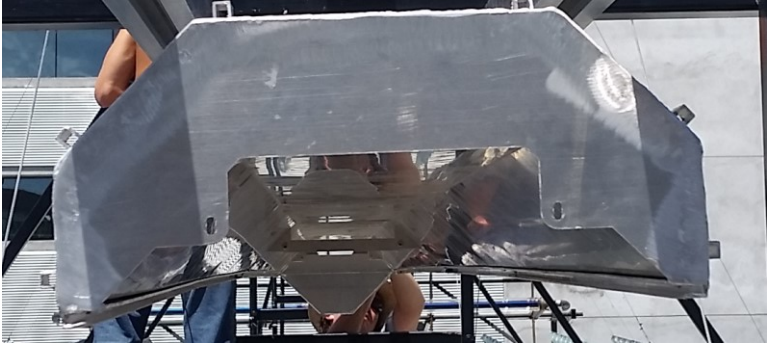
Figure B- 5- Front view of the trapezoidal cavity receiver without the absorber element.

The interconnections of the absorber tubes are done by means of flexible stainless-steel hoses. To fixate these hoses on the tubes without interference, some angular extensions were welded on the extremities of the absorber tubes, as it can be seen in Figure B-6.
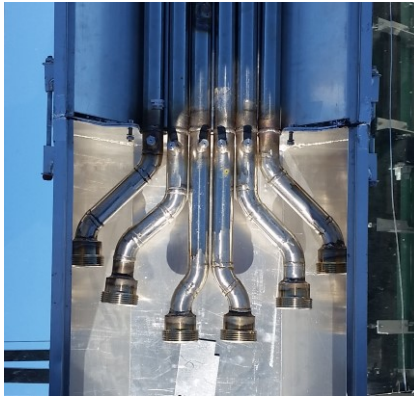
Figure B- 6 - Extensions welded on the extremities of the absorber tubes.

The HTF flows circularly on the receiver, passing by all the absorber tubes one time. It enters the receiver by the first absorber tube, at the south extremity of the workbench. It flows first at the more peripheral tubes, and last at the middle tubes, exiting by the fourth tube also at the south extremity of the workbench. Mode details of this configuration can be seen on appendix C and section 0.

The receiver is fixed at the bench structure by two rails, which allows it to move in the south and north direction as seen in Figure B-7.

This innovative design was developed in order to compensate the end losses during tests, and it is discussed in more detail on Appendix D, where this system is analyzed throughout one year.

Figure B- 7- Fixation of the receiver on rails.

Although the polished stainless steel has a low emissivity, which is desirable in terms of heat losses, it also has a low absorptivity that makes is not viable for a solar concentrator. Therefore, the six absorber tubes were coated with a selective ink. The ink used was the SOLKOTE, from the American company SOLEC (SOLEC, 2018). According to the manufacturer the emissivity ranges from 0.20 to 0.49 depending on the substrate and the thickness of the paint layer. The absorbance ranges from 0.88 to 0.94 depending on the same factors. The ink operating temperature ranges from -73 °C to 538 °C. The application of the product was done by painting with air gun, as can be seen in Figure B-8.

Figure B- 8 - Painting of the absorber tubes.

The absorber was instrumented in three sections: beginning, middle and end. There are measurements made directly in the fluid in each of the six tubes. These types of measurement were the ones used in the present work. In addition, thermocouples were installed to measure the temperature on the wall of tubes, inner and outer walls of aluminum plates, thermal insulation medium, glass surface and air inside the cavity. However, the fixation of the thermocouples to the tube surface did not present satisfactory results. Welding them to the tube resulted on the destruction of the thermocouple, therefore they were only pressed. This fixation needs improvement for further testing. Figure B-9 (a) shows the instrumentation of the middle section regarding the wall temperatures, and Figure B-9 (b) shows the thermocouples that are inserted on the north extremity of the absorber tubes. There are thermocouples inserted on the absorber tubes on both extremities of the receiver, and one on the fourth absorber tube in the middle section, since this is the last tube that the HTF flows before leaving the receiver.
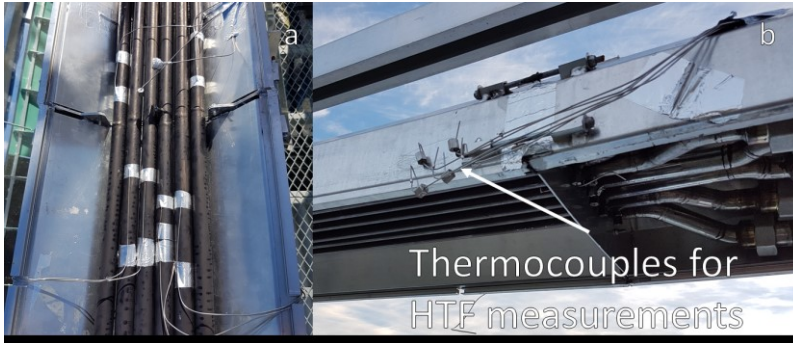
Figure B- 9 - Instrumentation of the receiver. a) Wall surface measurements. b) HTF direct measurements.

As mentioned, the receiver is positioned on rails, and these rails are then fixed on the LFC structure. To do so, pulleys were installed on the top of the LFC structure, and the assemble receiver and rails were hoisted until position. This procedure can be seen in Figure B-10.

Figure B- 10 - Rising procedure of the receiver.

Overall the constructive design of the receiver proved satisfactory. Its modular nature makes it easier to disassemble case its needed, and the fixation of the absorber tubes is done easily, and can be adapted for different absorber element configurations, such as different profiles or tube diameters. And although it takes some manpower to raise and lower the

receiver, it is doable in a few hours in case any adaptation is needed for further tests.

- Solar Tracking

The solar tracking system was developed in order for the mirror lines angular to correctly accompany the solar displacement throughout the day. The solar angular relations and the obtention of the angular offset between the mirror lines can be seen on section 4.3.

The solar tracking system can be divided into two parts, first the mechanical structure and second the control strategy. Regarding the mechanical structure, it was opted to use a single mechanical actuator to move all mirror lines in order to reduce costs. To reproduce a separated movement for each line implies on having a set of one step motor and one inclinometer for each of the lines. Therefore, the final concept of the mechanical system of the solar tracking can be seen in Figure B-11, and it includes one actuator bar, connected to the mechanical actuator that is a linear electrical motor. The movement is carried to the mirror lines through ten parallel lever arms.
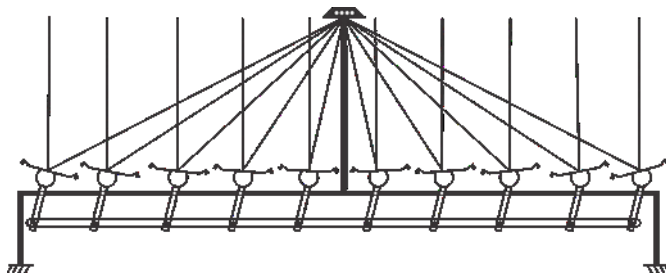
Figure B- 11- Scheme of the mechanical system for solar tracking.

The precision of the tracking mechanism impacts on the concentrated radiation reaching the absorber. The system, therefore, must be very robust and steady, to avoid looseness due to vibration or wind. For that, nylon bushings were installed between the rotating parts. The designed mechanism is able to track the sun position for a solar transversal angle between -80° to 80°, covering most of the day. The electrical linear motor used has a high torque and low speed, even so, a power supply system was installed, and the input voltage was adjusted to reduce speed and increase precision. The final system installed on the LFC can be seen in Figure B-12.

200

Figure B- 12 - Detailed view of the tracking mechanism on the LFC.

For the control system of the solar tracking, the approach chosen was to use the calculated solar position, and from there calculate the position that the second mirror line should have. The solar position was obtained using the Solar Position Algorithm (SPA), developed by the National Renewable Energy Laboratory (NATIONAL RENEWABLE ENERGY LABORATORY, 2018; REDA; ANDREAS; NREL, 2008). The control software was developed in LabVIEW, and it is responsible for retrieve the solar position spreadsheet for each experimental day from the SPA, to calculate the angular position of one mirror line, and to maintain its correct position throughout the day by controlling the linear actuator. In this task only one mirror line is used, since all the lines are interconnected and have the same angular movement.

To maintain the correct angular position, the software must first know the current position of the selected mirror line. To do so, two inclinometers were installed on the second mirror line, covering the range of -80º to 80º. The inclinometers and the linear motor can be seen in more detail in Figure B-13.

An experimental and theoretical analysis of uncertainties was performed in order to evaluate the impact of the angular precision on the concentrated radiation reaching the absorber. The details of this study can be seen on (BROGNI et al., 2017).

Figure B- 13 - Inclinometers and mechanical actuator installed on the LFC.

The variation of the solar concentrated radiation due to the variation of angular position can be seen in Figure B-14. For this visual verification, a white paper with a target drawn in it was positioned on the receiver aperture, and the second mirror line was tested concentrating radiation.
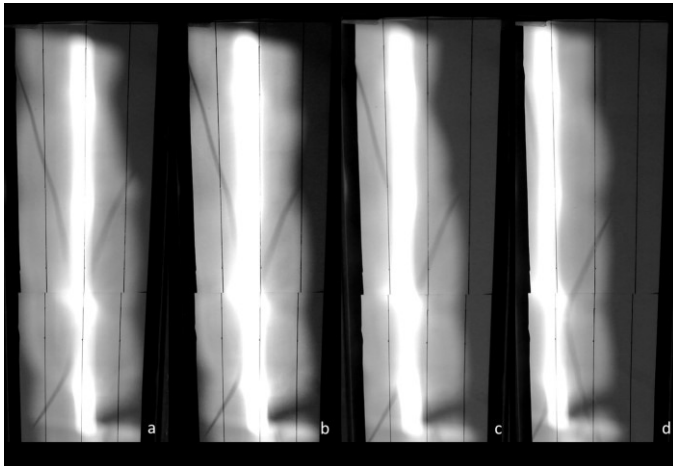
Figure B- 14 - Visual verification of concentration from second mirror line for different angular positions.

Only the second line was positioned because it is the line that has the inclinometers, and a higher concentrated radiation would burn the

white paper. The middle stripe on the white paper indicates the middle of the receiver, and the two outer stripes limits the area of the six tubes.

It can be seen from Figure B-14 that even a small variation on the angular position represents a large displacement on the concentrated radiation. However, as showed on (BROGNI et al., 2017), considering all uncertainties, the maximum angular position error is of $0.12°$, which is a reasonable value for a precise tracking system, as seen in Figure B-14.

Overall, the designed tracking system proved to be able to satisfactorily perform its designated function.

- Hydraulic circuit

A scheme of the hydraulic circuit of the LEPTEN LFC can be seen in Figure B-15. It is composed by all the auxiliary components the HTF flows through before reaching the receiver, and after that. This LFC prototype has a steam separator, that functions as a mass reservoir of water. It is a tubular pressure vessel positioned on the vertical.
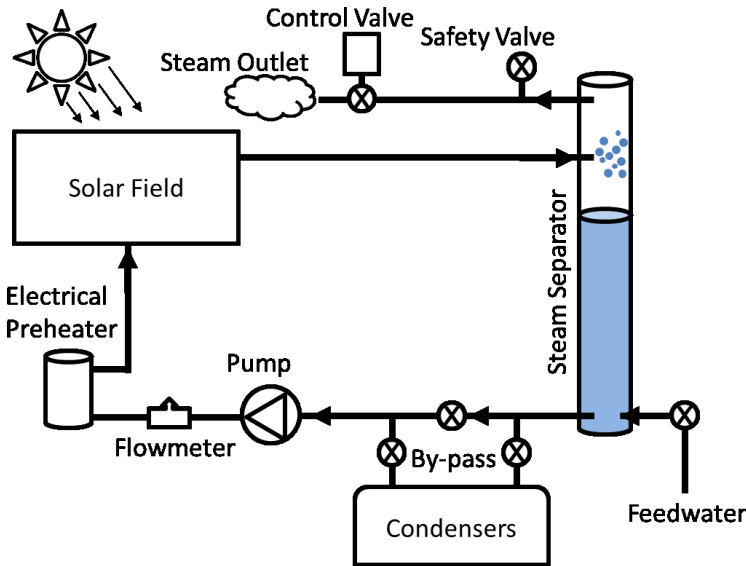
Figure B- 15- Scheme of the hydraulic system.

Feedwater enters the steam separator from its bottom, however, during tests the feedwater valve is always closed. During steam generation the level of condensate drops while steam is purged from the system, and only between testes the steam separator is filled again. To guarantee that steam would not enter the pump, there are three liquid level sensors

installed on the steam separator, and the low-level sensor indicates the end of the test.

Water exists the steam separator also by its lower part, to ensure that even in two-phase flow tests, only condensate is being routed to the pump. Before reaching the pump, there are three routes that the HTF can pass. It can go directly to the pump, it can go first to the condensers, or it can be divided and a fraction goes to the condensers while the other passes directly to the pump. The condensers installed in by-pass are used for some single-phase flow tests, where maintaining a stable lower temperature was needed. Figure B-16 shows the ground level components of the hydraulic system, such as the condensers in by-pass and the pump.
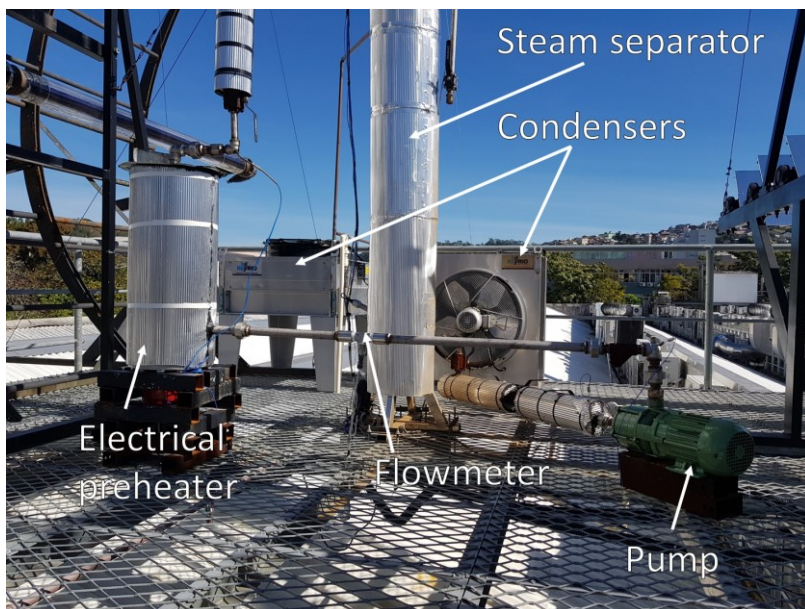
Figure B- 16 - Photograph of the hydraulic system.

At the outlet of the pump the HTF passes by the flowmeter. This configuration was chosen because the flowmeter is of the turbine type, so any air or vapor bubbles would cause a variation on the measurements. And for the two-phase flow tests, the HTF exiting the steam separator is at the saturated condition, and if it would go directly to the flowmeter it could carry small bubbles or create them due to pressure drop on the pipes and on the flowmeter. For that, first the pump promotes a pressure increase on the HTF, taking it to a subcooled liquid state. The flowmeter

used is the FTB-1424-HT from Omega©, and it was calibrated for water at ambient temperature. No calibration laboratory found would calibrate it for subcooled liquid water up to 230 ºC.

For that manner, an experimental verification procedure of the flowmeter behavior was performed for higher temperatures. This experimental procedure was made using the LEPTEN LFC hydraulic and control structure, and its details and results can be seen on Appendix E.

After passing the flowmeter, the subcooled HTF passes by an electrical preheater before it finally reaches the receiver on the solar field. This electrical preheater is a pressure vassel with a flanged multi-tubular 20kW electrical heater coupled. This equipment can be used for different ends. It can speed up the beginning of the test, helping the system to achieve the desired HTF temperature faster. It can also just maintain a stable inlet temperature condition for the HTF entering the receiver, helping achieve steady state conditions. It can also be used on the two-phase flow tests to put the subcooled HTF exiting the pump closer to the saturated condition before it enters the receiver. The control of the electrical preheater was done by a PID (proportional-integral-derivative) logical controller.

After exiting the solar field, the HTF is routed again to the steam separator, completing the cycle. If the tests are single-phase flow then this is the end of the HTF cycle. For the two-phase flow cases, the steam generated is purged from the system by the control valve. The pipe line that goes to the control valve exits the steam separator from its top part, to prevent condensate to enter the line. This pipeline is then directed downwards for the connections and valves to be in a height easier to access for installation, inspection and possible maintenance.

The control valve is located just after a safety valve, that is set to open if the pressure on the system surpasses 23 bars. These components can be seen in Figure B-17. The control valve is responsible for setting the internal pressure of the steam separator.

There is a by-pass of the two valves to simplify making single-phase flow tests at ambient pressure.

Figure B- 17 - Control and safety valves.

  The hydraulic system also includes temperature measurement of the HTF in several points such as before and after the pump, after the preheater, after the condenser and after the control valve. There are two pressure measurements, one just before the HTF enters the receiver, and another before the fluid re-enters the steam separator.

  The workbench also counts with several additional auxiliary equipment, such as an Agilent for data acquisition, power supplies for the linear motor and inclinometers, a computer to make the control of the solar tracking and store the test data, PID controllers not only for the preheater but also for the control valve, two-phase and three-phase current supply, frequency inverter to control the pump, among others. Overall the LEP-TEN LFC is a complex bench, result of four years of dedicated work from the Heliotérmica group.

APPENDIX C- EQUIVALENT LENGTH CALCULATION FOR BENDS AND ELBOWS FOR THE LEPTEN LFC

The LEPTEN LFC prototype uses a multi-tube trapezoidal cavity receiver. The information about the inner roughness of the tubes can be found on the table of Figure C-1.

Drawn steel tubes	New	0.04 (0.02–0.1)
	Cleaned after long service	0.15–0.20
	Moderately rusted or slightly fouled	≤ 0.40
	Heavily fouled	≤ 3.0
Galvanized sheet steel	Smooth (air ducts)	0.07
Galvanized steel tubes	Normally galvanized	0.15
Welded steel pipes	New	0.05 (up to 0.1)
	New, bituminized	0.05
	Used, cleaned	0.15–0.20
	Uniformly rusted	≤ 0.40
	Slightly fouled	1–1.5
	Heavily fouled	2–4
Riveted steel pipe		0.9 (0.5–10)

Figure C- 1– Roughness of the internal surface of tubes. Source (VDI-GESELLSCHAFT VERFAHRENSTECHNIK UND CHEMIEINGENIEURWESEN., 2010).

For the flow on the receiver, as it can be seen in Figure C-2, the HTF enters the receiver by the south extremity of the receiver, at the first absorber tube. At the north extremity of the receiver the following absorber tubes are interconnected: first with the sixth; second with the fifth and third with the fourth. At the south extremity of the receiver, the sixth tube is connected to the second, and the fifth tube is connected to the third, and the HTF exits the receiver by the south extremity of the fourth tube.

The interconnection between tubes is made through a flexible stainless steel hose. The equivalent length method is used in order to estimate the pressure drop in these interconnections. For the equivalent length calculation, the flexible hoses are modeled following the scheme in Figure C-2.
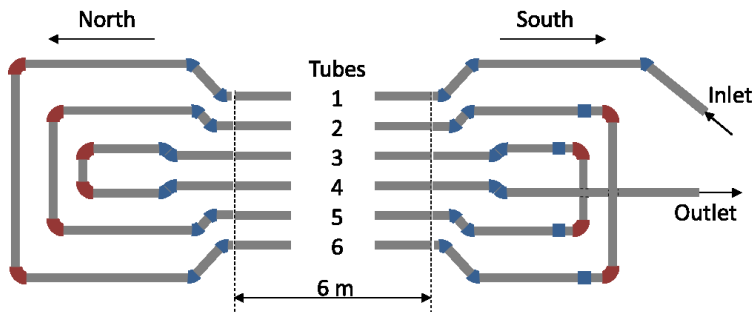
Figure C- 2– Scheme of the absorber tubes interconnections.

Table C-1 shows the lengths of solid 1'' tubes and of the flexible hose interconnecting two tubes. It also shows the number of elbows curved at 45º and 90º. This information is used to find the equivalent length that will be used in the pressure drop calculations. The two pressure transductors installed at the workbench are located at the inlet before the flexible hose, and on the outlet, after the flexible hose.

Table C- 1– Length and elbows of the interconnecting elements.

Connections	1" Tube		Flexible hose		
	Length [mm]	Elbow 45º	Length [mm]	Elbow 45º	Elbow 90º
Inlet to Tube 1 South	170	2	3750	1	0
Tube 1 to 6 North	340	4	1000	0	2
Tube 6 to 2 South	370	4	770	2	2
Tube 2 to 5 North	400	4	680	0	2
Tube 5 to 3 South	425	4	580	2	2
Tube 3 to 4 North	450	4	575	0	2
Tube 4 to Outlet	225	2	3750	0	0

Table C-2 presents the equivalent length factor for calculations, according to (NEUTRIUM, 2012) and (ENGINEERING TOOLBOX, 2004).

Table C- 2– Equivalent length of pipe for different fittings.

Connection	45° Elbow Curved	90° Elbow Curved
$(L/D)_{eq}$	16	30

Table C-3 shows the total equivalent length considered on the pressure drop calculations on elbows and interconnections.

Table C- 3– Total equivalent length.

	Length of straight tubes [mm]	L_{eq} elbows [mm]
Inlet to Tube 1 South	3920	1104
Tube 1 to 6 North	1340	2852
Tube 6 to 2 South	1140	3588
Tube 2 to 5 North	1080	2852
Tube 5 to 3 South	1005	3588
Tube 3 to 4 North	1025	2852
Tube 4 to Outlet	3975	736

APPENDIX D- MOVING ABSORBER PERFORMANCE ANALYSIS

As described in Section 3.2, the LEPTEN LFC receiver has a moving mechanism. This component has a great influence on performance of the system, therefore it will be detailed in this section. Since the prototype is of a small dimension (total area of 5m x 12 m) the end losses would have a great impact on its performance. With that in mind, the absorber was designed to be supported on a rail, which allows it to be moved. Figure D-1 shows a scheme of the moving absorber. The workbench is installed on the southern hemisphere (Latitude -27.60°), hence the displacement course needed is larger due to south. The designed course of displacement has a total of 3.72 m due south and 1.16 m due to north.
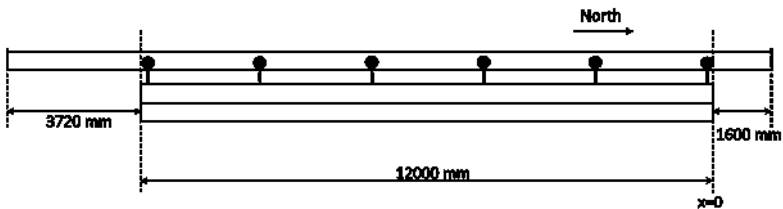
Figure D- 1- Scheme of the moving absorber.

The track of the absorber was marked in order to verify then length displaced during tests, and to compare with the calculated displacement. The verification is visual and not very precise, however, for qualitative purposes the calculated and verified displacement matched reasonably well. Figure D-2 shows the movement marks. This photo was taken during operational day, after the solar noon of the 23 May 2018, at a time where the absorber was already moving back north in order to compensate the longitudinal inclination of the solar vector. For that, the incident angle (θ_i) is used. The solar angular relation is best described in section 4.2.

Figure D- 2 - Photo of the marked track of the moving absorber.

Figure D-3 was taken earlier on the same day (day 143), at a time where the maximum movement of the receiver was not enough to compensate the end losses. The exposure and saturation of the photo were adjusted in order to better verify the concentrated radiation encountered on the extremity of the absorber.
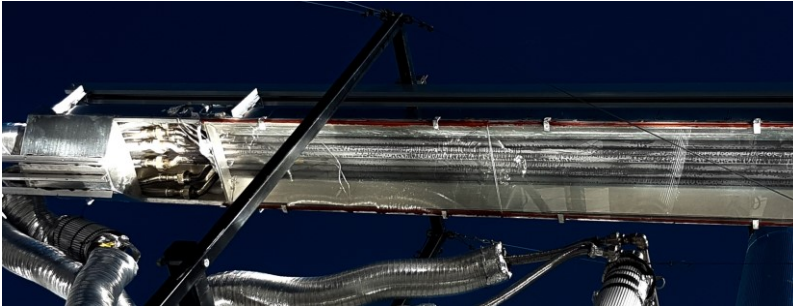
Figure D- 3– End losses with the moving absorber at the maximum movement position due to south.

The solar position was tracked throughout the year. It was seen that the moving absorber is able to compensate end losses for most of the time periods that a test would be performed during the year. Even at times where it did not completely eliminate it, it considerably reduced the end losses.

Figure D-4 shows the results of the simulation for a whole year at the site of the LEPTEN prototype. This simulation was made using the solar position equations presented on (DUFFIE; BECKMAN; WOREK, 2003), modeled in Matlab.

The two blue dotted lines on early and late hours represents respectively the sunrise and sunset hours throughout the year. In this figure four red curves can be seen, two at early hours, and two at late hours. The enclosure between them and the dotted blue lines shows the hours that the moving absorber cannot fully compensate the end losses due to North.

At periods below the two early hour curves, and after the two late hour curves the incidence angle is so inclined south, that the end losses to North are bigger than the 1.16 m that the moving absorber can dislocate.

Ultimately, these periods are not very important in the overall analysis of the concentrator. Actually, most tests begin after 8:00 in the morning and stops before 17:00. In these early and late periods, it is very unlikely to have permanent regime required for the analysis of the concentrator, due to the high transversal angles and consequently the rapidly shading between mirrors. It can be said that for all practical purposes the displacement due to north that the moving absorber has is enough to compensate the end losses in that direction for all possible operational periods for the workbench throughout the year.

There is a black lined circle on the center of the graph. The periods within represent the hours where the moving receiver cannot compensate the end losses due to south. These periods are more critical, for they happen around the solar noon mostly during winter. The ideal would be to increase displacement course in the south direction to 4.7 m, which would fulfill its purpose during all year. However due to space limitations the project was set on a displacement of 3.72 m.
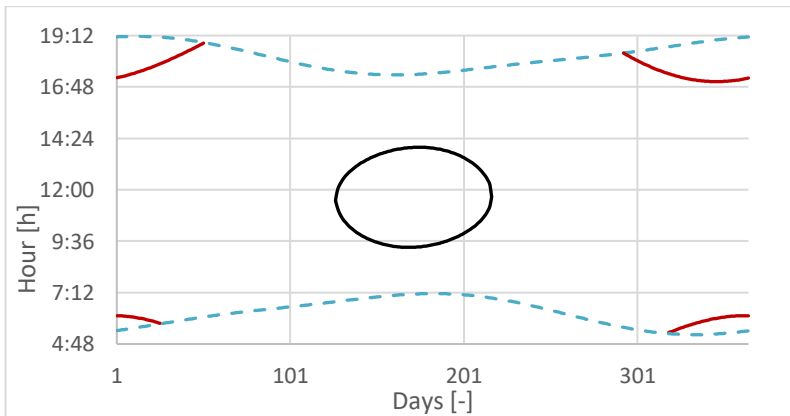

Figure D- 4- Results of the simulation of the moving absorber for a whole year. The blue dotted line represents the sunrise and sunset hours; the red lines delimitate the hours where the moving absorber cannot fully compensate the end losses

212

due to north, and the black circle encompasses the hours where the moving absorber cannot fully compensate the end losses due to south.

The maximum displacement to the south occurs on June 21, the day of the solstice of June, when winter begins at the southern hemisphere. On this day, the absorber should move 4.7 m south to fully compensate the end losses. As said before, the maximum displacement that the moving absorber has due to south is 3.72 m. Even then, the end losses in this specific time of maximum displacement, at June 21, 12:53 of local time, is reduced from 39.17% to 8.17% from a configuration of fixed absorber.

The mean end losses, considering the movement due to south, for only the periods where the moving absorber displacement cannot fully compensate the incidence angle is of 3.82 % to 34.82 % considering a fixed absorber.

For the analysis of a whole year of operation, from sunrise to sundown, for end losses due to south of the collector, the mean end losses for the system with the moving absorber is of 0.37 %, while for a fixed absorber it reaches 14.64 %. The same analysis for the end losses due to north gives a mean value of 0.61 % considering the moving absorber and 5.80 % for a fixed absorber.

The end losses due to north that the moving absorber cannot compensate seam higher, however it happens on less hours during the year, and only on beginning and end of the day, as seen in Figure D-4, having therefore less impact on the thermal performance.

The critical periods are the ones that the moving absorber cannot compensate due to south, and they happened around solar noon starting at 8th of may (day 127) and they end on the 5th of august (day 217). The early that this occurs is at 9:19 at June 19th, and the latter at 13:59 at June 25th. Overall the moving absorber is a design configuration that presents a great advantage for the research viability of small scale LFC prototypes.

APPENDIX E - INFLUENCE OF THE TEMPERATURE OF THE WORKING FLUID ON THE VOLUMETRIC FLOW MEASUREMENT

The flowmeter used in the workbench is of the turbine type; model FTB-1424-HT from Omega©. This model was chosen due to its robustness and for it can sustain operational temperatures up to 232 ºC. Most flowmeters found did not attained the aim temperature of 230 ºC. The sensor gives a signal in frequency obtained by a magnetic pick-up, which can be converted into volumetric flow with the use of a constant provided by the manufacturer.

Although this equipment can sustain high temperatures, it was calibrated for water at near ambient temperature, around 21.5 ºC. This type of flowmeter measures the flow through a rotor, and the viscosity of the fluid influences the number of turns by volume of flow.

The viscosity is a function of the temperature and pressure of the fluid, however, the variation with the pressure for liquid is less appreciable, and can be neglected at the pressure levels that are encountered at the workbench. The fluid at the flowmeter is always subcooled water, since even in two-phase tests the pump compresses the condensate extracted from the steam separator before reaching the flowmeter. There is an interest in verify the influence of the temperature on the volumetric flow measured.

For that, an experimental methodology was adopted, based on visualization of experimental measurements. It was seen a temperature surge at the first thermocouple of the receiver shortly after the turning on of the electrical preheater. This temperature surge was felt by following thermocouples shortly after passing the previous ones. An example of this effect can be seen in Figure E-1, for the inlet and outlet thermocouples. This time interval between the thermocouples measurements appeared to be constant for a given temperature and volumetric flow.
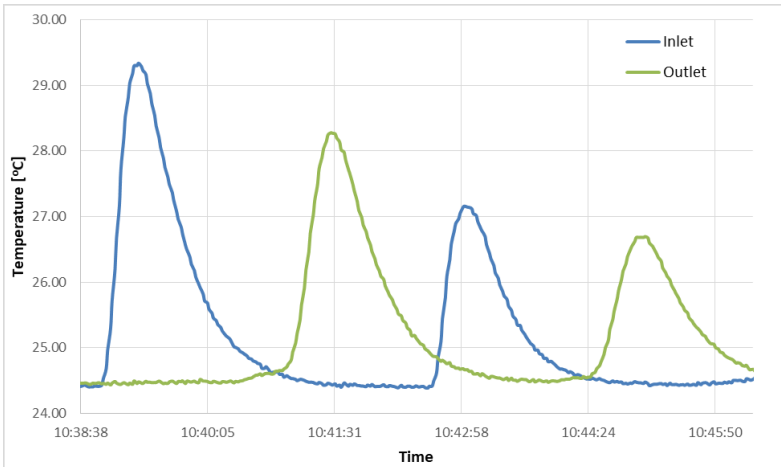
Figure E- 1 - Temperature surges measured by the inlet and outlet thermocouples.

The logic of the methodology is that this temperature surge is dislocated throughout the receiver as heat in the fluid, and the interval of time between measurements represents the time of residence of the fluid, and it is a function of the volumetric flow and the volume of the pipes between thermocouples, as seen in equation (E.01).

$$\Delta t = \frac{A_p\, L_p}{\forall_{HTF}} \tag{E.01}$$

The cross section area of an absorber pipe and the total length between the two thermocouples analyzed are represented by A_p and L_p respectively. It is important to note that the volumetric flow ($\forall_{HTF}$) is measured in l/s, and needs to be converted to m³/s to be used on equation (E.01).

The absorber elements consists on stainless steel tubes with an outer diameter of 25.4mm and the wall thickness of 1.2mm. At the beginning and the end of the receiver, flexible stainless steel corrugated hoses connects the absorber tubes, as illustrated at Figure E-2. In addition, connections were welded at the extremities of the absorber elements in order to fixate these hoses. Figure E-2 also indicates the number of the absorber tubes, and the orientation of the flow, that enters the receiver by the tube 1 and leaves by the tube 4. Only the thermocouples used at this present analysis are showing on the figure, and the prefix TC and the numbers 1,

2 and 3 indicate them. All these elements attached to the tubes add uncertainties on the total volume between two thermocouples, since they have different cross section areas.
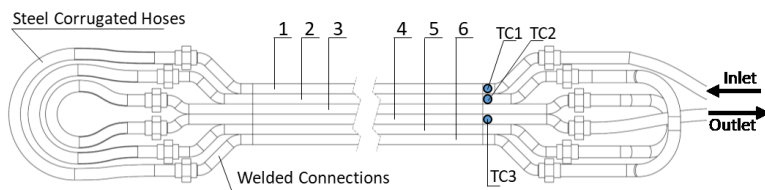

Figure E- 2 - Scheme of the absorber elements connection inside the receiver.

Assuming that the calibration of the flowmeter is of higher precision than the one we would obtain calculating the total volume of pipes, the total length between thermocouples was obtained experimentally. For that, the procedure of temperature surge measurements was performed for the heat transfer fluid near the calibration temperature. Over 60 measurements were performed for six volume flow levels, with frequencies varying from 180 Hz to 710 Hz. The flowmeter constant, given by the calibration procedure of the manufacturer, is $642.37\ Hz/(l/s)$. In order to obtain the total length, its value was altered on equation (01) until the mean difference between all time interval calculated and time interval experimentally obtained reached a minimum. The length obtained in this procedure was used on further calculations.

Summarizing, the first step is using near calibration temperature measurements in order to calibrate the verification procedure. The methodology follows by performing measurements in other temperatures and frequencies of the flowmeter measurements; the variation of these parameters is showed below. The temperature of the fluid is obtained by a thermocouple located just before the flowmeter.

Temperature levels

- Fluid temperature of 40 °C
- Fluid temperature of 60 °C
- Fluid temperature of 80 °C
- Fluid temperature of 100 °C
- Fluid temperature of 120 °C
- Fluid temperature of 140 °C

Frequency levels

- Frequency around 200 Hz

- Frequency around 450 Hz
- Frequency around 700 Hz

In total, 18 flow conditions were analyzed, and each condition is a mean result of the measurement of six temperature surge waves. The procedure was repeated for two thermocouples configuration. The first is called "Total Length Configuration", and it considers the total length of the absorber, measuring the temperature surges on the first and last thermocouple (TC1 and TC3 respectively). The second is considering the difference between the inlet and the first thermocouple on tube 2 (TC1 and TC2 respectively), and it will be called "Partial Length Configuration". To ensure subcooled liquid the control valve of the workbench was set to a pressure higher than the saturated pressure of water at 140 ºC.

The goal is to verify the temperature influence on the volumetric flow measured. For that, the residence time of the fluid between two thermocouples is estimated using the measured frequency and the calibration curve. The expected behavior is that when the temperature rises, the viscosity decreases and the difference between the calculated and measured residence time increases. This would indicate that the calibration curve is no longer suitable for higher temperatures, and that the volumetric flow is no longer accurate. From that a correction for the volumetric flow measured due to increase of the temperature could be drawn.

The results of the experiment, however, showed that the influence of the temperature on the measured volume flow is practically inexistent, or at least, is inside the uncertainty of the experiment. Figure E-3 and Figure E-4 show the result for the two different thermocouple configuration analyzed. On these figures, the x axis represents the time between the first and second thermocouple to experience the temperature surge. On the y axis there is the measured frequency, which can be directly converted into volumetric flow by using the constant given at calibration. The dotted line is the direct relation given in equation (E.01), using the constant from calibration, so it represents the ideal case for calibration temperature. The dots plotted represent the experimental mean value of time between thermocouples for each temperature at each frequency level.
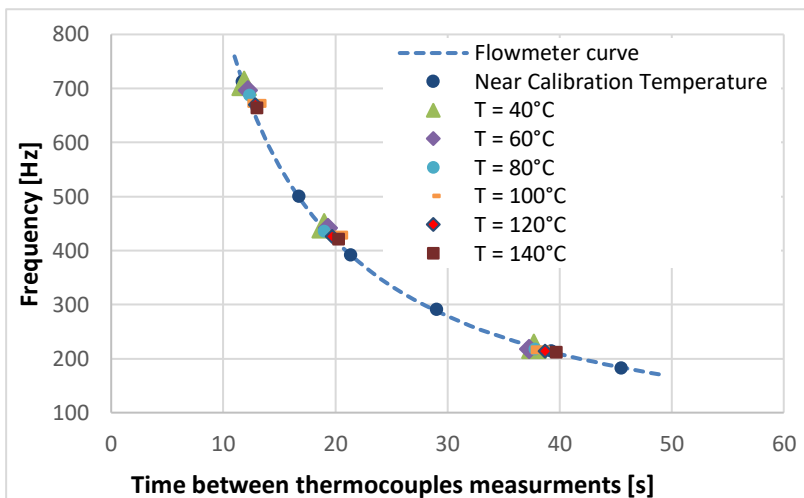
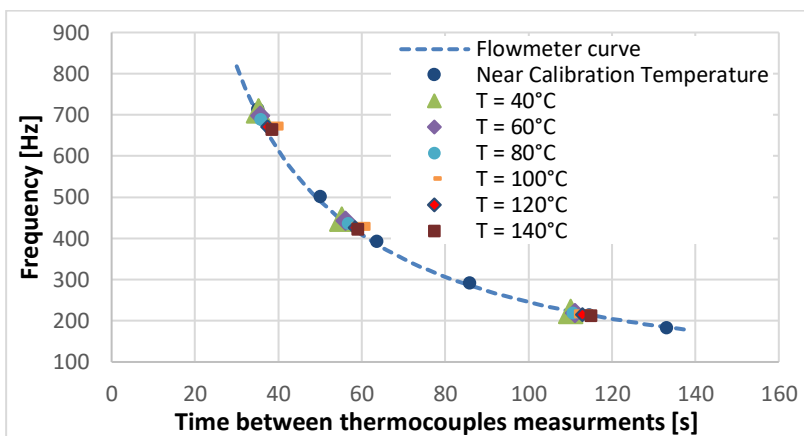Figure E- 3 - Comparison results for the partial length configuration.

Figure E- 4 - Comparison results for the total length configuration.

Table E-1 shows the error between the calculated volume flow and the experimentally obtained using the measured time of temperature surges between thermocouples. As can be seen, there is not a tendency of increasing error with the increase of temperature. The calibration error of the flowmeter is 0.65 % of the measured flow. The presented procedure showed higher errors, however, this was expected due to the uncertainties of correctly selecting the time of maximum temperature surge on the ther-

mocouples measurements. For the partial length configuration, the minimum and maximum error were -2.36 % and 3.03 %, to the temperature level of 60 °C and 100 °C respectively. Considering the total length configuration, the maximum error of 2.24 % occurred for the temperature of 100 °C and the minimum of -2.20 % occurred for the temperature of 140 °C.

Overall, the errors are still reasonable low and apparently random regarding the temperature in order to affirm that, for the range of temperature analyzed; this parameter has no significant influence on the volume flow measured.

Table E- 1 - Error between calculated and experimentally obtained volume flow.

	Partial Length Configuration		Total Length Configuration	
	Max	Min	Max	Min
Near Calibration Temp.	0.67%	-1.10%	1.16%	-1.93%
T = 40 °C	-0.53%	-1.46%	0.05%	-1.70%
T = 60 °C	2.72%	-2.36%	1.25%	-0.99%
T = 80 °C	1.19%	-1.62%	1.58%	-0.73%
T = 100 °C	3.03%	0.01%	2.24%	-0.78%
T = 120 °C	0.68%	-2.31%	1.34%	-1.50%
T = 140 °C	-0.93%	-1.76%	0.52%	-2.20%

The viscosity for subcooled water is reduced around 78 % at 140 °C from its value near the calibration temperature. If the comparison is made for the entire range of working temperature of the workbench, the reduction is around 85 % at 230 °C comparing to the viscosity at calibration temperature. The tests were performed only up to 140 °C due to safety reasons.

The assumption of non-dependency of temperature on the measured volume flow will be extended to all range of operational temperatures. This considering both the lack of dependency of measured volumetric flow with temperature up to 140 °C, and verifying that the viscosity drop from calibration temperature to 140 °C is much more appreciable than the viscosity drop from 140 °C to 230 °C. In the light of these results, the calibration constant of the flowmeter was directly used to calculate the volume flow in all temperature levels analyzed on the workbench.

APPENDIX F- MEASUREMENT DISCREPANCIES

Some discrepancies were found on the two-phase tests at low mass flow rate. Figure F-1 shows one of these tests.

A discrepancy of around 8 °C can be seen on the outlet temperature, and around 0.7 bar on the outlet pressure. One justification would be that the pressure drop calculated on the model is too small, and that if it happened to be equal to the experimental, the temperature profile would match. For that manner, some hypothetical situations were modeled.

The first is showed in Figure F-2, where a different inlet pressure was considered for the model to match the temperature profile.
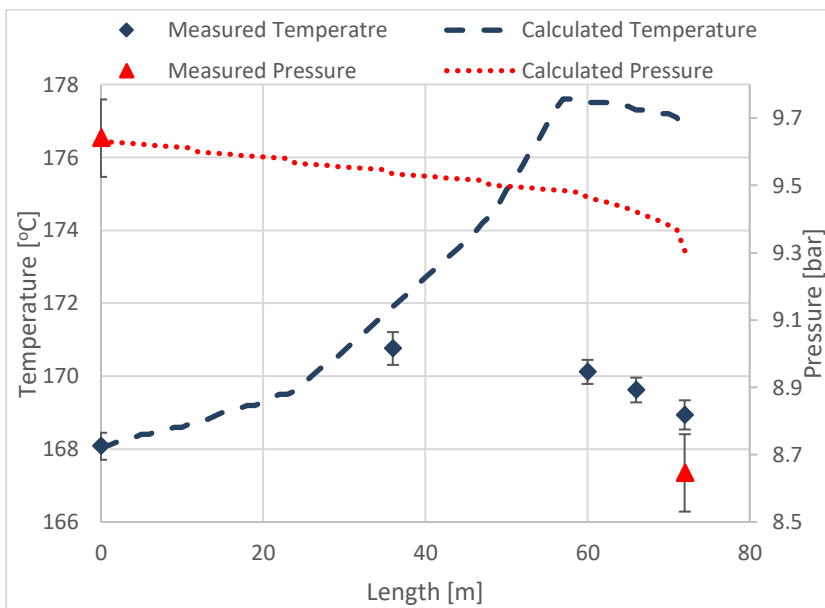

Figure F- 1 - Data discrepancy for the two-phase flow steady state interval from the 26/04.
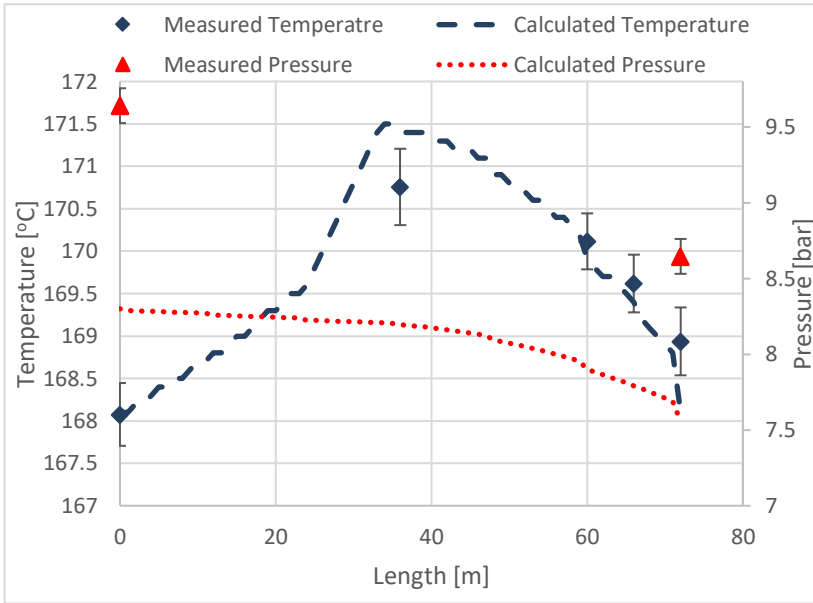
220

Figure F- 2 - Hypothetical situation modeling the data of 26/04 considering a different inlet pressure in order to match the temperature profile.

The temperature profile stayed much closed to the experimental one, and the HTF achieved a saturation temperature on around 35 m. However, both the inlet and outlet pressures are distant from the measured ones. An error on the inlet pressure measurement could be justified by some physical restriction on some joint or flexible hose after the sensor position, before entering the receiver. An error on the outlet pressure measurement, however, is not justifiable since the sensor is positioned after the last flexible hose of the receiver, just before re-entering the steam separator.

Another hypothetical condition, showed in Figure F-3, considers a different mass flow rate in order for the model to achieve the experimental pressure drop. In this case it is the temperature profile that is far from the experimental one.
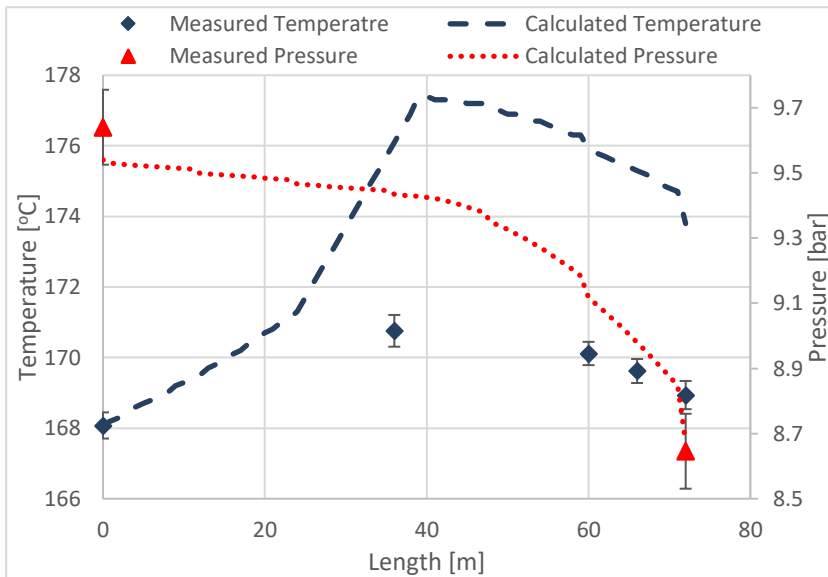
Figure F- 3 - Hypothetical situation modeling the data of 26/04 considering a different mass flow rate in order to match the experimental pressure drop.

In fact, the measured temperature of 169 °C at the outlet is below the saturation temperature, which is around 174 °C. This difference is far greater than the uncertainty of the thermocouple. This could indicate that the fluid is actually subcooled, however, the thermal model was validated for single-phase conditions, and it indicates a heat gain enough for a saturated condition at the outlet. In addition, the temperature profile presents the behavior of saturated conditions, with a temperature drop on the last measurements typical of saturated system undergoing a pressure drop condition.

This inverse behavior can be seen on Figure 6.20, where the measured outlet pressure has a lower saturation temperature, around 104 °C, than the one measured, of 119 °C. A pressure drop between the temperature measurement and the pressure measurement, however, could justify this. The last thermocouple is installed on the absorber tube, as the pressure sensor is installed just before the steam separator. There is a large flexible hose between these two measurements, and in some tests, it presented a belly, that could concentrate liquid on its bottom creating a resistance on the path of the flow. In this case, the model presented a temperature profile much closer to the measured one.